Physical modeling of junction processing in FDSOI devices for 20 nm node and below

Benoît Sklénard

UNIVERSITÉ DE GRENOBLE

THÈSE

Pour obtenir le grade de

DOCTEUR DE L'UNIVERSITÉ DE GRENOBLE

Spécialité : **Nano-Electronique et Nano-Technologies**

Arrêté ministériel : 7 août 2006

Présentée par

Benoît SKLENARD

Thèse dirigée par **Sorin CRISTOLOVEANU**

préparée au sein des **Laboratoires CEA Leti et IMEP-LAHC**
dans **l'École Doctorale EEATS**

Modélisation physique de la réalisation des jonctions FDSOI pour le nœud 20 nm et au-delà

Thèse soutenue publiquement le **10 Avril 2014**,
devant le jury composé de :

M. Alain CLAVERIE
Directeur de recherche, CNRS/CEMES (Président)
M. Nick COWERN
Professeur, Newcastle University, UK (Rapporteur)
Mme Evelyne LAMPIN
Chargée de recherche, CNRS/IEMN (Rapporteur)
Mlle Perrine BATUDE
Ingénieur, docteur, CEA Leti (Co-encadrante)
M. Sorin CRISTOLOVEANU
Directeur de recherche, IMEP-LAHC (Directeur de thèse)
M. Ignacio MARTIN-BRAGADO
Docteur, IMDEA Materials, Espagne (Co-encadrant)
M. Clément TAVERNIER
Ingénieur, STMicroelectronics (Co-encadrant, invité au Jury)
Mme Pierrette RIVALLIN
Ingénieur, CEA Leti (Co-encadrante, invitée au Jury)

Acknowledgments

First and foremost I want to thank my advisor Sorin Cristoloveanu and my technical supervisors Perrine Batude, Pierrette Rivallin, Ignacio Martín Bragado and Clément Tavernier. I would like to acknowledge their advices, support and great patience at all times.

I am also gratefull to the members of TCAD team at STMicroelectronics including Olivier Saxod, Pierre Boulenc (former member now at IMEC), Floria Blanchet, Sébastien Gallois-Garreignot (actually he is not really from TCAD team), Denis Rideau, Frédéric Monsieur... and to my former technical supervisors Ardechir Pakfar and François Wacquant (one week!).

I would also like to thank Assawer Soussou and Zahi Essa who have started and finished their PhD with me, and the other PhD students I have met during these 3 years: Amina Sidhoum, Andres Quiroga, Julien Dura, Hadrien Lepage, Cuiqin Xu, Papa Momar Souare, Komi Atchou Ewuame, Olivier Nier, Yvan Denis, Gabriel Mugny, Pierre Dorion, Sébastien Guarnay, Anouar Idrissi–Eloudrhiri, Luca Pasini, Laura Agudo, Mónica Prieto de Pedro, José Luis Gómez-Sellés, Ignacio Dopico...

In CEA Leti, I thank the members of the modeling and simulation laboratory: Philippe Blaise, François Triozon, Joris Lacord, Estelle Brague, Jean-Charles Barbe, Benoît Mathieu, Sébastien Martinie, Olga Cueto, Marie–Anne Jaud, François De Crecy, Hélène Jacquinot, Gilles Le Carval, Luca Lucci, Patrick Martin, Marina Reyboz, Pascal Scheiblin, Anne–Sophie Royet. I have also appreciated the help and collaboration with many people from other laboratories including Olivier Faynot, Maud Vinet, Thierry Poiroux, David Cooper, Adeline Grenier, Denis Blachier, Frédéric Mazen, Shay Reboh...

I am most grateful to Séb, Maria, Karine and Assawer for their encouragement during the writing of the PhD thesis and the preparation of the defense.

For this dissertation I would like to thank my reading committee members Evelyne Lampin and Nick Cowern for their time and interest. I would also like to thank Alain Claverie for accepting to be part of my oral defense committee.

Last, but by no means least, I thank my family, for all their love and encouragement. My parents, brothers and sister have given me their support and encouragement throughout the PhD.

Benoît Sklénard
September 2014

Contents

List of Figures

List of Tables

Introduction

THE manufacturing of integrated circuits (ICs) requires the reduction of microelectronic device dimensions in order to increase their performances and to incorporate more of them on a single chip. Over the past 40 years, the size of transistors has been drastically reduced following the so–called Moore's scaling law. This has contributed to the development of more and more powerful circuits. Nevertheless, there is a consensus on the fact that the dimensions of nowadays transistors are approaching the physical limits of miniaturization. Beyond this limit, alternatives have to be introduced to replace the conventional bulk planar architecture. Among them, the use of Silicon–On–Insulator (SOI) substrates or non–planar architectures such as FinFETs or nanowires are considered best options by semiconductor companies. For example, STMicroelectronics has chosen to develop a fully depleted Silicon–On–Insulator (FDSOI) technology for 28 nm and 14 nm nodes. In contrast, Intel has developed a nonplanar TriGate transistor architecture for its 22 nm node.

An alternative to device scaling is offered by a 3D sequential integration scheme in order to keep increasing the density of integrated circuits. This technique consists in fabricating the different transistor levels one after the other on the same substrate [Batude *et al.* 2011a, Batude *et al.* 2013]. In particular, 3D sequential integration is an active field of investigation at CEA Leti. However, its implementation faces the challenge of being able to process a high performance transistor at the top with a low thermal budget (typically $\leqslant$ 600 °C) in order to preserve the transistor at the bottom from any degradation, as the stacked layers are fabricated sequentially. This implies a drastic change for the dopant activation that is commonly performed with a high thermal budget (1050 °C spike anneal). For the moment, the technological option chosen at CEA Leti is to form the junction of top transistors by Solid Phase Epitaxial Regrowth (SPER) allowing to reduce the activation anneal at temperatures between 500 and 600 °C that are compatible with 3D sequential integration.

More generally, junction formation is particularly critical for advanced technology nodes. Indeed, on the one hand, high electrical activation is required to reduce the access resistances. On the other hand, low diffusion is desirable to limit short–channel effects and avoid problems related with device scaling. Among the possible technological options, SPER can be used to meet these requirements since it allows the formation of highly activated and abrupt junctions. This technique involves an amorphisation of the crystalline substrate either with the dopant itself or using a pre–amorphizing implantation (PAI) with heavier species. Then, the amorphized region recrystallizes through the so–called SPER process and dopant impurities present in the amorphous material are incorporated into lattice sites during the solid–solid amorphous to crystaline phase transformation. In particular, the out–of–equilibrium nature of SPER enables to achieve metastable above–equilibrium activation levels approximately one to two orders of magnitude higher than the solid solubility for a given dopant species.

This work is dedicated to the modeling and simulation of SPER using kinetic Monte Carlo (KMC) method in order to get insight into the physical mechanisms playing a role in the junction formation at low processing temperatures.

CHAPTER 1

Context and goal of this work

Contents

1.1 Technological context

In 1971, Intel introduced and marketed the first 4–bit microprocessor (called Intel 4004) which contained 2300 p–type MOSFET transistors with minimum dimension of 10 μm. Since then, device dimensions have been reduced following Moore's law in order to achieve higher density and performance and lower power consumption. Nowadays, Intel is manufacturing microprocessors based on their 22 nm technology and containing billions of transistors on a single chip.

However, extreme scaling has given rise to the increase of parasitic phenomena such as short channel effects (SCE), gate and junction leakages or static and dynamic power consumption. As a consequence, solutions have to be developed in order to overcome these problems. In particular, for actual technology nodes, new architectures have been introduced such as planar fully depleted Silicon on Insulator (FDSOI) devices or multiple gates FETs (either on bulk or SOI) [Kuhn 2011]. Fig. 1.1 illustrates the evolution of device architectures as a function of channel length reduction in order to preserve a good electrostatic control of the transistor. Planar FDSOI, TriGate and FinFET architectures are considered up to 10 nm node depending on the semiconductor company strategy. Beyond, multiple gates or gate all–around FET might be mandatory to ensure high performance and gate control of the channel.

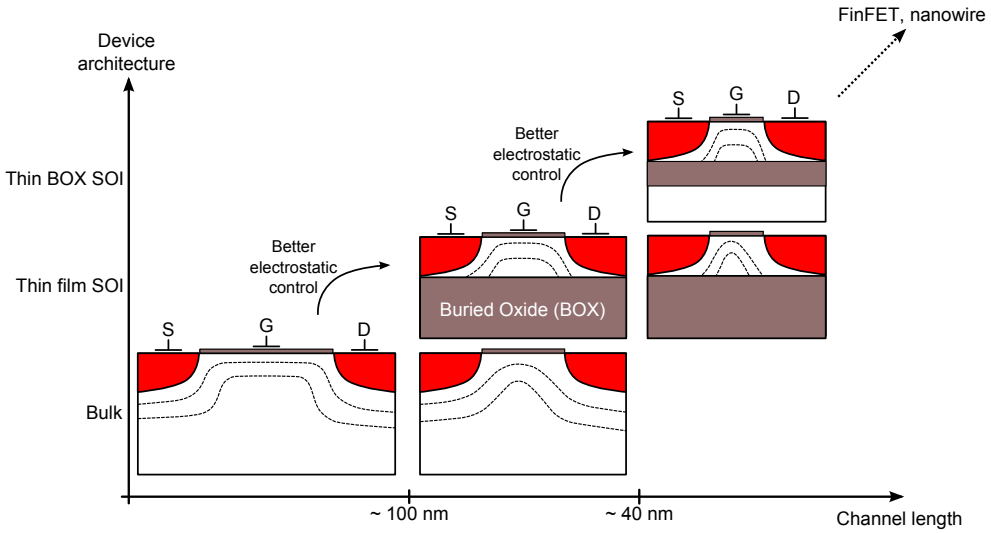

Figure 1.1: Evolution of device architectures as a function of channel length reduction in order to preserve a good electrostatic control of the transistor. Dashed lines represent electric field lines inside the device.

1.1.1 3D sequential integration

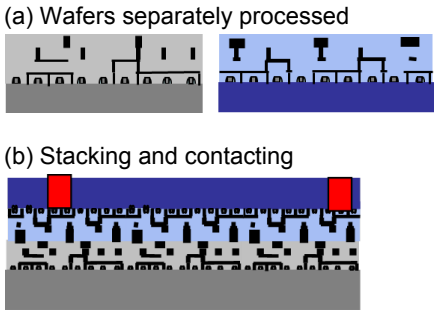

Figure 1.2: Description of parallel integration process flow. (a) Wafers are processed separately and (b) stacked and contacted afterward.

An alternative to scaling can be brought by a 3D integration scheme which consists in stacking the transistor levels rather than reducing the devices dimensions [Batude *et al.* 2013, Batude *et al.* 2011a]. Generally, 3D integration refers to 3D parallel integration where different chips are processed independently and stacked vertically afterward as shown schematically in Fig. 1.2. The connection between the stacked layers is usually performed using Through–Silicon Vias (TSV). However this method is limited to connecting blocks of a few thousand of transistors. To overcome this limitation, an alternative technique called 3D sequential integration has been emerging recently. In this integration scheme, transistor layers are processed sequentially and the stacked layers can be connected at the transistor scale as shown schematically in Fig. 1.3.

However its implementation faces the challenge of being able to process a high performance top transistor with a reduced thermal budget in order to preserve the bottom transistor from any degradation. Indeed, a too high thermal budget for the process of top layers would dramatically affect the performances of bottom layers (see [Batude *et al.* 2013, Batude *et al.* 2011a] and references cited therein for further technological details) by:

- affecting the salicide stability ,

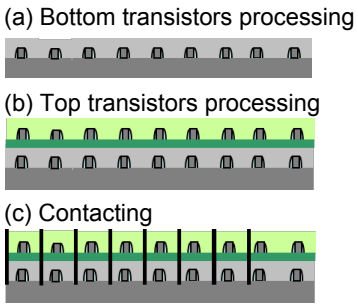

Figure 1.3: Description of 3D sequential integration process flow where transistor layers are processed sequentially. (a) The first transistor layer is processed, (b) a second layer is then processed on top of it and (c) the layers are then contacted.

- causing interfacial gate oxide growth,
- causing adverse dopant diffusion and deactivation on bottom devices.

A low thermal (LT) budget process is therefore mandatory for the fabrication of top layers. The considered option at CEA Leti is to activate the dopants through solid phase epitaxial regrowth (SPER) by annealing at a temperature below 600 °C instead of conventional spike anneals involving temperatures higher than 1000 °C that are not compatible with a 3D sequential integration scheme. More emphasis about this LT process will be given in section 1.1.2. The

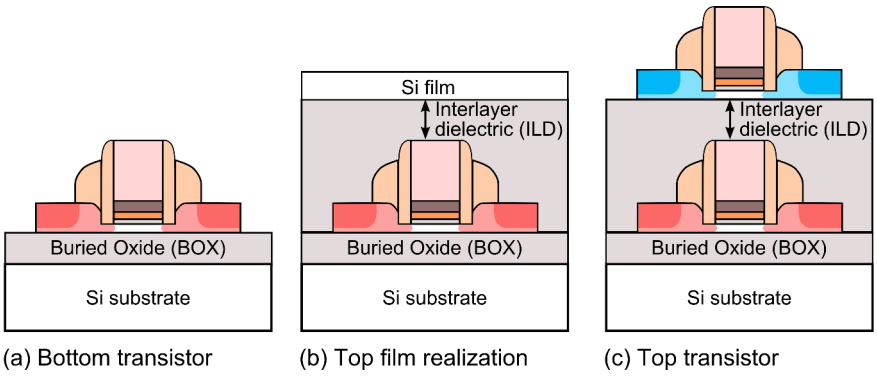

Figure 1.4: Description of the 3D sequential integration scheme process.

simplified process flow to integrate sequentially two transistor levels is illustrated schematically in Fig. 1.4. The bottom transistor is processed with a conventional high temperature thermal budget (Fig. 1.4a). Then, the top film layer is obtained via a low temperature molecular bonding (at 200 °C) of an SOI substrate enabling the full transfer of a monocrystalline Si layer (Fig. 1.4b). Finally, the top transitor is fabricated with a LT budget process (Fig. 1.4c). Fig. 1.5 shows a Transmission Electron Microscopy (TEM) cross-section image of two stacked transistors at the end of a 3D sequential integration process [Batude *et al.* 2011b] for further details.

1.1.2 Low thermal budget process

In a low thermal budget process, the temperature involved during the transistor fabrication cannot exceed 600 °C. We should point out that this temperature limit has been determined in order to preserve the bottom transistor from any degradation within a 3D sequential integration scheme. In a standard process, the highest thermal budget is needed for dopant activation. As

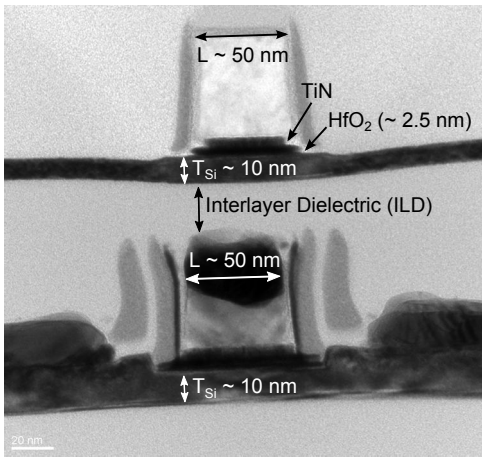

Figure 1.5: Transmission electron microscopy (TEM) cross-section image of stacked transistors processed through a sequential integration scheme at CEA Leti from [Batude *et al.* 2011b].

a consequence, in the case of a low thermal budget process, junction formation is the most challenging part. Indeed, dopant activation at 600 °C or below leads to quite low activation levels that are not compatible with sheet resistance requirements for advanced devices. To overcome this problem, dopant atoms are incorporated into lattice positions through the solid phase epitaxial regrowth (SPER) of an amorphous region. Such a technique allows to achieve very high activation levels exceeding the impurity solid solubility in the host material. The main steps of LT process are illustrated in Fig. 1.6. Dopant atoms are incorporated into the

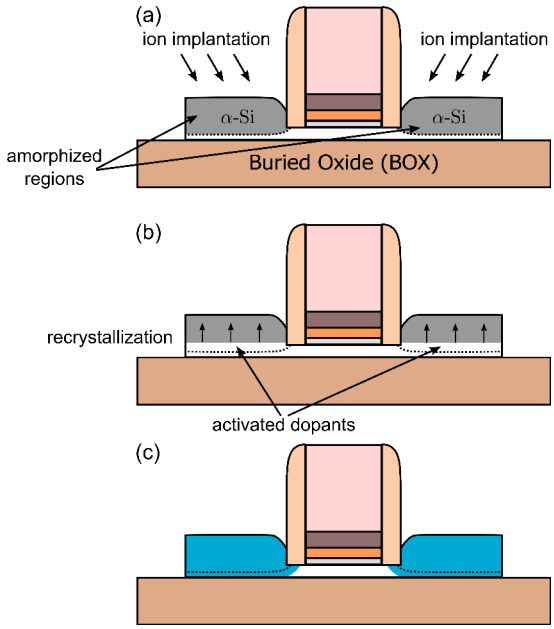

Figure 1.6: Description of the low thermal budget process. (a) Ion implantation technique is used to create amorphous regions and to incorporate dopant atoms. (b) Subsequent anneal leads to the recrystallization of the amorphous regions through solid phase epitaxial regrowth (SPER) and dopant atoms are incorporated into lattice positions. (c) After SPER is completed, the dopants present in the as–implanted amorphous region and a small fraction of those located below the amorphous/crystalline interface are electrical active.

substrate using ion implantation as shown in Fig. 1.6a. However, a particularity of this process is that implant parameters (species, dose, energy, dose rate and temperature) are set up in order to create amorphous regions in the zones that have to be doped (typically source and

drain in a MOSFET architecture). For light species such as boron, amorphization cannot be achieved and a pre–amorphization implant (PAI) step with a group IV impurity (Si or Ge) may be required. Amorphous regions recrystallize epitaxially through SPER upon subsequent anneal at temperatures ranging from 500 °C to 600 °C. During SPER, dopant species are incorporated into lattice positions and become electrically active as shown in Fig. 1.6b. After SPER has been completed, the dopants initially present in the amorphous region and a small fraction of those located below the amorphous/crystalline interface are electrically active as shown in Fig. 1.6c. In section 1.1.2.1 we will further discuss the amorphization process in the frame of a LT process on SOI substrates. Then, in section 1.1.2.2 we will briefly present the recrystallization processes which enable an amorphous region to recover its crystalline nature.

1.1.2.1 Amorphization

Dopant impurities are often introduced into the silicon substrate using ion implantation. This technique consists in accelerating the ions in an electrical field in order to give them enough kinetic energy to make them penetrate the target solid. This causes the implanted crystal to be damaged by the energetic collision cascades resulting from the impact of the implanted ion with lattice atoms. The concentration of these induced defects depends of the implanted species, its dose and its energy [Hobler & Otto 2003]. The implant damages tend to recombine and their lifetime therefore depends on the dose rate and the implant temperature [Posselt *et al.* 2001]. The recombination of these defects during the implant is often referred to as dynamic annealing and is the basis of amorphization. Fig. 1.7 shows a schematic representation of ion implantation. An incident ion impacts the crystalline lattice (Fig. 1.7a) causing a displacement of a silicon out of its lattice position (Fig. 1.7b). Hence, there is a lattice site with a missing atom called a vacancy (dotted circle) and an extra atom called an interstitial (colored circle). The interstitial moves into the silicon lattice because of the kinetic energy that has been transferred during the collision. It can also knock other crystal atoms and create further implant defects through collision cascades. A collision cascade is quite

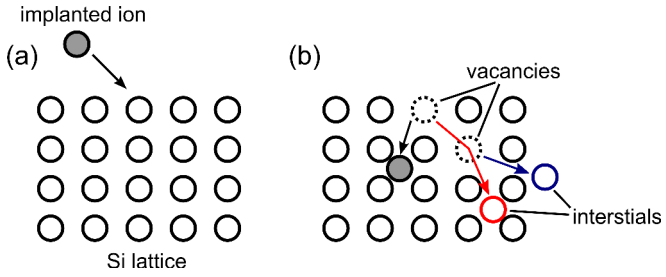

Figure 1.7: Schematic representation of ion implantation. (a) An incident ion is accelerated and impacts the silicon lattice. (b) Because of the energy transfer during the collision, the implanted ion can cause target atoms to be knocked out of their lattice position. The missing atom is called a vacancy (dotted circles) and the additional atom that is not in substitional position anymore is called an interstial (colored circles). Vacancies and interstials constitute the implant defects. If the energy transferred to the interstitial during the first collision is high enough, it can displace other atoms causing collision cascades.

fast and typically develops in about 1 ps. After that, thermally activated processes drive the evolution of the implant defects. Interstitials (I) and vacancies (V) migrate and can interact with each other and annihilate. However the recombination of an interstitial with a vacancy is not instantaneous and requires to overcome an energy barrier ($\sim$ 1.23 eV [Tang *et al.* 1997]). Theoretical calculations have evidenced the formation of the so–called *IV pair* when an interstitial and a vacancy interact with each other [Tang *et al.* 1997, Marqués *et al.* 2003]. It

consists in a local rearrangement of bonds with no excess or deficit of atoms and is often referred as a *bond defect*. This defect has gained a lot of interest because it introduces five– and seven–membered rings in the silicon lattice which are characteristic of the amorphous phase. As a consequence this defect is suspected to play a crucial role in the amorphization process [Marqués *et al.* 2003], as illustrated in Fig. 1.8. At the beginning of the implant, interstitial

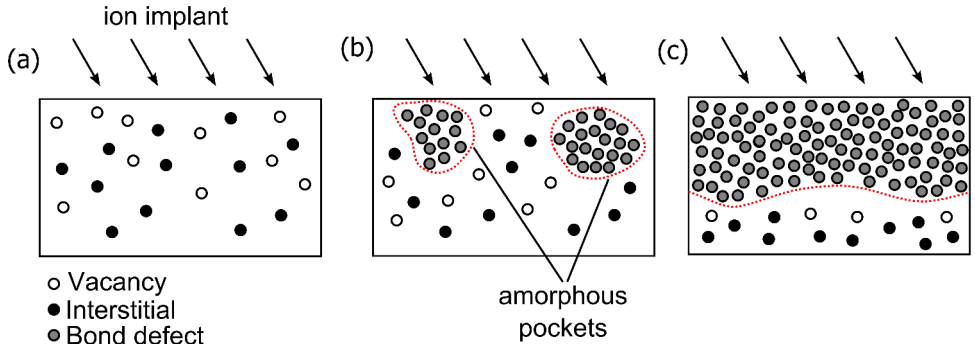

Figure 1.8: Schematic description of the different stages of ion implantation leading to the amorphization of the substrate. (a) Collisions between incident ions and lattice atoms lead to the generation of vacancies and interstitials (see Fig. 1.7). (b) Interstitials and vacancies may annihilate but this process is not instantaneous and amorphous pockets can be formed. (c) Upon sufficiently high irradiation conditions, a planar amorphous/crystalline interface can be achieved.

and vacancy defects are induced by the atomic collisions (Fig. 1.8a). These defects interact with each other and either annihilate or form a bond defect. The bond defect becomes more stable when the number of surrounding bond defects increases giving rise to the formation of amorphous pockets (Fig. 1.8b). After further irradiation, a planar amorphous/crystalline interface can be achieved as shown in Fig. 1.8c. We should point out that in the case of the LT process, amorphous regions are created with a continuous amorphous/crystalline interface corresponding to the situation shown in Fig. 1.8c. The stability of the bond defect with sur-

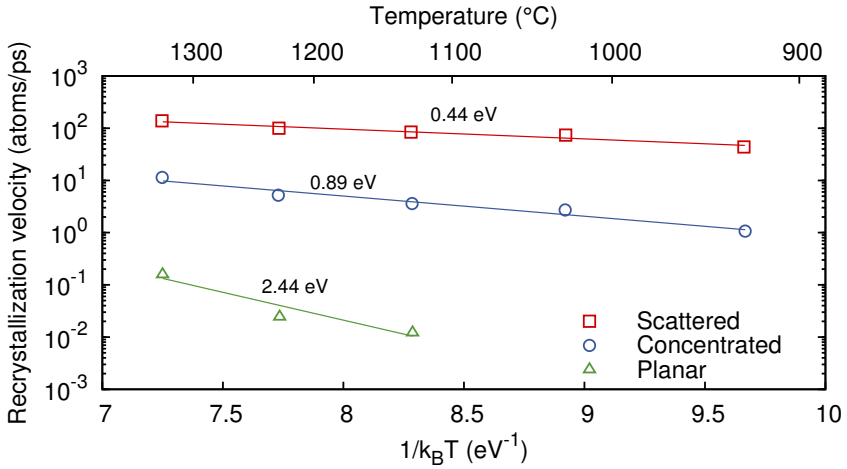

Figure 1.9: Arrhenius plot from [Marqués *et al.* 2003] of the recrystallization velocity in situations with scattered and concentrated damage and for a planar amorphous/crystalline interface.

rounding bond defects is illustrated in Fig. 1.9 where recrystallization velocities are reported for situations with scattered and concentrated damage and for a planar amorphous/crystalline interface. These data have been obtained by Marques *et al.* with molecular dynamics simulations (see [Marqués *et al.* 2003] for further details).

1.1.2.2 Recrystallization

After the formation of amorphous regions, a thermal anneal is carried out so that solid phase epitaxial regrowth (SPER) takes place. During this process, two distinct phenomena occur:

1. the amorphous region is regrown epitaxially layer–by–layer from the amorphous/crystalline interface,
2. during the solid–solid transition from amorphous to crystalline, dopant impurities are incorporated into lattice positions where they are electrically active.

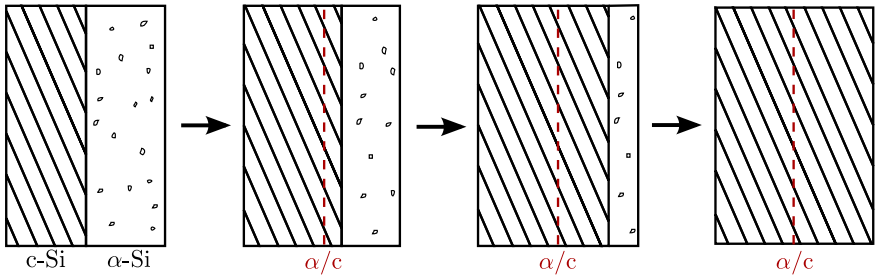

(a) Solid Phase Epitaxial Regrowth (SPER)

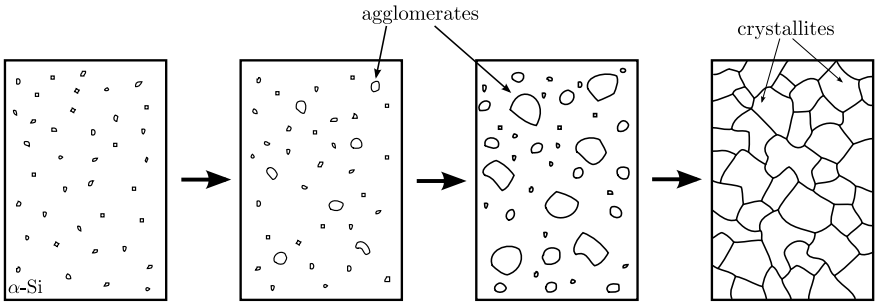

(b) Random nucleation and growth (RNG)

Figure 1.10: Schematics of (a) Solid Phase Epitaxial Regrowth (SPER) and (b) random nucleation and growth (RNG) processes.

The recrystallization process though SPER is shown schematically in Fig. 1.10a. It should also be emphasized that recrystallization may also occur inside the amorphous phase through random nucleation and growth (RNG) as illustrated in Fig. 1.10b. RNG consists in the nucleation of small agglomerates that further expand into crystallites but fortunately does not happen at the temperatures involved in the LT process ($\leqslant$ 600 °C) because of its high activation energy ($\sim$ 5 eV).

Dopant activation through SPER occurs out–of–equilibrium and gives rise to very high activation levels that are far exceeding the impurity solid solubility in silicon. Unfortunately, such super–saturated dopant concentrations exist in a metastable state and dopant deactivation may occur upon further thermal processing [Duffy *et al.* 2006].

SPER appears to be a very complex process which kinetics can be influenced by various parameters such as substrate orientation, non–hydrostatic stress or hydrostatic pressure and the presence of impurities, as we will show in this manuscript.

1.1.3 Challenges for junction formation

Junction formation with a low processing temperature faces several challenges with respect to conventional anneals. In the case of an FDSOI architecture, the first critical step is the control

of the amorphous region discussed in section 1.1.3.1. Then, during subsequent anneals several phenomena take place that can affect the quality of the junction. In section 1.1.3.2 we will present the problems related with the control of the recrystallization of the amorphous region. In section 1.1.3.3, we discuss the implication of the presence of End Of Range (EOR) defects in a LT process in terms of leakage currents and dopant deactivation. In section 1.1.3.4 we focus on dopant activation that is slightly related with the existence of EOR defects during the process. Finally, in section 1.1.3.5 we discuss the role and interest of simulation in the development of LT process.

1.1.3.1 Amorphization engineering

The amorphized region has to be deep enough in order to maximize the dopant activation and therefore minimize the sheet resistance. Nevertheless, a crystalline seed has to remain between the amorphous region and the buried oxide (BOX) so that the regrowth can proceed vertically as shown in Fig. 1.11a. The extreme situation would be the full amorphization of the film illustrated in Fig. 1.11b. In that case, the only way for SPER to proceed is through the lateral front which would give rise to (i) a slow and eventually incomplete regrowth and (ii) a defective recrystallization. On the other hand, a limitation of the junction formation at

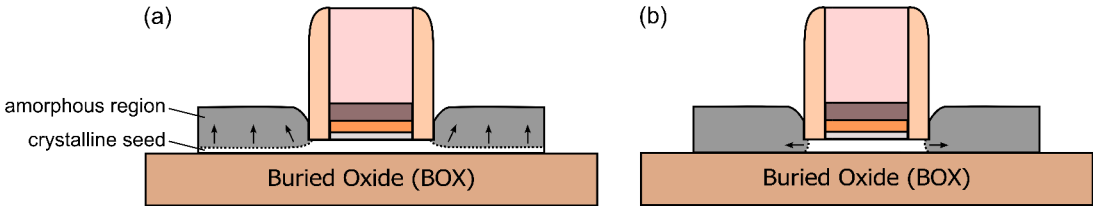

Figure 1.11: Schematic representation of two achievable amorphization conditions. (a) Amorphization with a crystalline seed between the bottom of the amorphous region and the buried oxide so that the regrowth can proceeds vertically and (b) full amorphization.

low processing temperature arises from the low dopant activation in the region located beyond the original amorphous/crystalline interface, giving rise to underlapped junctions. In contrast, conventional junctions tend to be slightly overlapped. This is illustrated in Fig. 1.12. The ideal junction is also reported in dotted line. An underlapped junction can lead to high access resistances that may be incompatible with technological requirements. As a consequence, a lateral control of the amorphization appears to be critical and still remains an open problem.

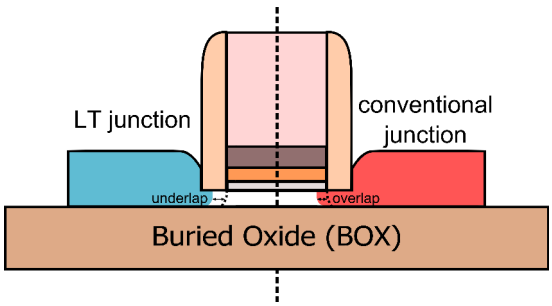

Figure 1.12: Schematic representation of the final junction with a low processing temperature (left side) and a conventional process (right side).

1.1.3.2 Recrystallization control

After the formation of amorphous regions, the recrystallization proceeds through SPER. As it has been shown previously, a complete amorphization leads to a complicated situation that should be avoided. However, even in the case where a crystalline seed exists, so that SPER advances vertically, complex phenomena related with regrowth anisotropy take place near to the edges. This can become particularly critical for nanoscale FinFETs or nanowires as observed experimentally in [Duffy *et al.* 2007]. In the case of planar FDSOI devices, challenges arise because of the presence of SiGe or SiC alloys with ultrahigh dopant concentrations used for source and drain regions that can have a strong influence on SPER kinetics and cause recrystallization problems.

1.1.3.3 Influence of End Of Range defects

After ion–implantation a high interstitial concentration is left below the amorphous/crystalline interface. During subsequent thermal processing they tend to interact to form bigger and more stable defects, the so–called end of range (EOR) defects. They first form small interstitial clusters and further evolve towards {311} defects and dislocation loops. The presence of these defects generally has detrimental consequences for the device. During the process, EOR defects release interstitials that can interact with dopants in substitutional positions and cause deactivation (see section 1.1.3.4). On the other hand, residual EOR defects at the end of the process can create energy levels in the bandgap and induce leakage currents when they are located in or close to depletion regions [Duffy *et al.* 2010].

The presence of residual EOR defects has been pointed out to cause severe leakage current. During this work, results showing similar leakage currents between a device fabricated with a LT process and a device fabricated using conventional high temperature anneals have been achieved. For sake of consistency, this manuscript only treats the atomistic modeling of SPER that has been the main occupation of this PhD and does not discuss the evolution of EOR defects during LT process. The interested reader can refer to [Sklenard *et al.* 2013b].

1.1.3.4 Dopant activation

SPER is an attractive technique to activate dopants since it enables to form highly activated junctions with a dopant concentration reaching a metastable solubility that is significantly higher than the maximum equilibrium solubility. This is due to the fact that during the recrystallization process the silicon lattice can substitutionally incorporate a very high quantity of impurity atoms. However, during the post–recrystallization regime, further thermal processing may lead to dopant deactivation that can be detrimental to device performances. As a consequence, the control of junction stability appears as a critical issue in the case of low temperature processing. Nevertheless, during this PhD it has been evidenced that FDSOI technology provides a solution to suppress boron deactivation by limiting the interaction between EOR defects and electrically active dopants [Xu *et al.* 2012].

1.1.3.5 The need of numerical simulation

The technological challenges mentioned in the previous sections highlight the complexity to optimize the fabrication of a junction with a low processing temperature. Indeed, the too many influencing factors make junction engineering experimentally impracticable. To overcome this limitation, numerical simulations are an essential tool for the development of a new technology.

On the one hand, simulation allows to get insight into the physical phenomena occurring during the junction formation giving rise to new technological solutions to optimize them. On the other hand, a predictive simulation may allow to evaluate the feasibility and the impact of a technological solution by significantly reducing the development cost and time. Finally, simulation can be use to understand the origin of a problem rather than resorting to experimental characterization that may appear to be long, expensive and impossible on complex architectures.

The purpose of this PhD is to develop new models to improve the physical understanding of junction formation with a low processing temperature. Next section gives an overview of atomistic approaches and details the kinetic Monte Carlo method that has been used in the frame of this PhD.

1.2 Atomistic simulation

Technology Computer Aided Design (TCAD) process simulation tools are widely used in semiconductor industry as a support to technology development. They aim to simulate the process steps of the fabrication of electronic devices and predict the final impurities, stress distribution and device geometry. The results are generally used as an input for device simulators to depict electrical characteristics. The coupling between process and device simulators provides a complete simulation flow of a given process. This enables to analyze the influence of process parameters on electrical characteristics and therefore predict the impact of a process optimization on the device performances without having to test it experimentally. However, to be predictive, process simulation tools need to account for the many physical phenomena occurring at the different steps of the process. They generally rely on continuum models, *i.e.* a set of phenomenological differential equations that are solved using finite element methods (FEM) or finite volume methods (FVM). Such models therefore ignore the atomistic nature of solids. However, as the size of the devices is scaled down, atomistic methods become very appealing to provide a description of the materials at the atomistic scale and get insight into the physical mechanisms as illustrated in Fig. 1.13.

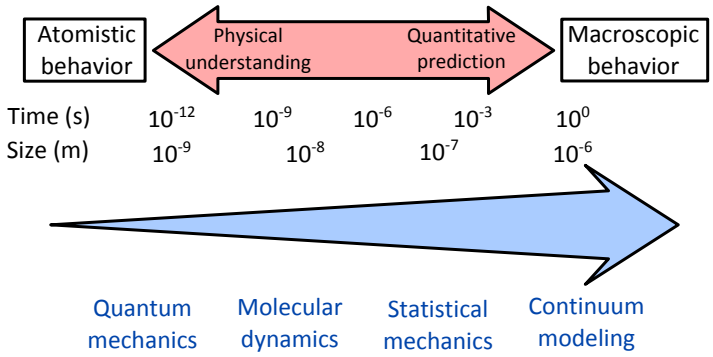

Figure 1.13: Multiscale modeling.

Atomistic approaches actually refer to a broad class of methods that we should clarify before going further. The most fundamental of these methods aim to compute the electronic structure of a system by solving more or less approximate quantum-mechanical equations. Numerical methods used to achieve these calculations can be splitted into two categories:

- *ab-initio* methods
- semi-empirical methods.

Electronic structure calculations can then be used to compute various material properties or formation energies. However, these methods cannot predict the dynamical properties of a system[1]. This leads us to the second class of atomistic methods that can be used to model atomic or electronic transport phenomena. It is important to emphasize that electronic structure calculations presented above may be used in conjunction with these methods to describe the interactions between the particles occurring during the transport. Since electronic transport is out of the scope of this manuscript, we will focus hereinafter on atomic transport. The atomistic methods used to simulate atomic transport aim to describe the evolution of interacting atoms of a system, generally upon the Born–Oppenheimer approximation[2]. The most direct, and therefore the most fundamental, of these techniques is the molecular dynamics (MD) method which consists of simulating the evolution of interacting atoms by integrating their classical equations of motion. The forces between the atoms have to be correctly described by using potential energy surfaces (PES) that can be computed from the electronic structure (using the atomistic methods described above) or from an empirical interatomic potential. However, a huge limitation of this technique resides in the accessible simulation timescales that do not exceed 10^{-6} s. In contrast, lattice or off-lattice kinetic Monte Carlo (KMC) approaches permit to overcome this limitation by evolving a system from state to state to account for long-timescale dynamics. Intermediate approaches can also be used to extend the timescales of MD simulations [Voter *et al.* 2002]. We will briefly describe MD and KMC methods hereafter.

1.2.1 Molecular Dynamics methods

Molecular Dynamics methods have been developed in the 1950s [Alder & Wainwright 1957] and have become very popular to treat problems related to condensed matter physics or other science disciplines. The basic principle relies on the assumption that the motion of particles can be treated classically upon the Born–Oppenheimer approximation. For a system of n particles, the equation of motion for each atom i is solved using Newton's law:

$$m_i \frac{\partial^2 \boldsymbol{r_i}}{\partial t^2} = \boldsymbol{F_i}(\boldsymbol{r_1}, \boldsymbol{r_2}, ..., \boldsymbol{r_n}) \tag{1.1}$$

where m_i is the mass of the atom i, $\boldsymbol{r_i}$ its position and $\boldsymbol{F_i}$ the forces acting on it.

Fig. 1.14 shows a simplified Molecular Dynamics algorithm highlighting the main steps. At the beginning of the simulation, the system has to be initialized. It means that initial positions and velocities have to be assigned to all the particles present in the simulation domain. Then, the forces $\boldsymbol{F_i}$ acting on each particle are computed. In classical molecular dynamics simulations an empirical potential is used in order to treat domains that are large enough to correctly capture the physical phenomenon of interest. However, the main concern of these potentials is their reliability in accurately predicting quantities for which they were not fit. In particular, the choice of the interatomic potential depends on the studied physical phenomenon. Commonly used interatomic potentials for silicon include the Tersoff's potential [Tersoff 1988], the Stillinger–Weber potential [Stillinger & Weber 1985] and its recent parametrization called SW115 [Albenze & Clancy 2005] or the environment dependent interatomic potential (EDIP) [Bazant *et al.* 1997, Justo *et al.* 1998]. Finally, once the forces have been computed, the new atomic positions are calculated by solving Newton's equation of motion by integrating Eq.1.1. This step is commonly achieved by a Verlet integration [Verlet 1967, Verlet 1968]. Molecular

[1] We should emphasize that an extension of Density Functional Theory referred as Time Dependent Density Functional Theory (TDDFT) exists to investigate time dependent physical phenomena [Burke *et al.* 2005].

[2] Adiabatic or Born–Oppenheimer approximation states that the motion of slow and fast degrees of freedom are separable. In our case, it means that electron cloud adjusts instantly to changes in the nuclear configuration.

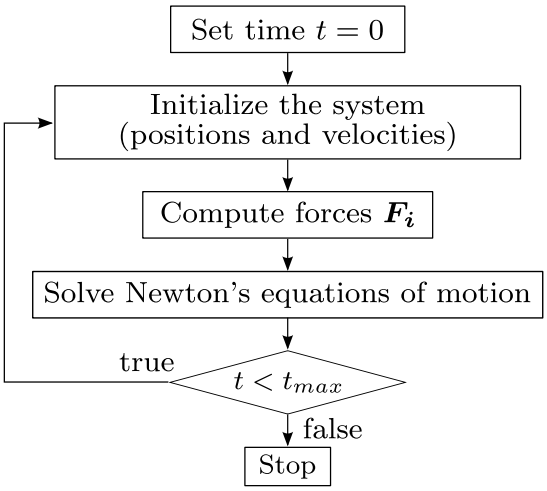

Figure 1.14: Molecular dynamics algorithm.

dynamics methods are a vast subject that would require a complete book and are therefore out of the scope of this section. The interested reader is invited to consult the dedicated literature such as [Frenkel & Smit 2001].

1.2.2 Kinetic Monte Carlo methods

The concept of Monte Carlo (MC) simulation concerns the methods relying on the use of random numbers in their algorithms. The name actually refers to the famous eponymous casino in the city of Monaco. They were introduced in the late 1940's at Los Alamos National Laboratory [Metropolis & Ulam 1949] and have known a wide development since then. Various algorithms have thus emerged, their only similarity being the use of random numbers [Landau & Kurt 2009]. Among them, the most famous include Metropolis Monte Carlo [Metropolis *et al.* 1953] and Kinetic Monte Carlo (KMC)[3] [Young & Elcock 1966] algorithms. Metropolis Monte Carlo was developed in the 1950s to study the static properties of a system. In contrast, KMC method was introduced in the 1960s to study dynamical properties of a system and will be described hereinafter.

Before going further into the details of the KMC technique, it is important to emphasize the assumptions it is based on. With Molecular Dynamics most of the time is spent to describe atomic vibrations while microscopic phenomena of interest (*i.e.* atomic jumps) occur over a longer timescale. Therefore, it can be assumed that the evolution of a system is characterized by occasional transitions from one state to another, where each state corresponds to an energy basin and two adjacent states are separated by an energy barrier (E_a) as depicted on Fig. 1.15. The potential energy barrier has to be large in comparison with k_BT for the event to be considered as rare. In addition, after a transition has occurred, it can be considered that the particle loses the memory of how it entered into the energy basin and the escape probability becomes independent of previous events. The processes are therefore Markovian [Gardiner 2009]. Then, if the transition rates are known *a priori*, it will be possible to describe the evolution of a system over much longer timescales than MD does. This is indeed the underlying concept of KMC method.

It can be shown that transitions are described using a Poisson process which is commonly

[3]The terminology kinetic Monte Carlo is now of common use, however, it has also been reported in initial papers as dynamic Monte Carlo methods [Fichthorn & Weinberg 1991].

Figure 1.15: Transition of a barrier energy leading to (a) a higher and (b) a lower energy state.

used in the theory of stochastic processes [Gardiner 2009, Fichthorn & Weinberg 1991]. Consider an event with rate r, then the transition probability density $f(t)$ giving the probability rate that the transition occurs at time t is:

$$f(t) = r \times \exp(-rt). \tag{1.2}$$

Generalizing to N independent Poisson processes, with rate r_i, results in a Poisson process with rate $R = \sum_{i=1}^{N} r_i$ and the transition probability density for this process is:

$$F(t) = R \times \exp(-Rt). \tag{1.3}$$

We can determine the mean time period between successive events: $\langle t \rangle = 1/R$.

The evolution of a system can be described by picking up random events with a probability proportional to their rate as shown in Fig. 1.16. The events are put end to end with a size proportional to their rate, a random number s is generated on the interval $(0, 1)$ and the event with the rate $R_{n-1} < sR \leqslant R_n$ is chosen. To evolve the clock of the system, the time has to be incremented by $1/R$ (the mean time period between successive events). More generally, the clock of the system can be incremented by a random time Δt, drawn from Eq. 1.3:

$$\Delta t = -\log(s')/R \tag{1.4}$$

where s' is a random number on the interval $(0, 1)$. The use of random numbers to evolve the clock of the system gives a better description of the stochastic nature of the involved processes and is justified because $\langle \log(s') \rangle = -1$. This procedure corresponds to the most common KMC algorithm referred as the residence-time algorithm [Bortz *et al.* 1975][4] that is presented schematically in Fig.1.17. It is worth noting that this algorithm will be used throughout this manuscript (see section 1.2.2.2 for additional information).

1.2.2.1 Transition State Theory (TST)

Transition state theory (TST) approximation is the formalism used in the Kinetic Monte Carlo method or in other accelerated dynamics methods to define the transition rates [Voter *et al.* 2002]. It was developed in 1935 by Eyring, Evans and Polanyi in order to define a theoretical framework to describe reaction rates [Laidler & King 1983]. Within TST, the transition rate k^{TST} is given by the canonical expectation of the flux through the dividing surface between an initial state A and a final state B, as shown in Fig. 1.18. It can be expressed as [Glasstone *et al.* 1941]:

$$k^{TST} = \frac{k_B T}{h} \frac{Z_{\ddagger}}{Z_{min}} \tag{1.5}$$

[4]This algorithm is also known as the n–fold way or BKL algorithm due to the paper of Bortz, Kalos and Liebowitz (see [Bortz *et al.* 1975]).

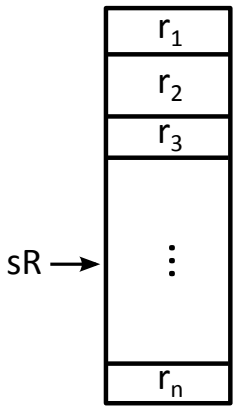

Figure 1.16: Schematic of the procedure for picking reaction pathway.

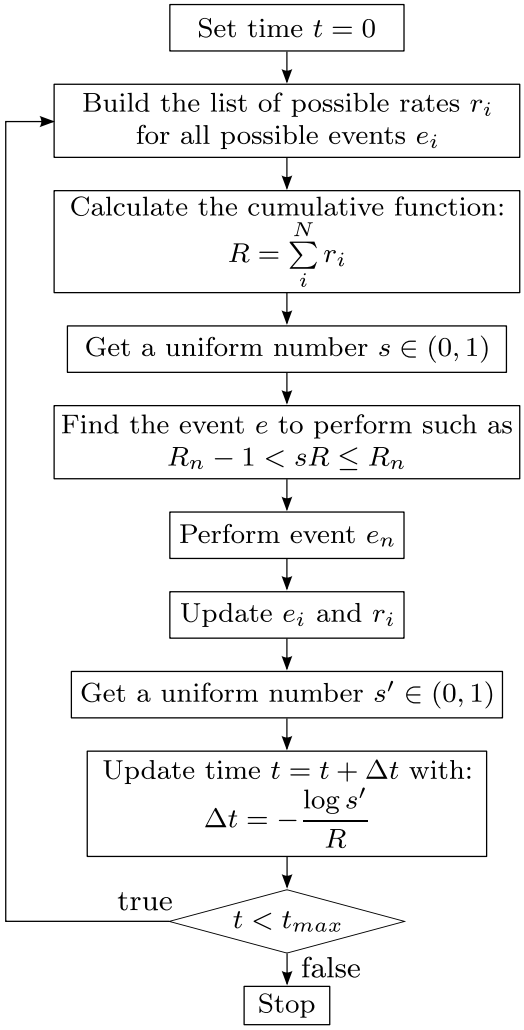

Figure 1.17: BKL Kinetic Monte Carlo algorithm [Bortz *et al.* 1975].

where Z_{min} and $Z_{\ddagger}$ are the partition function of the initial state and of the dividing surface respectively, h is Planck constant, k_B is the Boltzmann constant and T is the temperature. Unfortunately, an accurate evaluation of the partition functions happens to be impossible in practice. An approximation of the partition function consists in expanding the Hamiltonian of

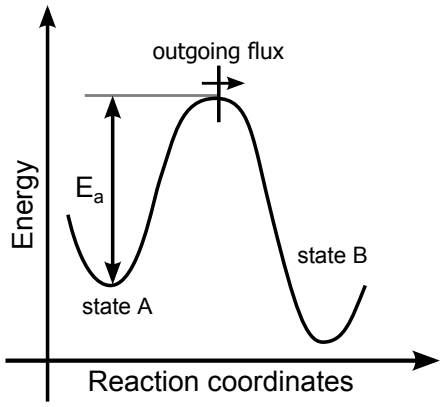

Figure 1.18: Schematic of the transition kinetic of a two state system. Within TST, the transition rate is given by the canonical expectation of the flux through the dividing surface between an initial state A and a final state B.

the system to second order around a local mechanical equilibrium state yielding:

$$Z_{min} = \frac{\exp\left(-\beta V_{min}\right)}{\prod_{i=1}^{D} \beta\hbar\omega_{min,i}} \tag{1.6}$$

and

$$Z_{\ddagger} = \frac{\exp\left(-\beta V_{\ddagger}\right)}{\prod_{i=1}^{D-1} \beta\hbar\omega_{\ddagger,i}} \tag{1.7}$$

where $\beta \equiv (k_B T)^{-1}$, V_{min} and $V_{\ddagger}$ are the potential energies at minimum and saddle points respectively, $\hbar$ is the reduced Planck constant, the ω are the real, positive, vibrational angular frequencies of the phonon modes of the system and D is the total number of vibrational degrees of freedom excluding free translations and rotations. Injecting Eq. 1.6 and 1.7 into Eq. 1.5, we obtain Vineyard expression defining the transition rate in the frame of harmonic approximation of TST [Vineyard 1957]:

$$k^{HTST} = \nu_0 \times \exp\left(-\frac{\Delta V}{k_B T}\right) \tag{1.8}$$

where

$$\nu_0 = \frac{1}{2\pi} \frac{\prod_{i=1}^{D} \omega_{min,i}}{\prod_{i=1}^{D-1} \omega_{\ddagger,i}} \tag{1.9}$$

is the so–called prefactor and

$$\Delta V = V_{\ddagger} - V_{min} \tag{1.10}$$

is the energy barrier for a given transition, also called activation energy and noted E_a in Fig. 1.18. Eq. 1.9 defines the transition probability used as an input in a KMC simulation.

1.2.2.2 Presentation of MMonCa

MMonCa is a recent multi–material oriented KMC simulator that has been used in the frame of this PhD to implement new models. It has been created by Dr. Ignacio Martín–Bragado at IMDEA Materials institute (Madrid, Spain). It is written in C++ and is integrated with the TCL library for user interactions. It contains two independent modules that can achieve different levels of modeling:

- the lattice kinetic Monte Carlo (LKMC) module relies on the lattice of the considered material and is used to simulate phase changes such as solid phase epitaxial regrowth (SPER) where crystalline orientation plays an important role.

- the object kinetic Monte Carlo (OKMC) module is an off-lattice simulator and is used to study defects evolution inside a solid. A presentation of this module can be found in [Martin-Bragado *et al.* 2013].

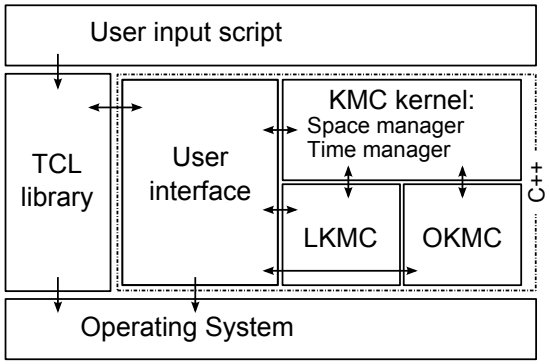

Figure 1.19: Block structure of the MMonCa simulator.

The simplified structure of the MMonCa simulator is shown in Fig. 1.19. The user launches a simulation through an input script containing TCL commands and special commands that are internally mapped with MMonCa C++ methods in order to carry out a dedicated task (initialize the simulation domain, simulate an anneal, etc.).

1.3 Goal of this work

The goal of this thesis is to model junction formation through SPER by means of an atomistic lattice kinetic Monte Carlo method. Chapter 2 explains the model for intrinsic silicon and its capabilities to predict faceting and twin defects generation that may play an important role in junction formation of advanced devices. Chapter 3 generalizes the model to take into account the influence of non–hydrostatic stress that strongly impacts the recrystallization kinetics. Finally, in chapter 4 the influence of dopant impurities is introduced into the model. The final chapter summarizes this dissertation and suggests future directions of research.

CHAPTER 2

Solid Phase Epitaxial Regrowth of intrinsic silicon

In this chapter, the solid phase epitaxial regrowth (SPER) of intrinsic silicon is discussed. In section 2.1, we start by reviewing the thermodynamics and kinetics of the recrystallization process and then we focus on the regrowth anisotropy and twin defects formation that are characteristics of SPER. Based on these observations, we introduce in section 2.2 the lattice kinetic Monte Carlo (LKMC) model of SPER that has been implemented in the MMonCa simulator and is used in the frame of this PhD. This model is then used to study single–directional and multi–directional SPER in sections 2.3 and 2.4 respectively. Single–directional SPER refers to the regrowth of a planar amorphous/crystalline interface proceeding vertically and therefore involving a single regrowth front. It is important to get insight into the physical phenomena and highlight the differences between different crystalline orientations. Nevertheless it does not correspond to the situation existing in electronic devices where SPER proceeds through various regrowth fronts and is thus multi–directional. In particular we show that the LKMC model reproduces the experimental observations of the regrowth of an amorphous region with a low processing temperature in FDSOI MOSFETs. Finally in section 2.5, we summarize this chapter and outline possible future developments.

Contents

2.1 Background

As has been presented in the previous chapter, amorphous silicon (α-Si) reorders through Solid Phase Epitaxial Regrowth (SPER) from a crystalline seed upon thermal annealing (see Fig. 1.10a). For more than 50 years, SPER has been attracting considerable attention not only because of its technological importance but also because of its scientific interest. Many experimental and theoretical studies have been carried out in order to get insight into its kinetics and to identify the microscopic mechanisms of recrystallization. In section 2.1.1, we will review the thermodynamics and kinetics of crystallization processes and present how the regrowth rate can be expressed within the framework of transition state theory (TST)[1].

2.1.1 Thermodynamics and kinetics of crystallization

2.1.1.1 Thermodynamics of amorphous to crystalline transition

At standard temperature and pressure conditions, silicon atoms arrange into a diamond cubic crystal structure where each atom is covalently bonded to four neighbors. Indeed, to minimize the overall energy, $3s$ and $3p$ silicon orbitals hybridize to form four tetrahedral sp^3 orbitals [Ashcroft & Mermin 1976]. Crystalline phase is therefore the lowest energy form of silicon. Amorphous silicon (α-Si) is formed by introducing long–range disorder in the silicon lattice and can be obtained experimentally by different methods such as rapid quenching, ion implantation or low temperature deposition. Its structure has been the subject of experimental and theoretical studies for many years. It can be described as a covalently bonded fourfold coordinated continuous random network (CRN) where the angles between bonds diverge from the ideal tetrahedral angle while bond lengths are only slightly distorted [Zachariasen 1932]. Experimental data based on high–energy x–ray and neutron diffraction measurements give an average bond angle distortion ($\Delta\theta$) of 9–10° [Laaziri *et al.* 1999] whereas data extracted from Raman spectroscopy give a larger range of 9–12° [Kail *et al.* 2010]. CRN models based on bond–swapping algorithm have been shown to be able to reproduce the experimental radial distribution function (RDF) of α-Si and α-Ge [Wooten *et al.* 1985, Barkema & Mousseau 2000]. Nevertheless, in a recent paper, Treacy and Borisenko point out that CRN models fail to explain fluctuation electron microscopy (FEM) data observed by several groups and showing the presence of topological crystallinity in α-Si ordering at the 10 to 20 Å length scale [Treacy & Borisenko 2012]. They suggest instead that a paracrystalline model is consistent with both FEM and RDF data. The real structure of α-Si also exhibits complex features that depend on the preparation conditions as well as on the thermal history. In particular, it should be noted that strong differences may arise between hydrogenated (α-Si:H) and pure

[1] Strictly speaking we use the transition state theory within the harmonic approximation as discussed in section 1.2.2.1.

(α-Si) amorphous silicon. In this manuscript, we will mainly focus on α-Si produced by ion–implantation.

Beyond the discussion about the structural topology of amorphous silicon, it is clear that α-Si always has a higher Gibbs free energy (G_a) than c-Si (G_c) and exists as a kinetically frozen metastable phase. As a consequence, the transition from an amorphous state to a crystalline state is thermodynamically favorable since it results into a reduction of the crystallization free energy $\Delta G_{ac} \equiv G_a - G_c$ defined as:

$$\Delta G_{ac}(T) = \Delta H_{ac}(T) - T\Delta S_{ac}(T), \tag{2.1}$$

where ΔH_{ac} and ΔS_{ac} are the crystallization enthalpy and entropy respectively. ΔG_{ac} can therefore be determined by evaluating the crystallization enthalpy and entropy. Both are calculated from the excess specific heat of amorphous phase ($c_{p,a}$) with respect to crystalline phase ($c_{p,c}$) $\Delta c_p \equiv c_{p,a} - c_{p,c}$ that can be measured by differential scanning calorimetry (DSC) [Roura *et al.* 2011]. The crystallization enthalpy is given by:

$$\Delta H_{ac}(T) = \Delta H_{ac}(T_0) + \int_{T_0}^{T} \Delta C_p(T')\,\mathrm{dT}', \tag{2.2}$$

where $\Delta H_{ac}(T_0)$ is the heat released during crystallization at T_0. Similarly, the crystallization entropy is given by:

$$\Delta S_{ac}(T) = \Delta S_{ac}(T_0) + \int_{T_0}^{T} \frac{\Delta C_p(T')}{T'}\,\mathrm{dT}'. \tag{2.3}$$

Donovan *et al.* have performed DSC measurements on amorphous layers produced by ion–implantation of (100)–oriented single–crystal Si and have determined a crystallization enthalpy of 11.9 $\pm$ 0.7 kJ/mol (at 960 K) [Donovan *et al.* 1985]. In the same work, they have also carried out a calorimetric study of crystallization in amorphous germanium (α-Ge) and observed a heat release prior to crystallization suggesting that α-Ge relaxes to an amorphous state of lower free energy. They quantified the total relaxation enthalpy ΔH_{relax} = 6.0 kJ/mol and found a crystallization enthalpy of 11.6 $\pm$ 0.7 kJ/mol (at 750 K). More recent calorimetric measurements of Roorda *et al.* evidenced that, similarly to α-Ge, α-Si is also subject to structural relaxation [Roorda *et al.* 1989, Roorda *et al.* 1991]. They reported ΔH_{relax} = 3.7 kJ/mol and ΔH_{ac} = 11.7 kJ/mol in [Roorda *et al.* 1989] and ΔH_{relax} = 5.3 kJ/mol and ΔH_{ac} = 13.7 kJ/mol in [Roorda *et al.* 1991], at 500°C. Their study indicated that structural relaxation is related to a lowering of the strain energy stored in distorted bonds in the amorphous lattice (*i.e.* a rearrangement of the whole amorphous network), in good agreement with previous Raman spectroscopy measurements [Kail *et al.* 2010]. This suggests that the relaxed state corresponds to a microscopic configuration where the bond angle distortion is minimum. Kail *et al.* reported that $\Delta\theta \approx 9^\circ$ for relaxed α-Si which corresponds to the lowest value mentioned above. As a comparison, in their experiment, $\Delta\theta \approx 12^\circ$ for unrelaxed α-Si obtained by ion–implantation. Interestingly, Custer *et al.* determined that both relaxed and unrelaxed α-Si formed by ion–implantation exhibit a 1.8 $\pm$ 0.1% lower density with respect to c-Si [Custer *et al.* 1994], confirming the observation of Roorda *et al.* [Roorda *et al.* 1991].

Since the values of crystallization enthalpies for silicon reported by Donovan *et al.* and Roorda *et al.* are very close, it might be tempting to think that they correspond to a minimum energy for α-Si, that can be reached after relaxation. However, Kail *et al.* have recently shown that ΔH_{ac} vary between 5.6 and 13.5 kJ/mol for relaxed α-Si, depending on preparation conditions [Kail *et al.* 2011]. Therefore, ΔH_{ac} should be written as the sum of two contributions

U_{strain} (internal energy due to bond strain) and $U_{defects}$ (internal energy due to structural defects) [Roura *et al.* 2008]:

$$\Delta H_{ac} \approx U_{strain} + U_{defects} = K_{\Delta\theta} \left(\Delta\theta\right)^2 . \tag{2.4}$$

The expression of $K_{\Delta\theta}$ in Eq. 2.4 is detailed in [Roura *et al.* 2008]. Roura *et al.* predicted a defect–free crystallization energy of 7 kJ/mol, which is very close to the lower bound of the crystallization enthalpy determined experimentally in [Kail *et al.* 2011]. It implies that the excess enthalpy with respect to the minimum crystallization enthalpy is the contribution of structural defects and, for ion–implanted α-Si, scales as 6 kJ/mol. However, the nature of these structural defects remains unclear.

Another important point concerns the evolution of Δc_p with temperature which is required to determine ΔH_{ac} and ΔS_{ac} using Eq. 2.2 and 2.3 respectively. Most of the available data of Δc_p in α-Si are performed at cryogenic temperatures (< 100 K). However, Roura *et al.* reported measurements of the excess specific heat of α-Si over a wide temperature range (100–900 K) [Roura *et al.* 2013]. They found that Δc_p becomes negligible in relaxed α-Si suggesting that crystallization enthalpy and entropy can be considered temperature independent for temperatures above 100 K. Below 100 K, they estimated a maximum variation of 0.02 kJ/mol for ΔH_{ac} and 0.4 J/K/mol for ΔS_{ac}. They also discussed the determination of the crystallization entropy, based on the theoretical calculation of Spaepen (ΔS^0_{ac}) using a defect–free model of α-Si who reported a value of 1.7 J/K/mol at 0 K [Spaepen 1974]. The value of the entropy at a single temperature T can be calculated using Eq. 2.3. However, in the case of ion–implanted α-Si, we pointed out the presence of structural defects that will cause an increase of the crystallization entropy. We note $\Delta S_{defects}$ this additional contribution due to structural defects:

$$\Delta S_{ac} = \Delta S^0_{ac} + \Delta S_{defects} \tag{2.5}$$

where $\Delta S_{defects} = -Rn_{defects} \log\left(n_{defects}\right)$, with R the gas constant and $n_{defects}$ the defects density. Roura *et al.* estimated a $n_{defects}$ = 1.7% to explain the excess crystallization enthalpy observed in ion–implanted α-Si, giving $\Delta S_{defects}$ = 0.58 J/K/mol. Finally, the values of ΔH_{ac} and ΔS_{ac} can be used to determine the excess Gibbs free energy of α-Si using Eq. 2.1. In particular, the intersection of ΔG_{ac} with the free energy of liquid Si, ΔG_{lc}, corresponds to the melting point of α-Si and is predicted to be lower than for c-Si, in good agreement with experimental observations [Roura *et al.* 2013, and references therein]. Another interesting conclusion is that structural defects lead to a lowering of the melting point with respect to defect–free α-Si.

2.1.1.2 Kinetics of Solid Phase Epitaxial Regrowth (SPER)

The thermally activated crystallization process of α-Si is shown schematically in Fig. 2.1. As it has been mentioned above, α-Si exhibits a structural relaxation phenomenon resulting in a lowering of its excess free energy represented by the dashed red line. If crystalline and amorphous phases coexist in a solid and are separated by a coherent solid–solid α/c interface, a phase transformation from α-Si to c-Si can occur if the temperature is high enough to overcome the energy barrier (ΔG^*) between amorphous and crystalline states. The growth rate corresponding to the crystallization of α-Si can be expressed using transition state theory as [Olson & Roth 1988, Laidler & King 1983]:

$$v = v_0 \times \exp\left(-\frac{\Delta G^*}{k_B T}\right) . \tag{2.6}$$

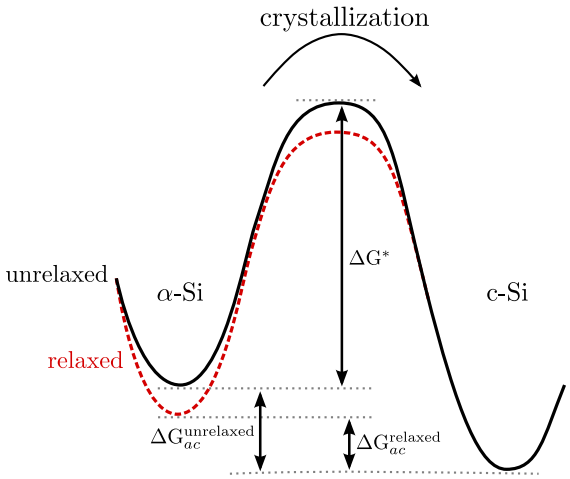

Figure 2.1: Schematic of the energetics of SPER. Unrelaxed α-Si (plane line) typically formed after ion–implantation releases enthalpy during low–temperature annealing through a phenomenon called structural relaxation (dashed line).

The prefactor v_0 can be made explicit [Lu *et al.* 1991]:

$$v_0 = f\lambda\nu \times \left[1 - \exp\left(-\frac{\Delta G_{ac}}{k_B T}\right)\right], \tag{2.7}$$

where f is a geometric factor (see section 2.1.2), λ is the local distance the interface moves per atomic rearrangement, $\nu \equiv k_B T/h$ is an effective normal mode frequency leading to rearrangement and ΔG_{ac} is the change in free energy per atom crystallized (in eV) and has been discussed previously. In ion–implanted α-Si, neglecting the entropic contribution, $\Delta G_{ac} \approx \Delta H_{ac}$ scales between 0.12 and 0.2 eV depending on the relaxation state of the amorphous phase and on the structural defects density [Donovan *et al.* 1985, Roorda *et al.* 1991]. In the general case, the free energy of activation from α-Si to c-Si can be written as [2] $\Delta G^* \equiv E^* - T\Delta S^*$ where E^* is the activation energy and ΔS^* is the activation activation entropy, such as Eq. 2.6 becomes:

$$v = v_0 \times \exp\left(\frac{\Delta S^*}{k_B}\right) \times \exp\left(-\frac{E^*}{k_B T}\right). \tag{2.9}$$

It turns out that, neglecting the temperature dependence of v_0 and ΔS^*, Eq. 2.9 can be expressed phenomenologically by an Arrhenius equation, $v = A \times \exp\left(-E^*/k_B T\right)$. Therefore, $E^* \equiv -k_B \partial\left(\log v\right)/\partial\left(T^{-1}\right)$ can be extracted experimentally from a temperature–dependent experiment where v is measured as a function of T. In the case of SPER, the regrowth rate can be evaluated by measuring the velocity of the displacement of the α/c interface which proceeds in a layer–by–layer epitaxial growth mode from amorphous to crystalline (see Fig. 1.10a). Various experimental techniques such as Rutherford backscattering spectrometry (RBS) and ion channeling measurements [Csepregi *et al.* 1978] or *in–situ* time resolved reflectivity (TRR)

[2] Strictly speaking, $\Delta G^* \equiv \Delta H^* - T\Delta S^*$ where ΔH^* is the activation enthalpy and ΔS^* is the activation activation entropy. Within the framework of transition state theory, the relationship between the activation energy (E^*) and the activation enthalpy for bimolecular reaction is given by [Atkins 1986]:

$$E^* = \Delta H^* + k_B T. \tag{2.8}$$

However in the case of crystallization $\Delta H^* \gg k_B T$, hence $k_B T$ can be dropped in Eq. 2.8, yielding $E^* \approx \Delta H^*$ and $\Delta G^* \equiv E^* - T\Delta S^*$.

Table 2.1: Experimental measurements of the activation energy of SPER of silicon reported by different authors.

Reference	Characterization technique	Temperature range	E^*
[Csepregi *et al.* 1978]	RBS	450–575 °C	2.3±0.03 eV
[Olson & Roth 1988]	*in–situ* TRR	500–1000 °C	2.68±0.05 eV
[Roth *et al.* 1990]	*in–situ* TRR	500–750 °C	2.7±0.02 eV
[McCallum 1996]	*in–situ* TRR	480–660 °C	2.7 eV

[Olson & Roth 1988, Roth *et al.* 1990, McCallum 1996] have been used by different research groups to measure the regrowth velocity at different temperatures on α-Si films formed by self–ion implantation into c-Si in order to determine E^* (see Table 2.1). It should be emphasized that *in–situ* TRR presents an advantage over *ex–situ* measurements since it allows to avoid temperature variations due to the regrowth evolution when the sample is removed from the furnace. It has also been shown that the presence of impurities can significantly affect the regrowth kinetics and may result in a scattering of the measured E^* depending on experimental conditions [Olson & Roth 1988]. In particular, hydrogen can diffuse from the surface oxide into the α-Si film and cause a retardation of the regrowth rate [Roth *et al.* 1990]. A contamination by C, O and N impurities can also occur during ion–implantation due to CO^+ and N_2^+ ions and has been shown to result in a defective regrowth [Narayan 1982]. The measurements of Roth *et al.* [Roth *et al.* 1990] and McCallum [McCallum 1996] (see Table 2.1) in hydrogen–free conditions provide an activation energy of 2.7 eV.

2.1.1.3 Kinetics of Random Nucleation and Growth (RNG)

Up to now we have been dealing with layer–by–layer epitaxial crystallization phenomena occurring through SPER at an α/c interface. However, as has been mentioned in the previous chapter, crystallization can also take place inside the amorphous phase through a random nucleation and growth (RNG) process and resulting in a polycrystalline material (see Fig. 1.10b). It is therefore of interest to understand the kinetics of RNG. In contrast to SPER that proceeds at a pre–existing planar α/c interface, RNG involves two phenomena: (i) the random nucleation of small crystalline clusters surrounded by amorphous material and (ii) the monotonic growth of these crystalline seeds into crystallites. The stability of the crystalline nucleus containing i atoms is determined by its free energy $\Delta G(i)$ given by [Spinella *et al.* 1998]:

$$\Delta G(i) = -\left(\Delta G_{ac} - \Delta G_{el}\right) i + \sigma_{ac} O_i, \tag{2.10}$$

where ΔG_{ac} is the free energy change during the amorphous to crystalline transition which has been discussed previously, ΔG_{el} is a free energy relative to elastic expansion but can be dropped since $\Delta G_{ac} \gg \Delta G_{el}$, σ_{ac} is the interfacial free energy due to bond distortions of the atoms located at the surface of the agglomerate and O_i is the number of atoms located at the nucleus interface. $\Delta G(i)$ increases with the cluster size and reaches a maximum ΔG^* (the nucleation barrier) at a critical cluster size i^*. For a homogeneous nucleation process:

$$\Delta G^* = \frac{16\pi}{3} \frac{\sigma_{ac}^3}{\Delta G_{ac}^2} \tag{2.11}$$

After the crystalline agglomerates have reached the critical nucleus size i^*, they exhibit a monotonical growth into crystallites resulting in a polycrystalline material with randomly oriented grains. A review of the theoretical dependence of the kinetic parameters r_n (the nucleation rate) and r_g (the growth rate) is given in [Spinella *et al.* 1998, and references therein].

Kail *et al.* have shown that RNG can be described by the Kolmogorov–Johnson–Mehl–Avrami (KJMA) model and the crystallization rate is given by [Kail *et al.* 2012]:

$$r_c = (r_n r_g^3)^{1/4} \equiv r_{c0} \times \exp\left(-\frac{\Delta E_c}{k_B T}\right), \tag{2.12}$$

where r_{c0} and ΔE_c are the crystallization pre–exponential factor and activation energy respectively. RNG process is therefore described by a single activation energy which has been reported to be 3.65±0.10 eV by Kail *et al.*, in good agreement with the value of 4 eV obtained in [Olson & Roth 1988]. Interestingly, it should be expected a dependence of the activation energy with the crystallization enthalpy because $\Delta E_c \propto \Delta G^*$. However, Kail *et al.* observed the same crystallization kinetics between samples with different crystallization enthalpies (they reported a variation of the crystallization enthalpy between 5.6 and 13.5 kJ/mol for relaxed α-Si depending on the on the α-Si material [Kail *et al.* 2011]). They proposed that the discrepancy between experimental results and classical nucleation theory arises from the fact that nucleation begins in microscopic inhomogeneities in α-Si which would be consistent with a paracrystalline structure of the amorphous network [Treacy & Borisenko 2012].

Finally, from the values of activation energy for RNG with respect to SPER, it turns out that, in the presence of a pre–existing planar α/c interface, crystallization will proceed through SPER and the contribution of RNG can be neglected. This is particularly true in the temperature range considered in the low thermal budget process (T $\leqslant$ 650°C) because the nucleation barrier (Eq. 2.11) is too high and nucleation probability remains very low. However it should be pointed out that in certain cases, SPER can become very slow and the contribution of RNG appears as non negligible if the temperature is sufficiently high. For example, this has been observed by Duffy *et al.* for the regrowth of sub–20 nm wide silicon fin field-effect transistors (FinFETs) that is limited by {111} faceting. The slow regrowth kinetics gave rise to the formation of polycrystalline silicon in the non–recrystallized region after a 1050 ∘C rapid thermal annealing (RTA) while it remained amorphous after a 600 ∘C, 60 s annealing [Duffy *et al.* 2007].

2.1.2 Anisotropy and defects formation

Experimental observations of SPER on Si and Ge have shown that recrystallization speed exhibits a strong orientation dependence. It has been reported a variation of the regrowth velocity within a range of 24:7:1 for Si along ⟨100⟩, ⟨110⟩ and ⟨111⟩ direction respectively [Csepregi *et al.* 1976, Csepregi *et al.* 1978, Narayan 1982] and 15:10:1 for Ge [Csepregi *et al.* 1978, Darby *et al.* 2013]. On the other hand, no difference has been observed in the calculated activation energy, respectively 2.7 eV and 2.17 eV for Si and Ge, suggesting that the nature of the atomistic processes involved during SPER is independent of the lattice orientation. It turns out that SPER is controlled by interface reaction kinetics which rules out the models based on a bulk diffusion mechanism (the interested reader is referred to [Lu *et al.* 1991] for a more complete discussion). It should also be emphasized that the recrystallization process is defect–mediated giving rise to a question regarding the microscopic nature of this defect (see [Lu *et al.* 1991] for further details).

Considering the expression of the regrowth rate given by Eq. 2.6, the orientation dependence should affect the prefactor v_0 (Eq. 2.7). Csepregi *et al.* have introduced a $\sin\theta$ term (such as $v_0 \propto \sin\theta$), where θ is the angle between the regrowth direction and the ⟨111⟩ direction [Csepregi *et al.* 1978] to explain the anisotropic behavior of SPER. Nevertheless, we prefer to present the phenomenological model of Drosd and Washburn [Drosd & Washburn 1982]

because it contains a deeper physical insight into the origin of anisotropy and constitutes the basis of the LKMC model used during this PhD. In their model, the atomistic structure of the amorphous phase is not described and the recrystallization mechanism is based on the assumption that "for an atom to attach successfully to the crystal it must complete at least two undistorted bonds", where an undistorted bond corresponds to a bond with the length and angle of the crystalline phase (respectively $\sqrt{3}a_0/4$ and 109.5° with a_0 being the lattice constant). The basic building block of this model is the incorporation of $\langle 110 \rangle$ chains in the crystalline phase which leads to the completion of a sixfold ring, characteristic of crystalline structure in diamond cubic lattices. A schematic representation of this model is given in Fig 2.2. It appears that the number of $\langle 110 \rangle$ chains involved in the recrystallization process depends on the regrowth plane. The regrowth of a $\{100\}$ plane is straightforward and involves only one atom. In contrast, during $\{110\}$ and $\{111\}$ recrystallization, respectively two and three atoms have to be incorporated to complete the sixfold ring. Considering the different permutations and combinations occuring during the regrowth of $\{100\}$, $\{110\}$ and $\{111\}$ planes, Narayan has calculated the theoretical velocity ratios and obtained an excellent agreement with the ratios observed experimentally [Narayan 1982]. The geometric factor f in the expression of the prefactor v_0 is orientation dependent and corresponds physically to the fraction of sites available for recrystallization. A deeper analysis of the implications of this model can be found in [Drosd & Washburn 1982, Narayan 1982]. Additional insight will also be provided in section 2.2 where this model is used within an atomistic lattice Kinetic Monte Carlo (LKMC) approach in order to provide a microscopic description of the phenomena occuring at the α/c interface during SPER. Interestingly, molecular dynamics calculations of Lampin and Krzeminski have also evidenced the mechanisms proposed by Drosd and Washburn at the atomic level [Lampin & Krzeminski 2009].

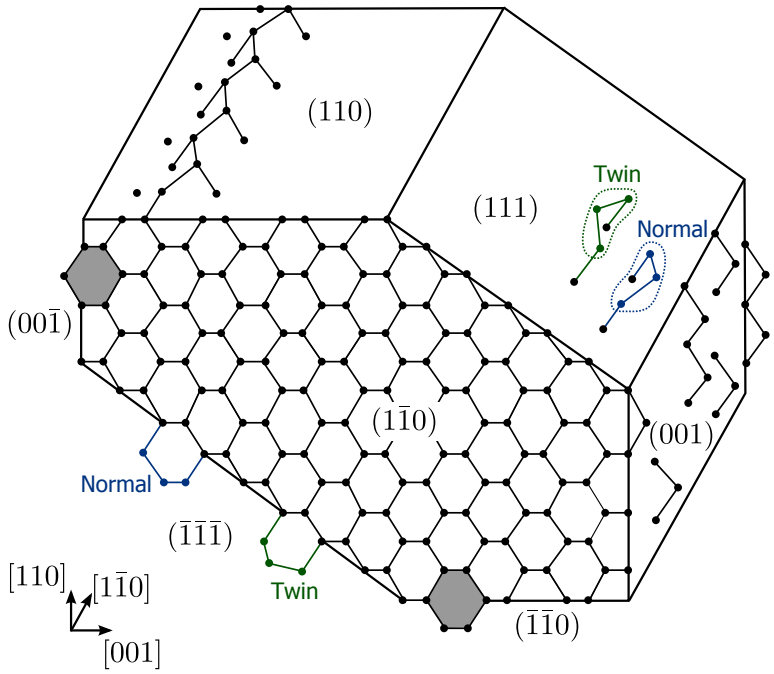

Figure 2.2: Three–dimensional schematic of the phenomenological model of Drosd and Washburn [Drosd & Washburn 1982]. Twin and normal configurations are also represented for the regrowth of $\{111\}$ planes.

Another important phenomenon occuring during SPER is the formation of defects which have been observed experimentally [Csepregi *et al.* 1978, Drosd & Washburn 1982, Narayan 1982]

and are attributed to the formation of twins in {111} planes [Jones *et al.* 1988]. Within the model of Drosd and Washburn, twins can initiate during {111} regrowth because the completion of the sixfold ring gives rise to various possibilities in the crystalline arrangement without breaking first neighbor distances and the angles between bonds as shown in Fig. 2.3. The

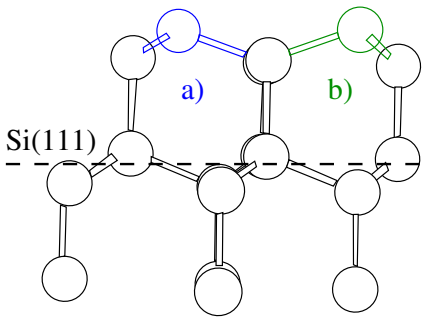

Figure 2.3: (a) Normal and (b) twin configurations lying on a Si(111) plane. The figure is retaken from [Martin-Bragado & Sklenard 2012].

direct consequence is that both normal and twin regrowth may occur on {111} planes with equal probabilities. It results in a highly defective SPER of (111) substrates, in good agreement with experimental observations [Csepregi *et al.* 1976]. In contrast, twins cannot initiate on {110} and {100} planes. However, defective regrowth of (100) or (110) substrates may result from interface fluctuations which cause local {111} planes to appear where twinning can initiate. Impurities having a high affinity for Si or Ge have also been shown to act as nucleation sites for twins [Narayan 1982]. Twinning has been pointed out to play a determinant role in the regrowth velocity of planar α/c interfaces [Csepregi *et al.* 1976] and during the SPER of rectangular shaped amorphous regions [Cerva & Küsters 1989]. This point will be largely discussed in section 2.2, based on the simulation results obtained with the SPER LKMC model.

2.2 LKMC model

The Kinetic Monte Carlo method has been used to describe the microscopic processes occurring during Solid Phase Epitaxial Regrowth at the α/c interface. The model assumes an atomistic representation of the α/c interface where the atoms are placed at the lattice site positions and a flag is used to distinguish among atoms in the crystalline phase with those in the amorphous phase. The atomistic structure of the amorphous phase is ignored and only the amorphous to crystalline transitions are described. This simplification is justified since SPER takes place at the α/c interface, as discussed previously (see section 2.1.2). The rate of a recrystallization event corresponds to the probability per unit time for an atom in the amorphous phase to join the crystalline phase. The algorithm picks up randomly a recrystallization event from the list of possible transitions with a probability proportional to its rate. The clock is then incremented by a random time which is consistent with the average time required to escape from that state (see section 1.2.2). The evolution from state to state leads to a progressive displacement of the α/c interface that can be analyzed at the atomistic scale. The purpose of this LKMC model is to describe the anisotropic behavior of SPER and defect formation. The details of the model permitting to take into account these two aspects of SPER will be described in sections 2.2.1 and 2.2.2 respectively.

2.2.1 Anisotropic growth

The description of LKMC events is based on the phenomenological picture of SPER proposed by Drosd and Washburn which has been presented in section 2.1.2 [Drosd & Washburn 1982]. This leads naturally to the definition of three main configurations for {100}, {110}, and {111} local orientations depending on atoms at the α/c interface forming two undistorted bonds or needing one or two extra atoms to form them. The same approach has been used in the work of Martín-Bragado which corresponds to the SPER model implemented in the commercial simulator Synopsys Sentaurus Process KMC [Martin-Bragado & Moroz 2009] and later in MMonCa [Martin-Bragado 2011]. Nevertheless, we should stress that the introduction of defective configurations into the model leads to results with more physical insight that can have a significant technological impact.

2.2.1.1 Implemented model

The model that will be described in this section has been implemented in the LKMC module of the MMonCa simulator. Three microscopic local configurations {100}, {110}, and {111}

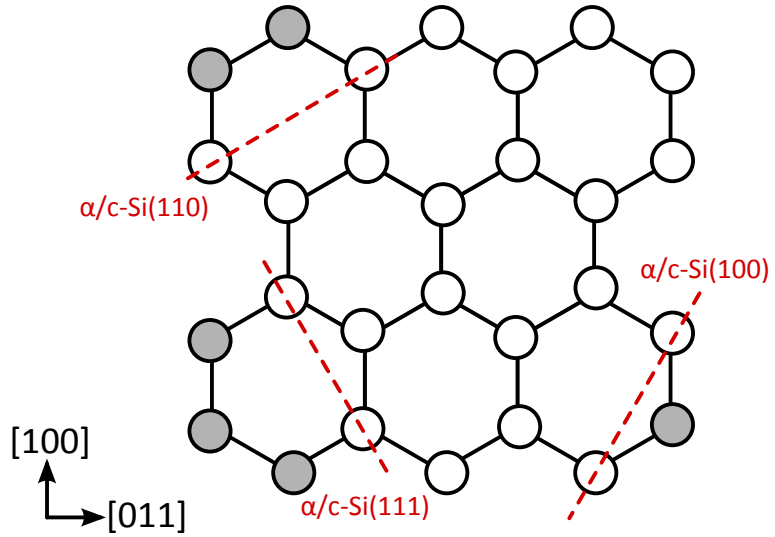

Figure 2.4: Schematic of the atomistic configurations for {100},{110} and {111} local configurations. Atoms in the crystalline phase are white and those in the amorphous phase are grey.

are considered by the model as shown schematically in Fig. 2.4. The local regrowth plane is determined by the neighborhood of the considered configuration in order to complete a sixfold ring so that {100}, {110} and {111} local configurations require respectively one, two and three atoms to be incorporated into the crystalline phase. In the case of the {100} configuration, we introduce a distinction between lowly $\{100_l\}$ and highly $\{100_h\}$ coordinated sites depending on the number of first and second neighbors. This allows a better control of the the α/c interface that will be discussed in section 2.2.1.3.

$$\nu_0(n,T) = K(n) \times \exp\left(-\frac{E^*}{k_B T}\right) \tag{2.13}$$

where $K(n)$ is the site dependent prefactor, E^* the activation energy, k_B is the Boltzmann constant and T the temperature. The values of the different parameters for Si and Ge are summarized in table 2.2 and will be discussed in section 2.3.1.

Table 2.2: Parameters of the LKMC model for silicon and germanium.

Parameter	Si	Ge[a]
E_a (eV)	2.7	2.17
K($\{100\}_l$) ($\times 10^{16}$ events.s^{-1})	3.09	11.8
K($\{100\}_h$) ($\times 10^{17}$ events.s^{-1})	7.42	23.5
K($\{110\}$) ($\times 10^{15}$ events.s^{-1})	2.08	24.1
K($\{111\}$) ($\times 10^{12}$ events.s^{-1})	1.62	1.50

[a]From [Darby *et al.* 2013]

2.2.1.2 Plane detection

To determine the regrowth plane an atom belongs to (*i.e.* $\{100\}$, $\{110\}$ or $\{111\}$), the model builds a list of the first (1NN), second (2NN) and third (3NN) neighbors for each atom. The algorithm computes the distance between the considered atom and the other atoms of the system and uses the cut-off distances summarized in Table 2.3 to select 1NN, 2NN and 3NN atoms, corresponding respectively to $\sqrt{3}/4a_0$, $\sqrt{2}/2a_0$ and $\sqrt{11}/4a_0$, where a_0 is the lattice constant. In the case of diamond lattice materials such as silicon or germanium, an atom has 4, 16, and 24 1NN, 2NN and 3NN respectively. The neighbors list is then used in the SPER model to determine the regrowth plane of an *amorphous* atom. The detection of $\{100\}$ configurations is straightforward and correspond to atoms with two or three crystalline first nearest neighbors[3]. Atoms with only one crystalline first nearest neighbor belongs either to $\{110\}$ or $\{111\}$ configurations. If the considered atom has an *amorphous* neighbor with one crystalline neighbor, then it is part of a $\{110\}$ configuration. In the other cases, the atom belongs to a $\{111\}$ configuration[4].

Table 2.3: First, second and third nearest–neighbor distances for silicon and germanium corresponding respectively to $\sqrt{3}/4a_0$, $\sqrt{2}/2a_0$ and $\sqrt{11}/4a_0$, where a_0 is the lattice constant.

Parameter	Si	Ge
1NN	2.35 Å	2.44 Å
2NN	3.84 Å	3.99 Å
3NN	4.50 Å	4.68 Å

2.2.1.3 The particular case of {100} microscopic configurations

If no distinction is introduced between $\{100\}$ configurations, they will have an equivalent probability to recrystallize which will give rise macroscopically to an interface that is not smooth (see [Martin-Bragado 2012]). However, experimental observations suggest that the α/c interface remains flat with a roughness $\sim$ 8 Å [Lohmeier *et al.* 1994] which is similar to the molecular dynamics simulations results of Gärtner and Weber [Gärtner & Weber 2003]. Thus, the distinction among $\{100_l\}$ and $\{100_h\}$ configurations constrains the model to produce an atomically flat $\{100\}$ α/c interface during SPER. They are respectively defined such as $c1NN + c2NN \leqslant 8$ and $c1NN + c2NN > 8$. Although the threshold between the two configurations is quite arbitrary, the fact to consider second nearest neighbors is necessary to

[3]An atom with four crystalline first nearest neighbor is by definition *crystalline*.
[4]In reality, the algorithm also checks that the $\{111\}$ configuration forms a sixfold ring.

allow the detection of any local variation of the α/c interface. It turns out that the rate of $\{100_h\}$ configurations has to be chosen high with respect to $\{100_l\}$ configurations in such a way that the regrowth of $\{100\}$ surfaces is limited by $\{100_l\}$ events while $\{100_h\}$ events control the roughness of the interface. This atomistic picture follows the model of Williams and Elliman which considers that sites with greater crystalline coordination are preferential sites for recrystallization [Williams *et al.* 1985]. Physically it can be interpreted by the fact that the regrowth process will tend to reduce the interfacial free energy σ_{ac} and therefore force the recrystallization to proceed layer by layer in order to limit the interface roughness. Nevertheless, it should be pointed out that the distinction between the two $\{100\}$ events remains an artificial way to take into account the interface energy which fits well with the necessity to get a computationally efficient atomistic model compatible with technological requirements. Alternatively, another approach relying on interface energies in the calculation of the transition rates could be drawn in order to improve the physical insight of the model. However, it would require to be able to evaluate the force between atoms (using for example an interatomic potential) and develop the theoretical framework to modify the transition rates accordingly. Beyond its complexity, this method would happen to be much more expensive, limiting the simulation time and the size of the system that can be studied and therefore its technological interest.

2.2.2 Defect formation

The particularity of the LKMC model implemented in MMonCa resides in the fact that it can simulate SPER induced defects. Previous works assumed a generic defect being formed as the result of $\{111\}$ local recrystallizations by placing a tag on such positions to reconsider the coordination of neighboring atoms, but otherwise leaving the atom with exactly the same coordinates as a perfect atom in the lattice would have [Martin-Bragado 2012, Martin-Bragado 2011]. This assumption allowed indeed to reproduce various behaviors related to regrowth defect formation but the lack of physical insight of this approach caused sever limitations in the prediction capability of the model. In contrast, the model presented here detects and places twins in their lattice positions. This is shown in the Fig. 2.3 representing a regular (a) and twin (b) configuration lying on a Si(111) plane. The use of the realistic (b) configuration not only improves the physics of the system being simulated but also opens the possibility of simulating the interaction of the different crystallographies when one twin orientation meets another.

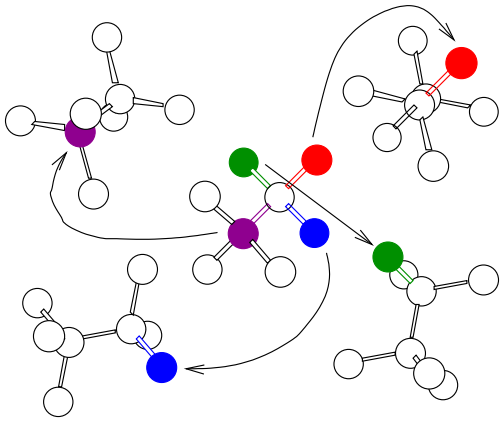

Figure 2.5: Look up configurations, from [Martin-Bragado & Sklenard 2012]. The center shows the substrate configuration surrounded by its twins. The twins are formed by the 60° rotation around one bond of the tetrahedron, and are displayed with different colors.

Fig. 2.5 contains all the valid configurations representing the substrate lattice and all its

twin configurations used by the simulator. The configuration at the center of Fig. 2.5 represents the original substrate lattice. The surrounding configurations are the associated twins for each of the four bonds of the tetrahedron. The atoms and bonds used as the rotation axis (and thus not changing) have been displayed. A twin is seen as a 60° rotation with respect to one bond in the original tetrahedron. After the initial substrate is provided, our model detects the local orientations using first and second neighbor distances and grows the crystal by picking the right match in the configuration table. For {100} and {110} local configurations surrounded by perfect crystal, there is only one match. But for {111} local configurations there are actually two matches: the current orientation and the twin orientation (see Fig. 2.3). In both of them the bond to the crystal is the same, but the rest of the tetrahedron is not specified and accepts the rotation of 60° contained in the twin configuration. Under these circumstances, one of the two configurations is randomly picked. If the twin is chosen, subsequent recrystallization of neighboring atoms detects it and attaches to the α/c interface with such orientation, extending it. Finally, when regular and twin nano-crystals meet, none of the two configurations are to be detected: atoms in such conditions are defects. Consequently a twin region is not defective *per se*, only the stacking faults are created at the intersection of different regions.

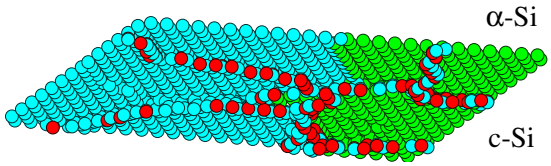

Figure 2.6: Atomistic view of the simulated α/c interface and defect formation after few nanolayers of Si(111) recrystallization, from [Martin-Bragado & Sklenard 2012]. Regular (blue) and twin (green) nano-islands form the α/c interface, leaving lines of defects (red and blue), and forming stacking faults behind.

Fig. 2.6 shows the formation of such defects in a Si(111) plane. Only the α/c interface and the defects are shown. The particular geometry of Si(111) allows the growth of both regular (blue) and twin (green) areas. When a regular and a twin island join, a defect is formed. The recrystallization continues, but leaving a track of heavy defective silicon. According to the simulations, such defective silicon consists of a network of stacking faults (red atoms below the recrystallized surface) that are the boundaries of normal and twin nano-crystals.

2.3 Planar regrowth

2.3.1 Model calibration

The model has been calibrated to reproduce experimental regrowth velocity of amorphous layers on (100), (110) and (111) crystalline Si (or Ge). Simulations have been carried out using a simulation cell where y and z are the in–plane directions and x is the regrowth direction as shown in Fig. 2.7. Periodic boundary conditions (PBC) have been applied along y and z directions. The recrystallization of $\approx$ 25 nm thick α-Si layers was simulated for the different substrate orientations at temperatures ranging from 450 °C to 750 °C. The domains sizes used for each simulation cell are summarized in Table 2.4. It should be noted that the sizes used along y and z direction slightly differ in order to ensure PBC. Fig. 2.8 shows an Arrhenius plot of the simulated regrowth velocity (lines) using the calibration parameters reported in Table 2.2 versus various experimental data from the literature (symbols). The slope of each curve gives the same macroscopic activation energy corresponding to the one used for microscopic events (2.7 eV for Si). The substrate orientation–dependent SPER rates arise from the different values

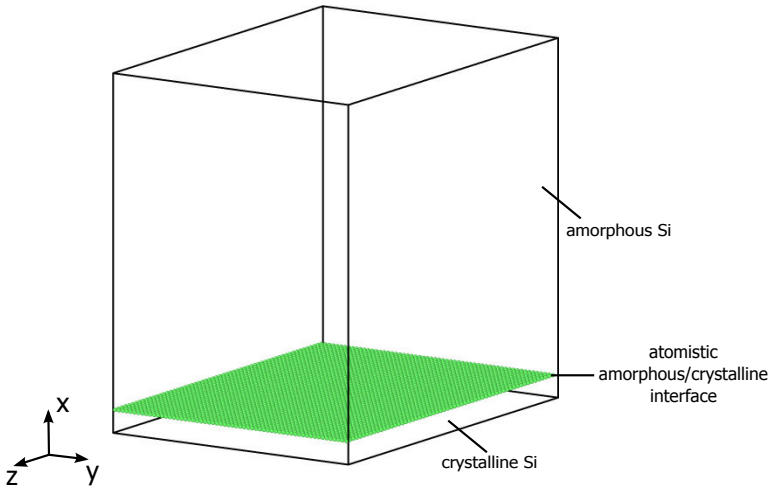

Figure 2.7: Simulation domain.

Table 2.4: Simulation cells sizes used for SPER of (100), (110) and (111) Si substrate with a_0 being the silicon lattice constant (0.5431 nm). Periodic boundary conditions have been applied along y and z directions.

Substrate	x		y		z	
	orientation	size	orientation	size	orientation	size
(100)	[100]	45 nm	[011]	$30\sqrt{2}a_0$	$[0\bar{1}1]$	$30\sqrt{2}a_0$
(110)	[011]	45 nm	[100]	$30a_0$	$[0\bar{1}1]$	$30\sqrt{2}a_0$
(111)	[111]	45 nm	$[\bar{2}11]$	$26\sqrt{6}a_0$	$[0\bar{1}1]$	$45\sqrt{2}a_0$

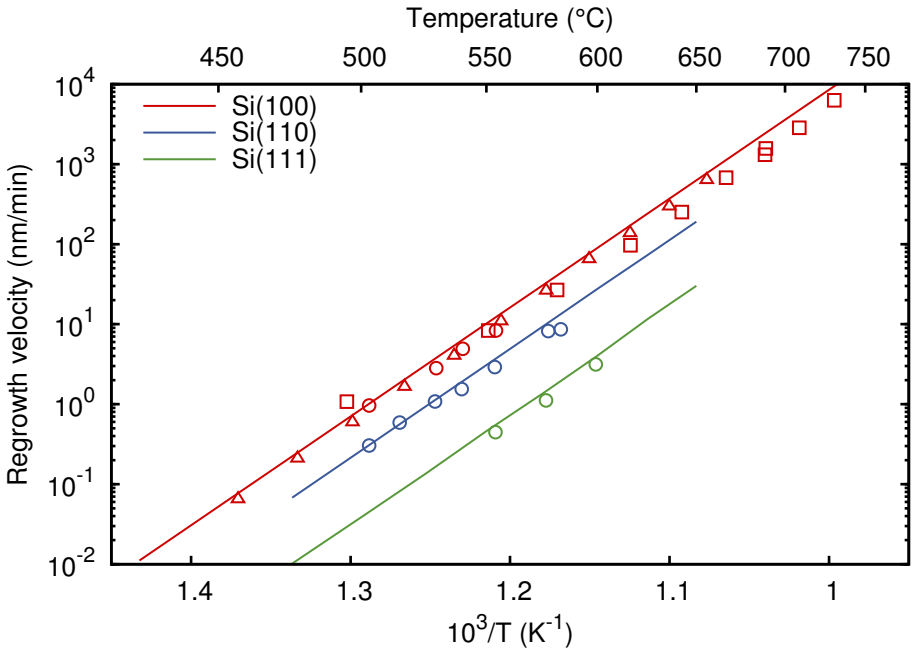

Figure 2.8: Arrhenius plot of the SPER velocity along ⟨100⟩, ⟨110⟩ and ⟨111⟩ directions. Symbols are experimental data from [Roth *et al.* 1990] (□), [Csepregi *et al.* 1978] (○) and [Johnson & McCallum 2007] (△) and lines are our simulations results.

used for the prefactors. However, it should be emphasized that there is no straightforward correlation between microscopic and macroscopic rates.

The model has been used to simulate the SPER along an arbitrary orientation ranging from $\langle 100 \rangle$ to $\langle 011 \rangle$ direction. The simulations have been carried out using a 20 $\times$ 180 $\times$ $26\sqrt{2}a_0$ nm^3 simulation cell with PBC along z direction. The arbitrary orientations are obtained by a rotation θ of a (100) substrate around the $[0\bar{1}1]$ (z) direction. The reference frame is described by the normalized matrix:

$$\boldsymbol{M} = \begin{bmatrix} 1 & 0 & 0 \\ 0 & \frac{1}{\sqrt{2}} & -\frac{1}{\sqrt{2}} \\ 0 & \frac{1}{\sqrt{2}} & \frac{1}{\sqrt{2}} \end{bmatrix}, \tag{2.14}$$

and the rotation matrix around z direction is given by:

$$\boldsymbol{R_z} = \begin{bmatrix} \cos\theta & \sin\theta & 0 \\ -\sin\theta & \cos\theta & 0 \\ 0 & 0 & 1 \end{bmatrix}. \tag{2.15}$$

Finally, the normalized matrix $\boldsymbol{M'}$ describing the system after rotation is given by:

$$\boldsymbol{M'} = \boldsymbol{M}\boldsymbol{R_z}. \tag{2.16}$$

Since θ can be any value between 0 and $\pi/2$, the periodicity along y direction might be lost and PBC cannot be used. As previously, the simulated regrowth velocities were computed by measuring the average recrystallization speed (see appendix A) of 20 nm α-Si at 550 °C. Fig. 2.9 shows the comparison between simulation results (line) and experimental data of Csepregi *et al.* (symbols) [Csepregi *et al.* 1977]. Not surprisingly, the model correctly predicts the regrowth velocity for θ=0°, θ=54.7° and θ=90° corresponding to (100), (111) and (110) orientations respectively. More interestingly, simulation results turn out to be in good agreement with experimental data for any arbitrary orientation. In particular, for orientations between 40° and 70° (around (111) orientation), SPER is controlled by defect formation leading to the rounded shape of the regrowth velocity in Fig.2.9.

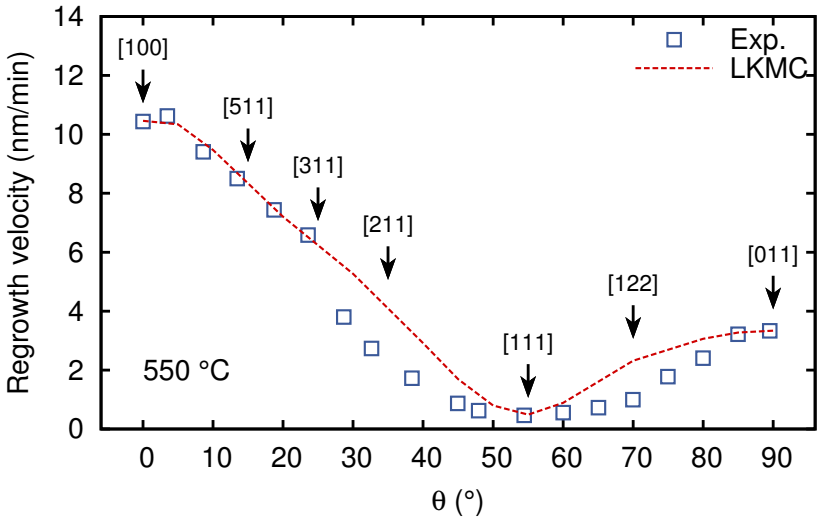

Figure 2.9: Plot of the regrowth velocity at 550 °C as a function of substrate orientation angle θ, from [100] to [011] direction. Symbols are experimental data from [Csepregi *et al.* 1978] and lines are our simulation results.

2.3.2 (100) substrate

Fig. 2.10 shows the topology of the α/c interface for Si(100) regrowth. It can be seen that the interface remains flat, in good agreement with experimental observations [Narayan 1982, Lohmeier *et al.* 1994]. A quantification of the interface roughness gave a value of σ_{if} =

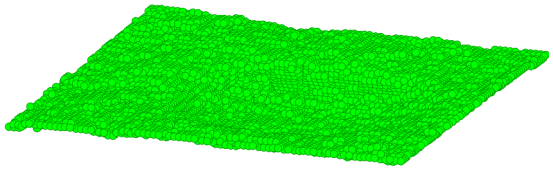

Figure 2.10: Atomistic plot of α/c interface for Si(100) regrowth.

1.8$\pm$0.3 Å using the method detailed in appendix A and can be compared with the experimental value of 8 Å [Lohmeier *et al.* 1994]. First of all, it should be emphasized that the small roughness value obtained in simulation is the direct consequence of the introduction of distinct rates for $\{100_l\}$ and $\{100_h\}$ configurations as it has been described previously. In particular, it allows to improve the description of the fact that SPER proceeds layer by layer where the α/c interface keeps its planar structure. Then, the slight difference with experimental roughness probably arises from the fact that the model cannot describe the real atomistic nature of the α/c interface and considers instead an idealized interface where atoms occupy lattice sites. It is clear that this atomistic picture cannot describe the real situation and a quantum–mechanical treatment would be required. For example, Bernstein *et al.* have studied the α/c interface using tight binding molecular dynamics (TBMD) simulations (*i.e.* the interatomic forces are described by a tight–binding Hamiltonian) and have shown that the transition between amorphous and crystalline regions occurs over a distance of 7 Å [Bernstein *et al.* 1998]. Even if they used a rapid cooling of a molten Si region to produce the amorphous phase which could exhibit a different behavior than the result of an amorphization through ion implantation, their value is in good agreement with experimental measurements. In contrast, the LKMC simulation considers an abrupt transition and will therefore tend to underestimate the interface roughness.

In a microscopic point of view, it turns out that the flatness of the interface gives rise to $\{100\}$ rather than $\{110\}$ or $\{111\}$ local configurations. As a consequence, simulations predict very low defect concentration after SPER completes. This is is excellent agreement with high–resolution electron microscopy (HREM) observations [Jones *et al.* 1988, and references therein].

2.3.3 (110) substrate

SPER of (110) substrates has received less attention that of (100) or (111). Fig. 2.11 shows the topology of the α/c interface for Si(110) regrowth which happens to be more defective than for Si(100) (see Fig 2.10). In particular, the regrowth gives rise to the formation of two types of twins at opposite angles shown in pink and blue in Fig. 2.11.

2.3.4 (111) substrate

As stated previously and shown in Fig. 2.9, the regrowth of (111) substrates is particularly subject to twinning, which strongly influences its regrowth kinetics. Fig. 2.12 shows the comparison of simulated results (symbols) versus experimental growth (solid lines) at 550 °C as reported by [Csepregi *et al.* 1976]. Similar experimental results have also been obtained by

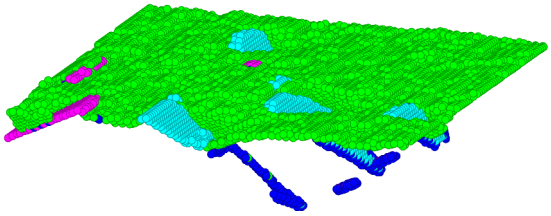

Figure 2.11: Atomistic plot of α/c interface for Si(110) regrowth.

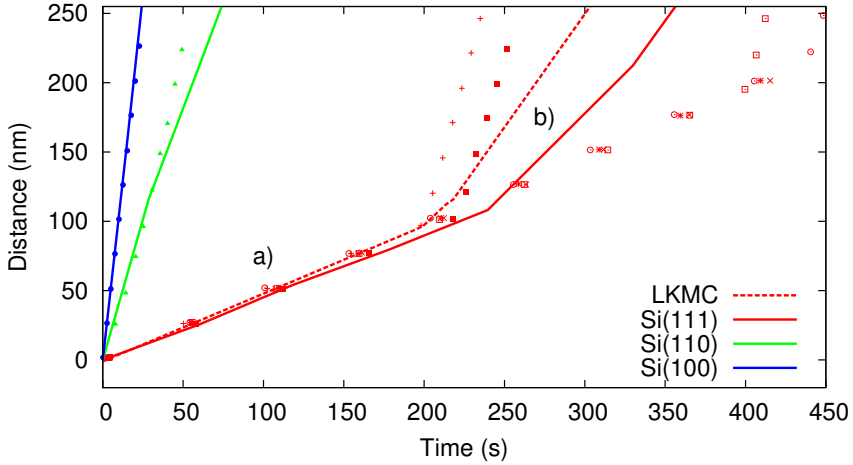

Figure 2.12: Experimental data from [Csepregi *et al.* 1976] (solid lines) versus simulated results (symbols) for Si(100), Si(110), and Si(111) regrown distance with time. Results with different random seeds, together with its average (dashed line), are shown for Si(111). The LKMC model can produce and explain the two different velocities (a) and (b) experimentally seen in Si(111) SPER. This figure is retaken from [Martin-Bragado & Sklenard 2012].

Ho *et al.* [Ho *et al.* 1984]. The dashed line shows the averaged values for several Si(111) simulations performed with different starting random seeds, which results are also shown as red symbols. The perfect agreement for Si(100), Si(110), and the first nanometers of Si(111) shows that the calibration done for a 20 nm amorphous thickness is enough to simulate much thicker samples. For Si(111) growth above 100 nm, the referred experimental work shows a sudden change into a faster recrystallization speed. This is also seen in our simulations. The partial disagreement between experimental data and simulations for this fast recrystallization speed for Si(111) is a product of our relatively small simulation domain ($250 \times 35 \times 35$ nm^3), as we will explain later. Such relatively small domain is needed to keep a reasonable use of computer resources.

Fig. 2.13 clarifies the origin of the two velocities during Si(111) recrystallization. The first phase (a) is produced by the very slow local Si(111) recrystallization events. During this phase, both regular (blue) and twin (green) nano–islands grow epitaxially on {111} substrates. The existence of these two crystallographic orientations leaves a stacking fault, parallel to the interface, at the intersection of both islands. These stacking faults are a source for other {111} facets to grow laterally and to form twins that will have a different orientation than the previous ones. These new twins facilitate in (b) the growth of a "grain". Such grain has the substrate crystalline configuration preferentially at one side of the new facet, in agreement with the observations of [Drosd & Washburn 1982]: "the {111} crystalline surface should attain an enhanced growth rate primarily on one side of the twin." The layout of the grain seen in Fig. 2.13c, with one side being sharp while the other is growing fast and integrating smoothly with the substrate is also in good agreement with previously reported observations: "Experi-

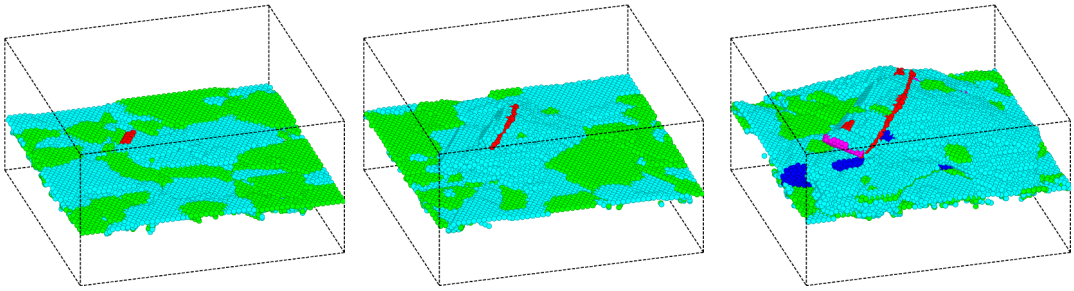

(a) t_0 (b) t_0 + 91 s (c) t_0 + 191 s

Figure 2.13: Atomistic plot of α/c interface evolution at 550 °C showing the transition between low and high Si(111) SPER velocities. Blue atoms belong to the substrate orientation, while green and red are twins. The formation of inclined twin (red atoms) produces the fast granular growth seen in experiments [Martin-Bragado & Sklenard 2012].

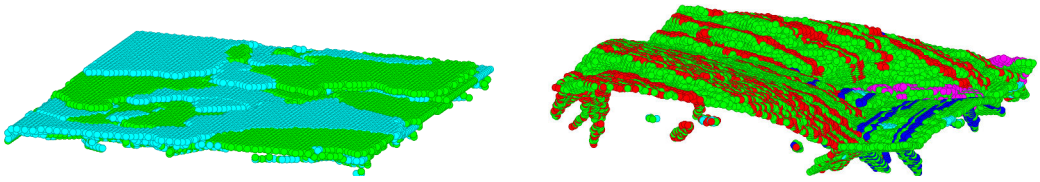

(a) Si(111) thin (b) Si(111) thick

Figure 2.14: Atomistic plot of α/c interface for thin and thick Si(111) regrowth, from [Martin-Bragado & Sklenard 2012].

mentally, the micro-twins are observed to thicken from one side." [Drosd & Washburn 1982]. Fig. 2.13 shows the formation and evolution of such twins. Fig. 2.13a shows the α/c interface when it is still mostly flat and mainly composed of regular (blue) and parallel twin (green) configurations. Nevertheless, an inclined twin has started (red). This new twin grows in Fig. 2.13b helped by the regular crystal. On Fig. 2.13c, secondary twins are also starting to grow. Since this process is random in nature, it explains the difficulty of small simulations to reproduce the average thickness at which it becomes important enough to change Si(111) macroscopic recrystallization speed. Also, the predicted simulation speed is expected to be higher: in a small simulation the growth of this extra facet rapidly takes over the whole simulation domain, while in a macroscopic experiment it would have to compete with many other slow–growing areas and also different twin orientations. Figs. 2.13 and 2.14 explain the experimental observed variations in surface roughness during Si(111) recrystallization: "in the first region the interface is uniform" while "in region B the growth rate is faster but the interface is very non-uniform" [Csepregi *et al.* 1976]. Our simulations, made at 550 °C, correlate both facts, faster speed and non-uniformity, and explain them in terms of the creation of twins that do not grow parallel to the {111} substrate orientation.

Finally, Fig. 2.15 shows the formation of defects in one of our Si(111) SPER simulations. For clarity only defective atoms (the ones without four bonds at the correct distances) are shown. Experimental work shows that "twins are substantially larger near the surface as compared to those near the substrate interface, but the twin density is larger near the interface" [Rechtin *et al.* 1978]. Our simulations agree: near the initial substrate interface there are many small twin nano-islands parallel to the substrate (green atoms), while near the surface (the α/c interface) there are fewer twins, but inclined and bigger in extension (red atoms). Our simulations also confirm that "a portion of the inclined {111} twin sets, finally determines the kinetics of crystallization" [Rechtin *et al.* 1978]. Since the presence of these new twins pro-

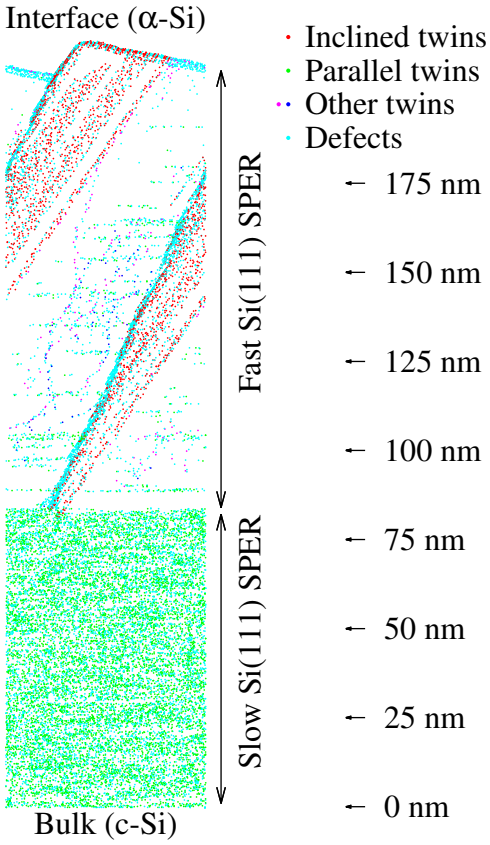

Figure 2.15: Formation of defects as shown in our Si(111) SPER simulations. Only the defective atoms, those without 4 bonds at the correct distances, are plotted. The simulation shows that the two phases of Si(111) produce two very different defect regimes: one with very dense, small, and parallel to the surface twin defects, and a second one with bigger but less dense inclined twin defects. This is in excellent agreement with experimental observations [Rechtin *et al.* 1978, Kyutt *et al.* 2001]. This figure is retaken from [Martin-Bragado & Sklenard 2012].

duces a fast microscopic {100} and {110} growth of grains we see the existence of less defects in this fast Si(111) growth than in the planar but slower Si(111) growth. Similar experimental results were observed during the SPER of samples amorphized with heavy erbium implantations [Kyutt *et al.* 2001], although we did not simulate any dopant induced effect: "numerous micro-twins formed on the (111) planes parallel and inclined to the surface are observed over the entire upper sublayer" [Kyutt *et al.* 2001]. Different topologies of defects were also observed: "width bands with a high twin density are predominantly located at the regrown layer and over the band of EOR defects" (approximately the first 200 nm and the last 450 nm in these experiments) "whereas regions with high relatively low twin densities are observed in the middle of the layer" [Kyutt *et al.* 2001] (from 200 nm to 450 nm). Our simulations did not show the third layer, but we could obtain the two first layers shown in Fig. 2.15.

2.4 Multidirectional SPER

The study of single–directional SPER has been discussed in detail in the previous section and will be used as a basis for the study of multidirectional SPER that will be now considered. It should be emphasized that during front–end processing, SPER systematically exhibits a multidirectional behavior and therefore turns out to be of great technological importance. Fur-

thermore, multidirectional SPER gives rise to various complications that do not happen during the regrowth of a planar–interface.

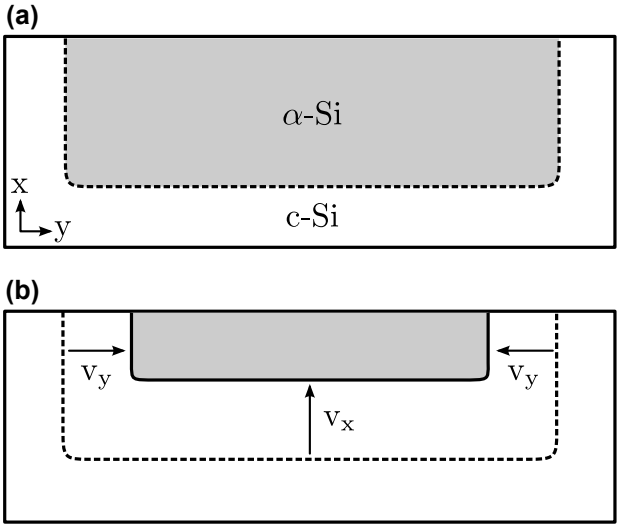

Figure 2.16: Schematic cross–section of the regrowth of a box–shaped amorphous region resulting from ion–implantation through a pattern mask: (a) after ion–implantation and (b) during recrystallization.

Multidirectional SPER occurs when the size of the amorphous region is finite along more than one direction, in contrast to single–directional SPER which assumes an amorphous layer of infinite lateral extent. Multidirectional SPER can be two–dimensional or three-dimensional depending if the amorphous region is limited along two or three directions respectively. Depending on the materials bounding the amorphous layer, the SPER will proceed differently. When the amorphous region is in contact with crystalline silicon, it will be able to act as a seed for epitaxial regrowth. This situation typically occurs during the process of electronic devices where amorphous regions are created by ion–implantation through a pattern mask and is schematically illustrated in Fig. 2.16a. In that case, the regrowth will proceed along both lateral and vertical directions with — most of the time — a distinct recrystallization velocity, as shown in Fig. 2.16b [Saenger *et al.* 2007b, Cerva & Küsters 1989]. On the other hand, when the bounding material is an insulator, typically SiO_2 or Si_3N_4 as it is often the case during the process of electronic devices, the regrowth is inhibited at the amorphous/insulator interface leading to the formation of macroscopic {111} planes [Burbure *et al.* 2007, Saenger *et al.* 2007a].

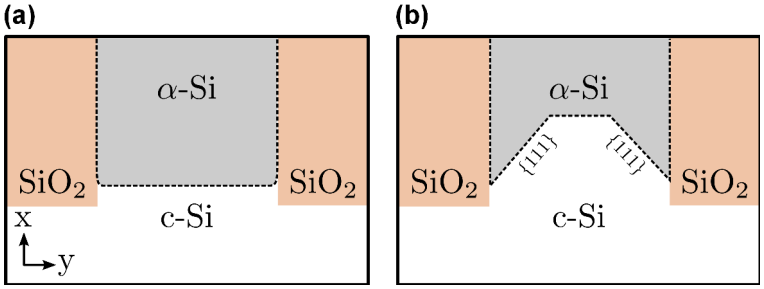

Figure 2.17: Schematic cross–section of the regrowth of a trench–bounded amorphous region: (a) after amorphization by ion–implantation and (b) after an incomplete recrystallization leading to the formation of {111} planes.

Generally speaking, multidirectional SPER results in the generation of defects which may impact the performances of electronic devices. In the following sections, LKMC simulation

results will be presented and compared with experimental data for the regrowth of amorphous regions bounded by insulator trenches (section 2.4.1) and of box–shaped amorphous regions (section 2.4.2). Finally, in section 2.4.3, the model will be used to simulate SPER in FDSOI devices at low processing temperature.

2.4.1 Influence of trenches

In a conventional CMOS process, transistors are isolated by SiO_2–filled trenches referred as Shallow Trench Isolations (STI). SPER of trench–bounded amorphous regions has been shown to give rise to imperfect recrystallization and subsequent defect formation. This problem has been addressed experimentally by Burbure *et al.* and Saenger *et al.* [Saenger *et al.* 2007a] on structures containing an amorphous layer produced by ion–implantation and bounded by SiO_2 trenches as shown schematically in Fig. 2.17a. They evidenced that SPER proceeds normally a the center of the layer but is inhibited at the amorphous/SiO_2 interface in the case of Si(100) and Si(110) substrates with the trench edge aligned respectively with the crystal's in–plane $\langle 110 \rangle$ and $\langle 100 \rangle$ directions. This anomalous regrowth behavior makes the recrystallization stop on $\{111\}$ planes, as shown in Fig. 2.17b. However, as has been discussed in section 2.3.4, the regrowth of $\{111\}$ planes is very slow and highly defective, leading to the formation of the so–called trench edge defects. Fig. 2.18 shows cross–sectional transmission

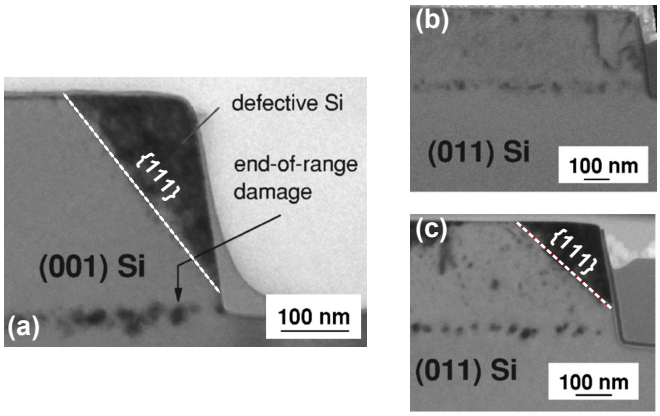

Figure 2.18: Cross–sectional transmission electron microscopy images from [Saenger *et al.* 2007a] of trench–bounded regions amorphized by ion–implantation recrystallized by annealing at 900°C for 60 s: (a) Si(100) substrate where insulator edges are aligned with the crystal's in–plane $\langle 110 \rangle$ direction. (b) Si(110) substrate where insulator edges are aligned with the crystal's in–plane $\langle 110 \rangle$ and (c) $\langle 100 \rangle$ direction.

electron microscopy images from [Saenger *et al.* 2007a] after the recrystallization of trench–bounded amorphous regions by annealing at 900°C for 60 s. Fig. 2.18a corresponds to Si(100) substrate with trench edges aligned with the crystal's in–plane $\langle 110 \rangle$ direction while Fig. 2.18c corresponds to Si(110) substrate with trench edges aligned with the crystal's in–plane $\langle 100 \rangle$ direction. In the two cases, the dark contrast indicates the presence of defective Si bounded by a $\{111\}$ plane intersecting the surface at angles of 35.3° and 54.7° for Si(100) and Si(110) respectively. Interestingly, Fig. 2.18b shows a rather different behavior for Si(110) substrate with trench edges aligned with the crystal's in–plane $\langle 110 \rangle$ direction leading to a non defective regrowth. It should also be emphasized that these defective regions appear to be very stable and are still observed even after a 1325 °C anneal for 5 h [Saenger *et al.* 2007a]. Saenger *et al.* interpreted their results using a heuristic model in order to explain the formation of $\{111\}$ planes.

In this section, we will present simulation results using the LKMC model presented in

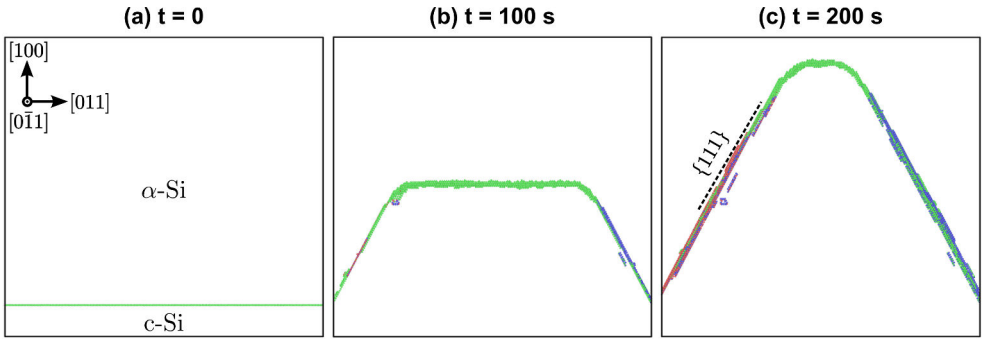

Figure 2.19: Several snapshots projected along [0$\bar{1}$1] direction taken during LKMC simulation of SPER at 550 °C of a ⟨110⟩–aligned amorphous layer on Si(100) crystalline substrate: (a) initial configuration, (b) after 100 s and (c) after 200 s.

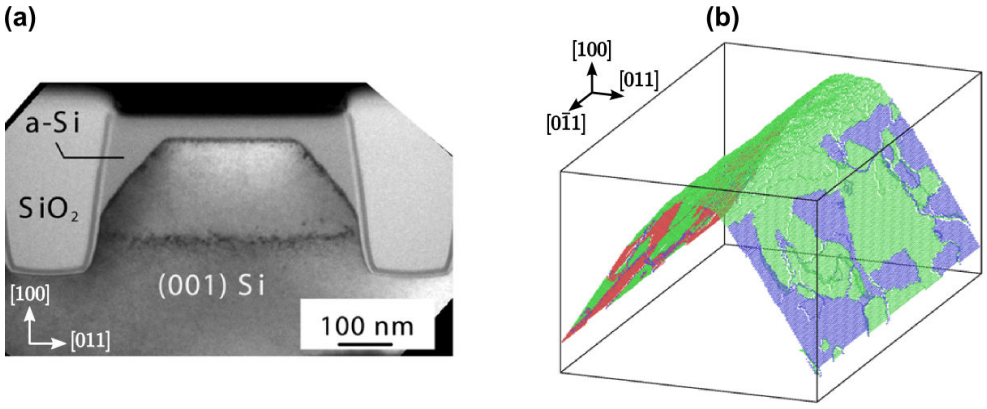

Figure 2.20: Partial regrowth of trench–bounded ⟨110⟩–aligned amorphous layer on Si(100) substrate: (a) Cross–sectional transmission electron microscopy image after a 30 min anneal at 550 °C taken from [Saenger *et al.* 2007a] and (b) LKMC simulation snapshot after annealing at 550 °C for 200 s.

section 2.2 to get insight into the microscopic mechanisms leading to the generation of these {111} facets at trench edges and subsequent defects. For sake of clarity, we will limit this review to Si(100) substrates with trench edges aligned with crystal's in–plane ⟨110⟩ and ⟨100⟩ directions corresponding to configurations which are of technological relevance. Nevertheless, the LKMC model is generic and could be used to examine other configurations.

SPER simulation of ⟨110⟩–aligned and ⟨100⟩–aligned amorphous layers on Si(100) have been carried out on $40 \times 60 \times 65\sqrt{2}a_0$ nm^3 and $40 \times 60 \times 92a_0$ nm^3 simulation cells respectively (see Fig. 2.19a and Fig. 2.21a). Periodic boundary conditions have been used along z direction only. The absence of periodic boundary conditions along y allow to indicate the presence of the trenches. For each orientation, a 35 nm α–Si layer has been regrown at 550 °C.

Fig. 2.19 shows several snapshots taken during LKMC simulation of ⟨110⟩–aligned structure. As has been described previously, the regrowth proceeds normally along ⟨100⟩ direction in the center, but is completely stopped at the lateral boundaries corresponding to the insulator trenches (Fig. 2.19b). The α/c interface pinning at trench edges rapidly leads to the formation of {111} planes evidenced by the dotted line in Fig. 2.19c, in good agreement with the XTEM image of Fig. 2.20a. The atomistic view in Fig. 2.20b corresponds to a snapshot of the LKMC simulation after 200 s anneal and show that {111} planes regrow by forming of regular (green) and twin (blue and red) nano–islands, leaving lines of defects resulting in the generation of stacking faults. These observations are similar to those made during the

analysis of single–directional Si(111) SPER (see section 2.3.4). However, in this case, the regrowth appears to be multidirectional and involves {111} and {100} competing fronts. The higher regrowth velocity of {100} configurations with respect to {111} configurations results in a trapezoid shape of the regrowth front. When the top of the interface reaches the surface, two amorphous triangular regions bounded by the insulator trench and {111} plane are still present. Thus, the recrystallization of these regions can only occur trough the slow and highly defective (111)–oriented SPER leading to the defective regions observed in Fig. 2.18a.

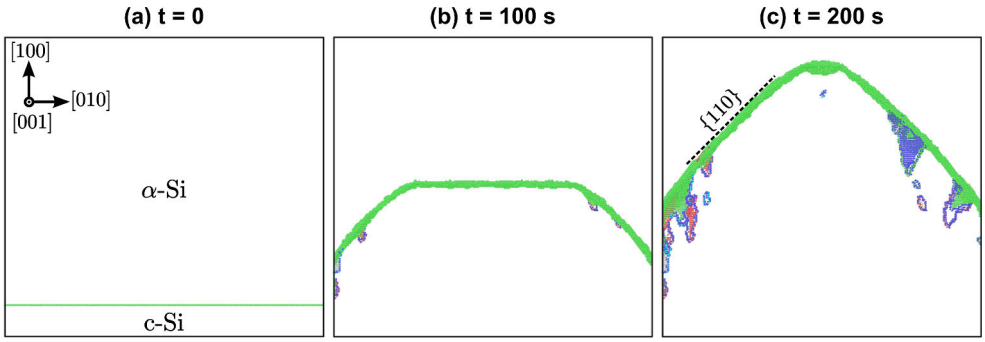

Figure 2.21: Several snapshots projected along [001] direction taken during LKMC simulation of SPER at 550 °C of a ⟨100⟩–aligned amorphous layer on Si(100) crystalline substrate: (a) initial configuration, (b) after 100 s and (c) after 200 s.

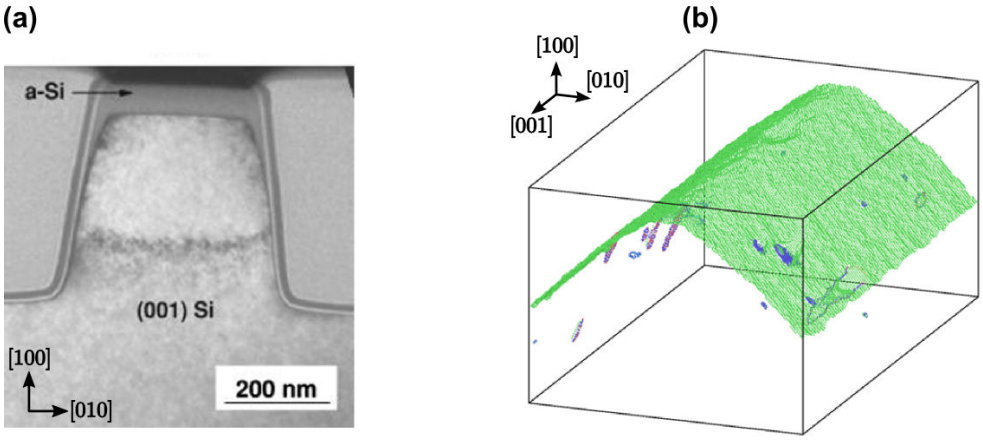

Figure 2.22: Partial regrowth of trench–bounded ⟨100⟩–aligned amorphous layer on Si(100) substrate: (a) Cross–sectional transmission electron microscopy image after a 30 min anneal at 550 °C taken from [Saenger *et al.* 2007a] and (b) LKMC simulation snapshot after annealing at 550 °C for 200 s.

A rather different behavior occurs when trench edges are aligned with the crystal's in–plane ⟨100⟩ direction as shown in Fig. 2.22. SPER appears to proceed normally along ⟨100⟩ direction in the center as for ⟨110⟩–aligned structure. However, from Fig. 2.21b recrystallization is slower at edge boundaries than in the center but not stopped resulting in the formation of a rounded trapezoid shape. The lateral sides of the trapezoid region form a 45° angle with the surface which corresponds to {110} planes (see dashed line in Fig. 2.21c). This is again in good qualitative agreement with XTEM observation of Saenger *et al.* shown in Fig. 2.22a. It should be emphasized that the apparent presence of a defective regrowth in Fig. 2.21c is actually an artifact resulting from the projection as confirmed by the three–dimensional view of the same snapshot shown in Fig. 2.22b. A comparison between the lateral facets formed during SPER of ⟨110⟩–aligned (Fig. 2.20b) and ⟨100⟩–aligned (Fig. 2.22b) structures suggest

that there is no defective regrowth in the later case. It therefore turns out that SPER of ⟨100⟩–aligned α–layer succeeds without the formation of defective Si, similarly to the observations of Fig. 2.18b for a ⟨110⟩–aligned Si(011) structure.

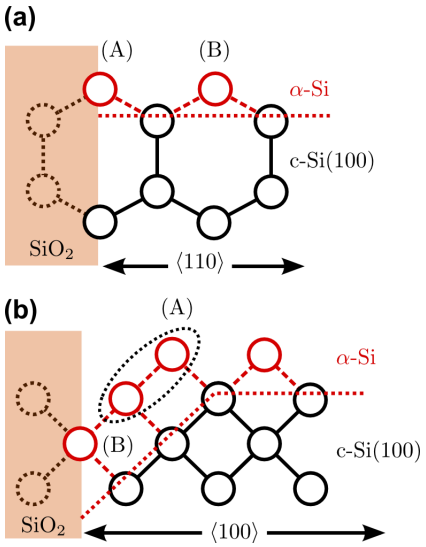

Figure 2.23: Schematics of the microscopic regrowth mechanisms involved during recrystallization of Si(100) with (a) SiO_2 edges aligned with the crystal's in–plane ⟨110⟩ direction and (b) SiO_2 edges aligned with the crystal's in–plane ⟨100⟩ direction.

The LKMC model allows to correctly catch the macroscopic observations of SPER of trench–bounded amorphous regions. However, going deeper to the microscopic detail, it also provides a physical explanation of why ⟨110⟩–aligned and ⟨100⟩–aligned structures lead to {111} and {110} faceting respectively. This is indeed clarified in Fig. 2.23, for ⟨110⟩–aligned (a) and ⟨100⟩–aligned (b) configurations. The dotted atoms and bonds in SiO_2 trenches correspond to missing template for regrowth. Indeed, from the initial assumption of the model, the regrowth of the microscopic configuration needs to form two undistorted bonds to the crystalline phase [Drosd & Washburn 1982] (see section 2.2). From Fig. 2.23a, it follows that atom (B) can be incorporated to the crystalline lattice by forming two undistorted bonds with its two *crystalline* first neighbors. In contrast, atom (A) has only one *crystalline* first neighbor which prevents a recrystallization event to occur and causes the pinning of the α/c interface at the trench edge. In a ⟨100⟩–aligned Si(100) structure the situation is quite different as shown in Fig. 2.23b. Far from the interface, the recrystallization can proceed normally while, close to the interface, it requires an indirect mechanism. Indeed, to recrystallize, atom (B) needs that the {110} configuration labeled (A) performs a recrystallization event first. Since $\nu_{\langle 100\rangle} > \nu_{\langle 110\rangle}$, the regrowth in the center is faster than close to the insulator edge resulting in the development of {110} facets.

Finally, the model can be used to simulate the SPER of trench–bounded active regions where the amorphous layer is three–dimensional instead of being two–dimensional without implying additional complexity. The simulations have been carried out without periodic boundary conditions using $25 \times 110 \times 50$ nm^3 simulation cell containing a 20 nm α–layer. As previously, ⟨110⟩–aligned and ⟨100⟩ rectilinear Si(001) features have been studied. Since the purpose was to investigate the final stage of SPER by focusing on trench edge defects, anneals have been carried out at 900°C during 10 s in order to achieve a complete regrowth. Fig. 2.24 shows plan–view scanning electron microscopy images from [Saenger *et al.* 2007a] for ⟨110⟩–aligned (a) and ⟨100⟩ (b) structures amorphized by ion–implantation after a 900 °C

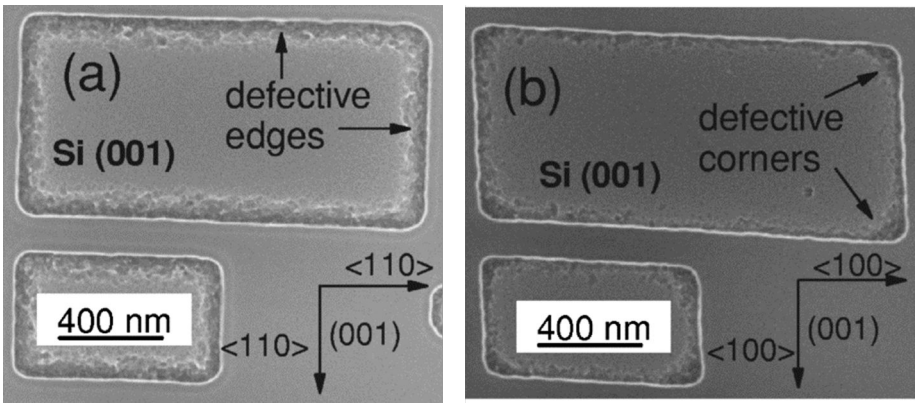

Figure 2.24: Plan–view scanning electron microscopy (SEM) images from [Saenger *et al.* 2007a] of trench–edge defects in (a) ⟨110⟩–aligned and (b) ⟨100⟩–aligned trench–bounded rectilinear Si(001) structures amorphized by ion–implantation after a 900 °C anneal for 6 min. Secco etching were carried out prior to SEM observations in order to allow the visualization of defects [Secco d'Aragona 1972].

anneal for 6 min. The corresponding simulation results are shown in Fig. 2.25. Not surprisingly, the regrowth of ⟨110⟩–aligned trench–bounded features produces highly defective edges (see Fig. 2.24a and 2.25a). In contrast, SPER ⟨100⟩–aligned trench–bounded features do not produce trench–edge defects but only slightly defective corners (see Fig. 2.24b and 2.25b). Interestingly the defects in ⟨100⟩–aligned trench structure disappear with further annealing in contrast to those in ⟨110⟩–aligned trench structure (see [Saenger *et al.* 2007a] for a more detailed description). However the model does not assume any evolution of these defects for the moment and thus cannot predict this behavior. For intermediate annealing temperatures as those used in a low thermal budget process, the model provides a result in good agreement with experimental observations and is therefore technologically relevant. In particular, the presence of α–Si/insulator interfaces is a concern for the SPER of FDSOI or thin–body MOSFETs as we will see at the end of this chapter (see section 2.4.3).

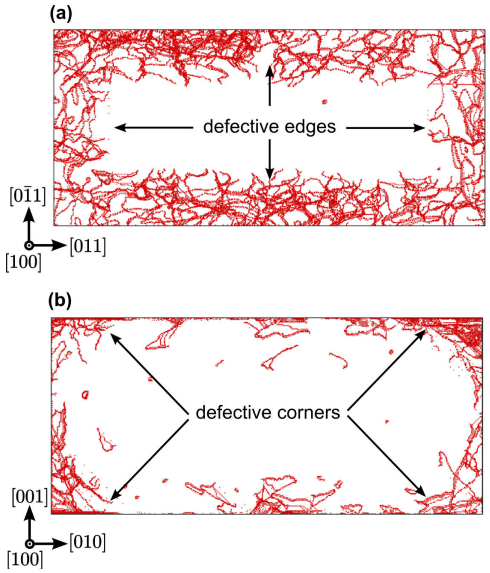

Figure 2.25: Top view of simulated defect distributions after a 900 °C anneal for 10 s: (a) ⟨110⟩–aligned and (b) ⟨100⟩–aligned trench–bounded rectilinear Si(001) structures.

2.4.2 Regrowth of box–shaped amorphous regions

Box–shaped amorphized regions are generally the result of patterned ion–implantation as shown schematically in 2.16a. In this situation, SPER will proceed through competing fronts which will advance along both lateral and vertical directions and is by definition multidirectional as illustrated in Fig. 2.16b. However, based on the results of previous section, it is clear that the simple picture given by Fig. 2.16b is not correct and the real behavior appears to be much more complex. Actually the situation is close to the case of SPER of trench–bounded amorphous regions except that the insulator becomes crystalline silicon.

The regrowth of box–shaped amorphized regions has been studied experimentally by Cerva and Küster [Cerva & Küsters 1989] and Saenger *et al.* [Saenger *et al.* 2007b]. Based on their results, Saenger *et al.* proposed an heuristic model (see [Saenger *et al.* 2007b] for a more detailed description). More recently, a continuum approach based on level–set methods has been used by Morarka *et al.* [Morarka *et al.* 2008, Morarka *et al.* 2009]. In this section, the LKMC model will be used to study the regrowth of patterned regions. Again, the study will be limited to $\langle 110 \rangle$–aligned and $\langle 100 \rangle$–aligned amorphous lines in Si(100).

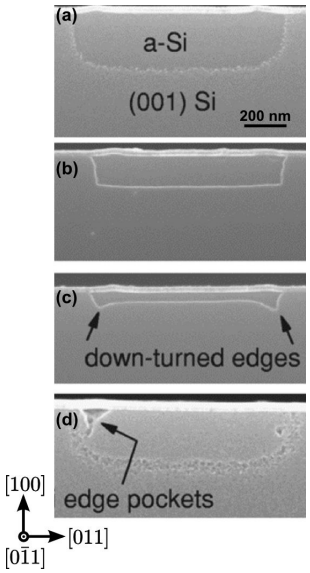

Figure 2.26: Cross–sectional scanning electron microscopy (SEM) images of SPER at 550 °C of box–shaped two–dimensional amorphous regions in Si(001) with edges aligned with $\langle 110 \rangle$ direction from [Saenger *et al.* 2007b]: (a) after ion–implantation, (b) after 6 min, (c) after 12 min and (d) after 18 min. Secco etching were carried out prior to SEM observation in order to allow the visualizations of defects [Secco d'Aragona 1972].

Fig. 2.26 shows several cross-sectional scanning electron microscopy images at different stages of SPER at 550 °C from [Saenger *et al.* 2007b]. The mask used to produce the two–dimensional $\langle 110 \rangle$–aligned box–shaped amorphous region exposed $\approx$ 970 nm of Si(100) and the amorphization depth was $\approx$ 270 nm as shown in Fig. 2.26a (see [Saenger *et al.* 2007b] for experimental details). For computational reasons, the size of the amorphous region was too big to be simulated with the LKMC model. As a consequence, the simulation sizes have been reduced but the aspect ratio has been preserved. The regrowth of $\langle 110 \rangle$–aligned and $\langle 100 \rangle$–aligned box–shaped α–layers have been simulated using a $146 \times 43 \times 66 a_0$ nm^3 and $146 \times 43 \times 40\sqrt{2} a_0$ nm^3 simulation cell respectively and periodic boundary conditions have been applied along z direction. In each simulation, a 142×41 nm^2 box–shaped α–Si region was considered as shown in Fig.2.27a (the extra non amorphous material at left, right and bottom of the simulation cell is crystalline Si and acts as a recrystallization template). Subsequent

annealing has been simulated at 550 °C.

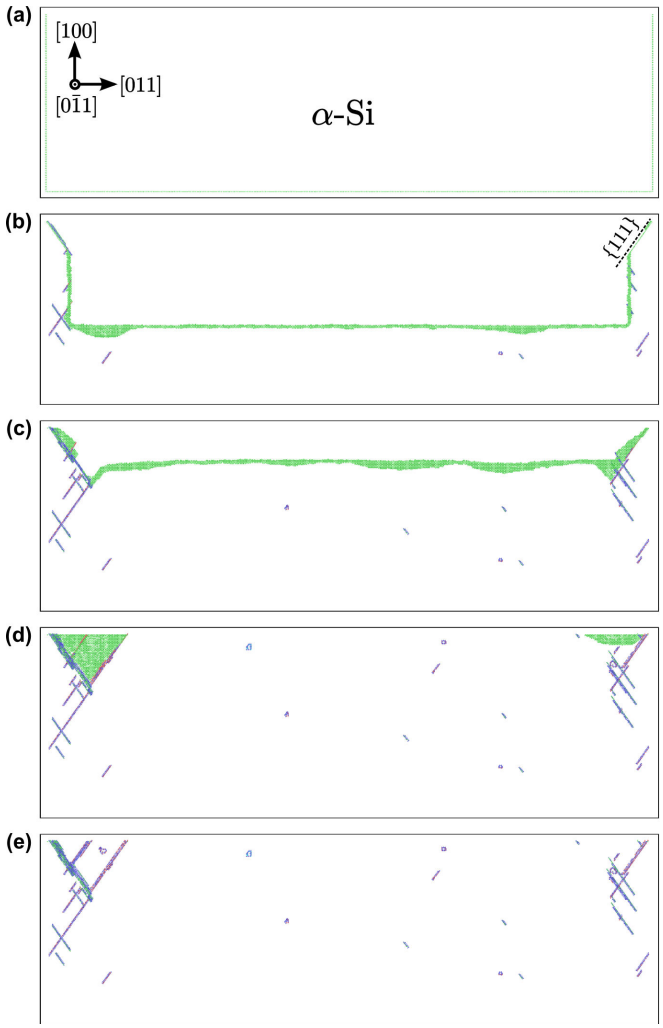

Figure 2.27: Simulation snapshots of recrystallization of ⟨110⟩–aligned box–shaped amorphized regions in Si(001) at different stages of the anneal at 550 °C: (a) initial structure, (b) after 100 s, (c) after 200 s, (d) after 297 s and (e) after 480 s (complete regrowth has been achieved).

Fig. 2.27 presents several simulation snapshots at different stages of the anneal of the ⟨110⟩–aligned box–shaped structure. Fig. 2.27b shows that SPER produces a characteristic {111} faceting of the lateral fronts because of the surface proximity as for the regrowth of trench–bounded regions (see previous section). Otherwise, the regrowth proceeds normally along ⟨110⟩ direction laterally and ⟨100⟩ direction vertically. This situation appears in good agreement with XSEM observations shown in Fig. 2.26b. An interesting phenomenon occurs when the vertical regrowth front reaches the {111} planes developing at the lateral regrowth fronts because of surface pinning. This leads to the formation of down–turned edges (Fig. 2.26c) that are correctly predicted by the LKMC model (Fig. 2.27b). These down–turned edges evolve into small triangular edge pockets bounded by {111} as evidenced by simulations in Fig. 2.26d and XSEM image in Fig. 2.26d. The dissymmetry between edge pockets in the simulation results from the stochastic behavior of the KMC method. However, the fact to obtaining a similar dissymmetry as in Fig. 2.26d is purely fortuitous. Finally, Fig. 2.27e shows the defect distribution at the end of the regrowth.

Another interesting aspect of box–shaped regrowth that is not captured by the LKMC

model is the slower regrowth at the corner of the box–shaped amorphous region. This is not shown in Fig. 2.26 but it has been observed by several researchers [Rudawski *et al.* 2009, and references therein]. This behavior results in a pinch-off of lateral and vertical regrowth fronts which produces mask–edge defects when the two fronts meet. Rudawski *et al.* have reported that mask–edge defects are composed of either shear–type or 60°–type perfect dislocations with Burger vectors $a_0/2\langle 110\rangle$ based on g_{220} bright–field PTEM analysis [Rudawski *et al.* 2009]. More recently, Shen *et al.* has determined these defects to be Frank partial loops with Burger vectors $a_0/3\langle 111\rangle$ from Molecular Dynamics simulations and from TEM and Inverse–Fast–Fourier–Transform (IFFT) analysis of (111) plane lattice images [Shen *et al.* 2012]. It should be emphasized that the generation of these defects can be controlled by applying an external stress [Jones *et al.* 1988, Rudawski *et al.* 2006]. This process has given rise to a new kind of Stress Memorization Techniques (SMT) based on the control of the formation of dislocations during SPER process in order to induce stress in channel MOSFETs. In particular, this technique has been reported by Intel [Weber *et al.* 2011], Samsung [Lim *et al.* 2010] and TSMC [Shen *et al.* 2012] in high-κ/Metal–Gate processes of bulk MOSFETs.

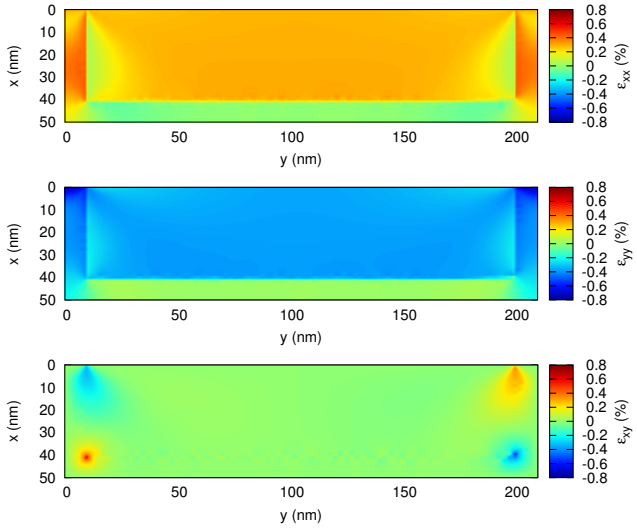

Figure 2.28: Strain simulations generated by volume expansion of α-Si in a box–shaped amorphized structure.

In summary, it turns out that the regrowth of $\langle 110\rangle$–aligned box–shaped structures produces (i) microtwinning from the development of $\{111\}$ planes and (ii) dislocations when lateral and vertical fronts pinch–off. The origin of this second mechanism remains quite unclear when no stress is applied and is not predicted by the actual LKMC model. It can be suspected that the density variation between amorphous and crystalline phases may give rise to strain causing the atoms located in the lateral front to be slightly displaced with respect to those in the vertical front which could lead to the nucleation of a dislocation when the two ledges meet. Fig. 2.28 presents plots of the strain generated by the volume expansion of the amorphous phase taken to be 2 % as suggested in [Custer *et al.* 1994] and calculated using the Sentaurus SProcess simulator. By convention a negative (positive) value represents a compressive (tensile) strain. In particular, introducing a correction of the activation energy by taking into account a contribution of shear strain ε_{xy} (plotted in Fig. 2.28c) has been shown to lead correctly to the retardation of the regrowth velocity at corners [Martin-Bragado & Moroz 2009]. However, it should be emphasized that this approach lacks of physical basis and requires a mechanical calculation which has to be updated as the SPER goes along. The simulation of mask–edge dislocations are beyond the scope of this manuscript even if they present a great

technological interest.

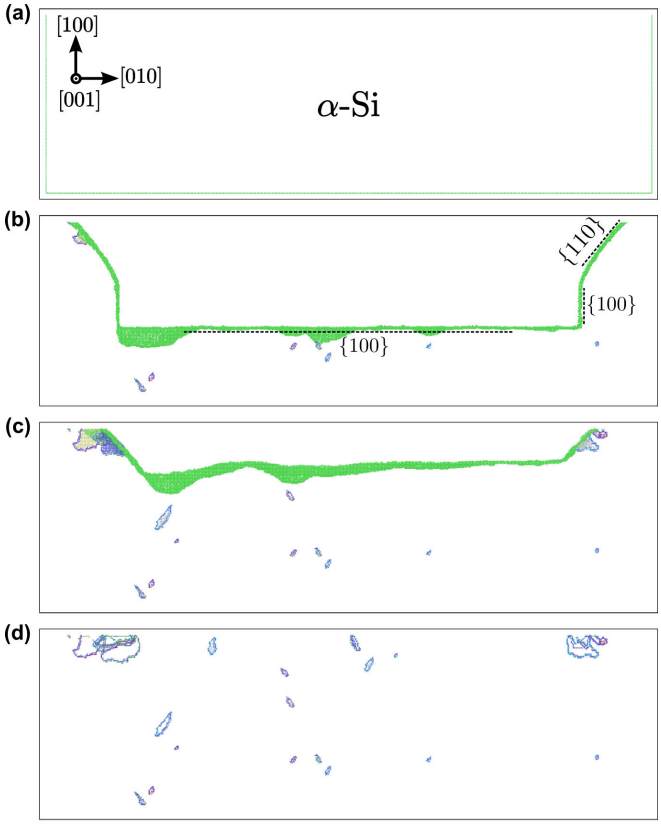

Figure 2.29: Simulation snapshots of recrystallization of ⟨100⟩–aligned box–shaped amorphized regions in Si(001) at different stages of the anneal at 550 °C: (a) initial structure, (b) after 100 s, (c) after 200 s, and (d) after 480 s (complete regrowth has been achieved).

Fig. 2.29 shows several simulation snapshots at different stages of the anneal of the ⟨100⟩–aligned box–shaped structure. Based on the results obtained for the regrowth of trench bounded ⟨100⟩–aligned structures, a less defective regrowth is expected than for ⟨110⟩–aligned box–shaped amorphous regions because lateral fronts produce {110} facets rather than {111} facets during SPER. This is indeed the case as shown in Fig. 2.29b. On the other hand, there is no formation of edge pockets (in contrast to ⟨110⟩–aligned structures) leading to less defects (see Fig. 2.29c). Finally, from Fig. 2.29d, SPER appears to generate very few defects. Nevertheless, there is to our knowledge no experimental study of the regrowth of ⟨100⟩–aligned box–shaped structures. In particular, it is not clear whether a slowing down of the regrowth velocity corners occurs and if subsequent mask–edge dislocation nucleation happens.

2.4.3 SPER in FDSOI MOSFETs

The LKMC model has been shown to correctly describe the evolution of the regrowth fronts during multidirectional SPER including the formation of facets and subsequent defects generation. In particular, in either trench–bounded or box–shaped structures, ⟨110⟩–aligned structure appears to be quite defective because of the formation of {111} facets. In contrast, in ⟨100⟩–aligned structure the regrowth produces {110} facets resulting in a low defect nucleation probability.

In this section, LKMC simulations are performed in order to analyze SPER in FDSOI devices. In contrast to bulk MOSFETs, FDSOI process requires a selective epitaxial growth on

the semiconductor thin film to form the raised source/drain (RSD) junctions prior to implant steps. Amorphous regions are typically produced by ion–implantation where the gate stack and Si_3N_4 spacers are used as a mask and are laterally bounded by a Si_3N_4 spacer and a SiO_2 trench. As in previous sections, SPER of both $\langle 110 \rangle$–aligned and $\langle 100 \rangle$–aligned structures in Si(100) has been simulated with periodic boundary conditions along z direction. The simulation cell sizes were respectively $24 \times 170 \times 40\sqrt{2}a_0$ nm^3 and $24 \times 170 \times 66a_0$ nm^3 and the simulated structure is shown in Fig. 2.30. It should be noted that 70×18 nm^2 amorphous regions separated by a 30 nm long gate have been considered for source and drain junctions formation. The simulation cell boundary is highlighted by the solid black line in Fig. 2.30. The amorphous regions have been recrystallized by annealing the structure[5] at 550 °C and simulation results are presented in subsequent sections.

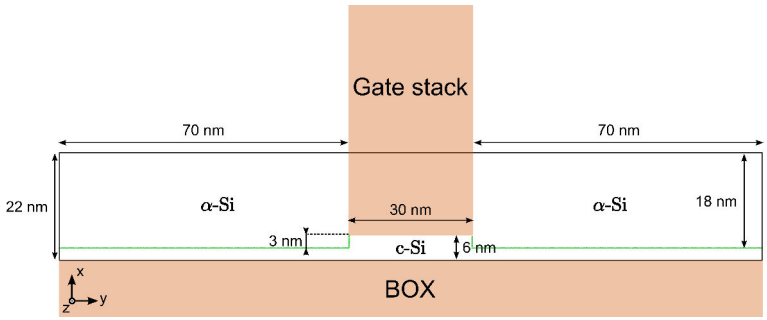

Figure 2.30: Simulated FDSOI structure.

2.4.3.1 SPER of $\langle 110 \rangle$–aligned α–Si(100)

Fig. 2.31 shows simulation results of $\langle 110 \rangle$–aligned amorphous regions at different stages of the anneal at 550 °C. From Fig. 2.31a, after 10 s the lateral regrowth front bounded by crystalline Si (*i.e.* on the gate side) has advanced but pinning occurs at the gate edge resulting in the beginning of $\{111\}$ facets formation. On the hand, the vertical front advances along $\langle 100 \rangle$ direction but is also pinned at trench edge leading to $\{111\}$ faceting. In Fig. 2.31b it appears that after 100 s the lateral front has disappeared and the regrowth proceeds through the vertical α/c front. However, $\{111\}$ planes are formed because of the presence of non–crystalline silicon material, similarly to the situation observed during the recrystallization of trench–bounded amorphous regions (see 2.4.1). Fig. 2.31c shows that the bulk regrowth has finished but α–Si regions bounded by $\{111\}$ planes remain at edges. The regrowth of these regions proceeds through (111) recrystallization and is therefore very slow and highly defective as shown in Fig. 2.31d. Thus, SPER of $\langle 110 \rangle$–aligned amorphous regions in Si(100) FDSOI MOSFETs appears as producing defective regions close to gate and trench edges. The consequence on the electrical performances of the devices is still unclear[6]. They should typically result in an increase of the resistance of source and drain regions because of scattering phenomena in disordered materials [Ashcroft & Mermin 1976]. Notice also that the same kind of defective zones will appear at edges in the width direction (not shown here but similar to the results of Fig. 2.25a) and could be problematic for devices with a small width.

N-channel FDSOI MOSFETs with ultrathin silicon channel (7 nm) and 145 nm Buried

[5] It should be emphasized that in actual process a 600 °C anneal during 2 min is generally used.

[6] Near–gate defective regions have been involved to explain the drop in carrier mobility measured in shorter devices as well as the unusual low–temperature behaviour of mobility and scattering mechanisms [Pham-Nguyen *et al.* 2009]

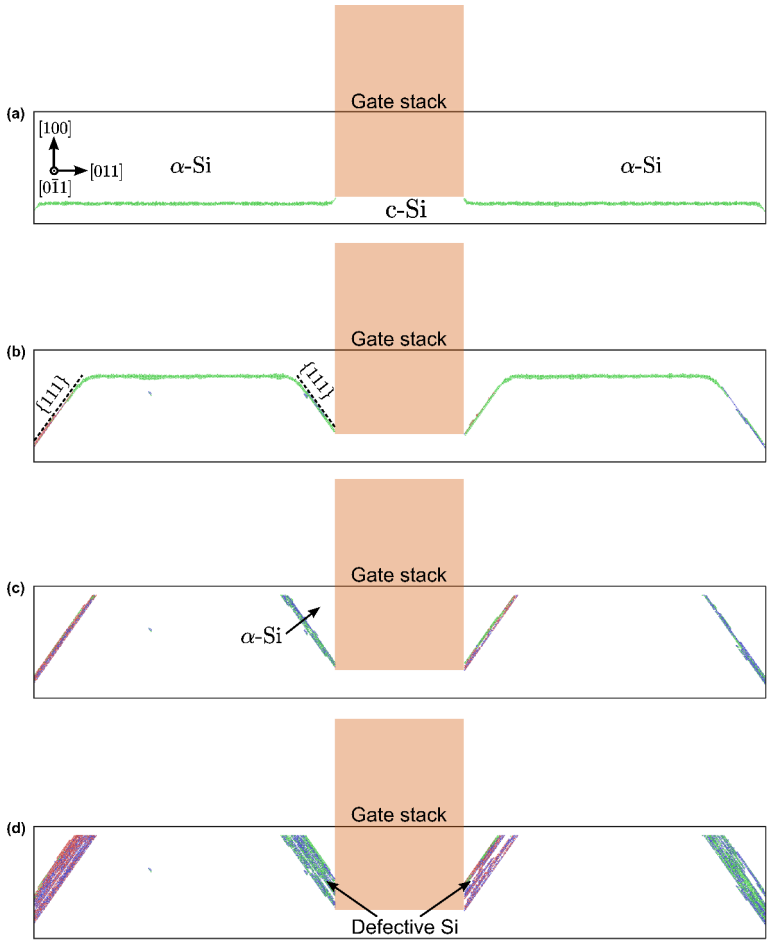

Figure 2.31: Simulation snapshots of recrystallization of ⟨110⟩–aligned amorphized regions in an FDSOI MOSFET at different stages of the anneal at 550 °C: (a) after 10 s, (b) after 100 s, (c) after 200 s, and (d) after 600 s.

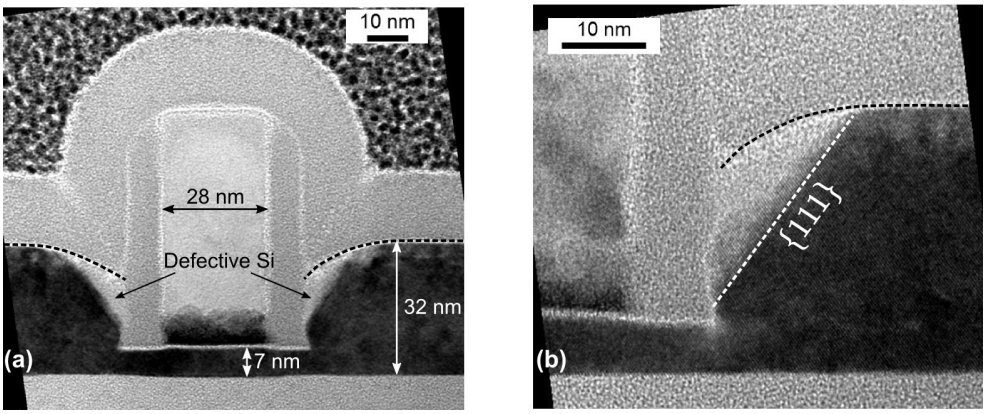

Figure 2.32: Cross-sectional transmission electron microscopy images of trench–edge defects in Si(100) FDSOI devices after annealing at 600 °C for 4 min.

Oxide (BOX) have been fabricated at CEA–Leti on 300 mm Si(100) wafers following a standard low–thermal budget process flow. After the HfSiON/TiN/Poly-Si gate patterning and spacer fabrication, a selective Si epitaxy has been used to form Raised Source Drain (RSD). Amorphous regions were formed by ion–implantation of As^+ using 9 keV ions implanted at a dose of 1×10^{15} /cm^2 and regrown through SPER by annealing at 600 °C for 4 min. Fig. 2.32a shows a cross-sectional transmission electron microscopy image of a device at the end of the

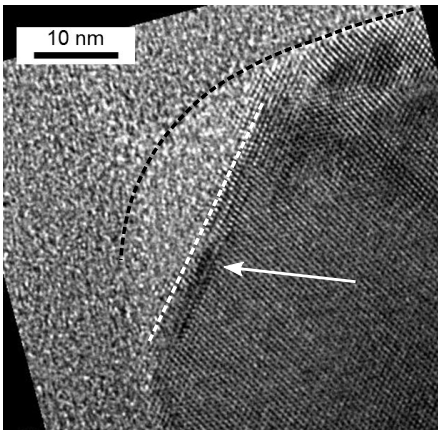

Figure 2.33: Zoom of the cross-sectional XTEM image showing the trench–edge defect in Fig. 2.32b. The contrast variation indicated by arrow suggests the presence of microtwins on {111} planes.

anneal. Fig. 2.32b confirms the presence of the characteristic trench-edge defects bounded by {111} planes along gate edges as predicted by LKMC simulations (see Fig. 2.31d). In particular, the contrast variation indicated by arrow in Fig. 2.33 suggests that microtwins have been formed during the partial recrystallization of {111} planes.

2.4.3.2 SPER of ⟨100⟩–aligned α–Si(100)

In contrast to ⟨110⟩–aligned structures, we might expect a better regrowth quality with ⟨100⟩–aligned amorphous regions as it has been shown in sections 2.4.1 and 2.4.2. Fig. 2.34 presents simulations snapshots at different stages of the anneal and it can be indeed observed that {110} faceting occurs rather than {111} faceting resulting in a much less defective SPER. In particular, after 200 s SPER has almost finished (see Fig. 2.34b) while it was not the case for ⟨110⟩–aligned structures (see Fig. 2.31c). These results suggest therefore that ⟨100⟩–aligned layouts could be preferable than ⟨110⟩–aligned ones for devices processed at low thermal budget if defective regions turn out to be a real concern for the electrical performances of FDSOI devices.

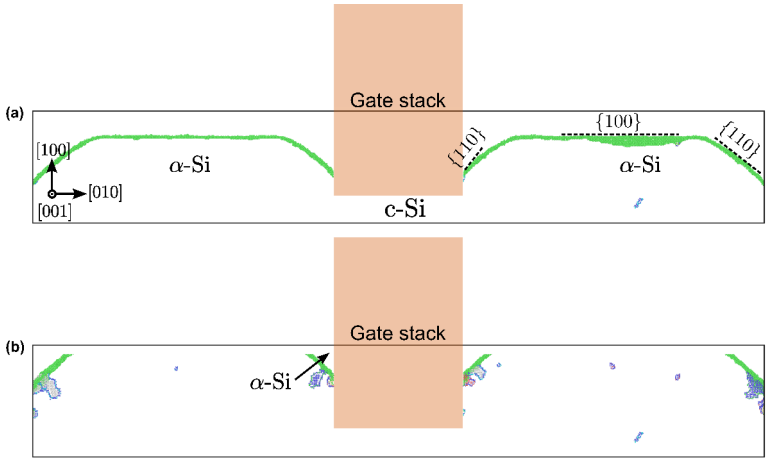

Figure 2.34: Simulation snapshots of recrystallization of ⟨100⟩–aligned amorphized regions in an FDSOI MOSFET at different stages of the anneal at 550 °C: (a) after 100 s and (b) after 200 s.

We should point out that in the case of the 28 nm FDSOI technology developed at STMicroelectronics, 45° rotated SOI substrates are used, so that the channel orientation is along

$\langle 100 \rangle$ direction. This technological option may be particularly suitable for junction formation with low processing temperatures.

2.5 Summary

In this chapter, we have presented a review of the thermodynamics and kinetics of SPER. It appears that SPER is mainly driven by kinetics and occurs at the amorphous/crystalline interface because of the strong orientation dependent regrowth velocity observed experimentally. In particular, the regrowth velocity is well described by an Arrhenius behavior with temperature:

$$v(\theta, T) = K(\theta) \exp\left(-\frac{E_a}{k_B T}\right), \tag{2.17}$$

where E_a is the activation energy (2.7 eV for Si) and K(θ) is an orientation dependent prefactor, with θ being the angle ranging from $\langle 100 \rangle$ to $\langle 110 \rangle$.

From these considerations, an atomistic comprehensive model has been introduced relying on the kinetic Monte Carlo (KMC) method. This model considers an explicit representation of the atomic structure at the amorphous/crystalline interface and assigns a tag to each atom depending if it is *amorphous* or *crystalline*. This model has been extended in the lattice KMC (LKMC) module of the MMonCa simulator during this PhD. It enables to simulate both regrowth anisotropy and twin defect formation. Anisotropy is included by distinguishing among $\{100\}$, $\{110\}$ and $\{111\}$ local configurations depending on atoms at the α/c interface forming two undistorted bonds or needing one or two extra atoms to form them as initially proposed by Drosd and Washburn [Drosd & Washburn 1982]. The recrystallization probability for each configuration follows $\nu = K_{configuration} \times \exp\left(-E_a/k_B T\right)$ with $K_{configuration}$ being a configuration–dependent prefactor and E_a the activation energy. Twin defect formation during the recrystallization of $\{111\}$ configurations has been included more recently (see [Martin-Bragado & Sklenard 2012]). It is achieved through an on–the–fly algorithm determining the correct twin configuration that can complete the sixfold ring, characteristic of crystalline structure in diamond cubic lattices.

The model has been used to simulate the SPER of a planar α/c interface with different orientations. Simulation results of the regrowth velocity as a function of crystalline orientation have been shown to be in excellent agreement with experimental data from the literature. In the case of the SPER of Si(111), simulations capture the two velocity regimes that have been observed experimentally in [Csepregi *et al.* 1976, Csepregi *et al.* 1978]. We explained this behavior by analyzing the origin for the formation and subsequent evolution of different type of twins (parallel to the interface and inclined). In particular, we observed that during the initial regime, Si(111) SPER proceeds through $\{111\}$ microscopic mechanisms and is therefore very slow and highly defective (because twins are formed). The second regime is produced by the small, but not null, probability that such defects can serve as a seed to grow inclined twins that are compatible with the structure serving as the edge of a growing "grain" of regular crystalline silicon using a mechanism different than $\{111\}$ local microscopic recrystallization. This second regime is (i) faster because it involves $\{100\}$ and $\{110\}$ microscopic configurations that have a higher recrystallization rate than $\{111\}$ ones, (ii) rough, because the growing grains do not follow the orientation of the Si(111) substrate, and (iii) less defective but with larger twins at the edges that provide the support for the grain.

On a more technologically relevant aspect, multi–directional SPER has been studied with the LKMC model considering:

1. trench–bounded amorphous regions (corresponding to structures that are laterally bounded by a different material than silicon)

2. box–shaped amorphous regions (corresponding to structures that are bounded by laterally bounded by crystalline silicon).

In the case of the SPER of trench–bounded amorphous regions, faceting occurs at edges because of the missing crystalline template to allow a normal regrowth. We simulated the regrowth of $\langle 110 \rangle$–aligned structures and $\langle 100 \rangle$–aligned structures in Si(100) and observed the formation of $\{111\}$ and $\{110\}$ facets respectively. $\{111\}$ faceting produces defective regions because twin defects can be formed during the recrystallization of $\{111\}$ configurations which is not the case with $\{110\}$ faceting. As a consequence, SPER of $\langle 100 \rangle$–aligned structures has been shown to succeed with a better crystalline quality in contrast to $\langle 110 \rangle$–aligned structures. In box–shaped amorphous regions, SPER proceeds through a lateral and a vertical regrowth fronts competing with each other. As for the regrowth of trench–bounded regions, simulations predict a better crystalline quality after SPER of $\langle 100 \rangle$–aligned box–shaped regions than for $\langle 110 \rangle$–aligned box–shaped regions, in good agreement with experimental observations. In the case of junction formed through SPER at low temperature processing in FDSOI MOSFETs, LKMC simulations show the formation of defective regions bounded by $\{111\}$ facets in $\langle 110 \rangle$–channel devices while a complete regrowth is achieved in $\langle 100 \rangle$–channel devices.

Future developments should address the evolution of twin defects with subsequent thermal treatments. Indeed, Duffy *et al.* observed using high-resolution cross-sectional transmission electron microscopy (XTEM), that regrowth–induced defects can be cured with sufficiently high thermal budgets in germanium structures [Duffy *et al.* 2011]. The implemented LKMC model has also been used to successfully simulate SPER of Ge (see [Darby *et al.* 2013]). Thus, it could be technologically relevant to extend the model in order to simulate the SPER of SiGe alloys that are commonly used to form the source and drain regions in *p*–type MOSFET transistors.

CHAPTER 3

Impact of stress on Solid Phase Epitaxial Regrowth

STRESS has been introduced in advanced CMOS technologies since the 90 nm node in order to enhance the carrier mobility. Thus, the use of strain engineering techniques has become standard in actual MOSFET devices. During the fabrication process of these devices, the physical mechanisms playing a role in the junction formation may be influenced by the presence of a non–hydrostatic stress field. In particular, experimental observations of SPER have shown it exhibits a strong stress–dependence. In this chapter, we extend the SPER LKMC model that has been presented in chapter 2 to include the influence of stress in the microscopic recrystallization rates. This new model has been implemented in the MMonCa simulator and simulation results have been compared with experimental data of single–directional SPER of Si(100) upon different stress states available in the literature. In section 3.1, we describe the conventions and notations used in this chapter. Then, in section 3.2, we present a literature review of the influence of stress on SPER and introduce the concept of activation strain tensor that is the basis of the stress–dependent SPER LKMC model. In section 3.3 we detail the implemented LKMC model and in section 3.4 we compare the simulation results obtained with this new model with experimental data. Finally, in section 3.5 we summarize this chapter and outline possible future developments. It should be pointed out that this chapter is closely based on [Sklenard et al. 2013a, Sklenard et al. 2014].

Contents

3.1 Conventions and notations

We start by clarifying the notations that will be used in this chapter. For sake of clarity, the same convention as in the previous chapter is used to define Cartesian axes: x axis is aligned with the growth direction while y and z axes are the in–plane directions. For convenience, we introduce the vector $\boldsymbol{x}$ (a 1$^{\text{st}}$ order tensor):

$$x_i = \begin{bmatrix} x \\ y \\ z \end{bmatrix}. \tag{3.1}$$

Stress–related 2$^{\text{nd}}$ order tensor is noted $\boldsymbol{\sigma}$ and defined as:

$$\sigma_{ij} = \begin{bmatrix} \sigma_{11} & \sigma_{12} & \sigma_{13} \\ \sigma_{21} & \sigma_{22} & \sigma_{23} \\ \sigma_{31} & \sigma_{32} & \sigma_{33} \end{bmatrix} \tag{3.2}$$

By convention a negative (positive) σ_{ij} value represents a compressive (tensile) stress.

Finally, to simplify notations in tensor operations, we will use Einstein summation convention. For example, taking a 2$^{\text{nd}}$ order tensor $\boldsymbol{\psi}$, the dot product of $\boldsymbol{\psi}$ with $\boldsymbol{\sigma}$ is:

$$\boldsymbol{\psi} \cdot \boldsymbol{\sigma} = \sum_{i,j} \psi_{ij} \sigma^{ij}. \tag{3.3}$$

Using Einstein summation convention, the sum sign can be dropped and the summation is implied by the repeated indices:

$$\boldsymbol{\psi} \cdot \boldsymbol{\sigma} = \psi_{ij} \sigma^{ij}. \tag{3.4}$$

Notice that there is no difference between upper and lower indices in non–relativistic physics, e.g. $\sigma_{ij} = \sigma^{ij}$ and $\psi_{ij} = \psi^{ij}$.

3.2 Background

Historically, the first experimental investigations of stress–influenced SPER concerned the impact of hydrostatic pressure on the recrystallization of Si(100) and Ge(100) samples as shown schematically in Fig. 3.1a [Nygren *et al.* 1985, Lu *et al.* 1989, Lu *et al.* 1991]. More recently, studies have been carried out in order to evidence the influence of a non–hydrostatic stress on SPER in Si(100). In particular, the impact of in–plane and normal uniaxial stresses shown schematically in Fig. 3.1b and 3.1c respectively have been investigated experimentally [Aziz *et al.* 1991, Rudawski *et al.* 2008b, Barvosa-Carter 1997].

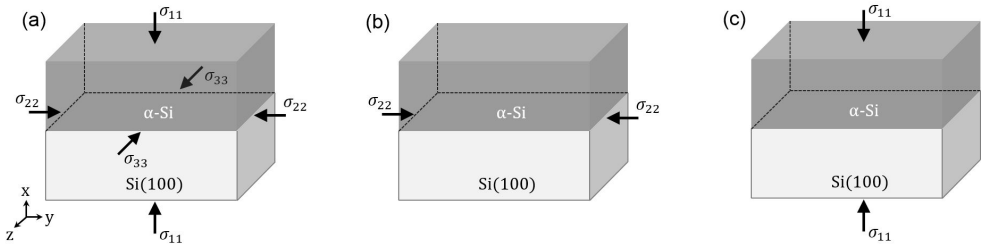

Figure 3.1: Schematics of planar SPER in Si(100) upon (a) hydrostatic pressure, (b) in–plane uniaxial stress and (c) normal uniaxial stress.

In this section, the theoretical impact of a stress state on the transition rate within the framework of Transition State Theory (TST) will be reviewed, first of all for the simple case of hydrostatic pressure (section 3.2.1) and then generalized to a non–hydrostatic stress (section 3.2.2). The different experimental results available in the literature will also be presented and used to confront the theoretical models. We should emphasize that the concept of activation strain tensor, which plays a central role in the stress–dependent SPER LKMC model, will be introduced in section 3.2.2.

3.2.1 Influence of hydrostatic pressure: the notion of activation volume

In previous chapter, we have shown that the regrowth velocity exhibits an Arrhenius behavior described by Eq. 2.6. The energy barrier ΔG^* is a Gibbs free–energy that can be expanded to:

$$\Delta G^* = \Delta E^* - T\Delta S^* + P\Delta V^*, \tag{3.5}$$

where ΔE^* is the activation energy, ΔS^* is the entropy change, P is the hydrostatic pressure and ΔV^* is the volume change. From Eq. 2.6 and by neglecting the temperature dependence of the entropy, the regrowth velocity upon hydrostatic pressure becomes:

$$v = v_0 \times \exp\left(\frac{\Delta S^*}{k_B}\right) \times \exp\left(-\frac{\Delta E^* + P\Delta V^*}{k_B T}\right). \tag{3.6}$$

The volume change ΔV^* is called the activation volume and can be measured in an isothermal pressure–dependent experiment from:

$$\Delta V^* = -k_B T \frac{\partial (\log v)}{\partial P}. \tag{3.7}$$

A negative (positive) activation volume value yields to a decrease (increase) of the energy barrier resulting in a faster (slower) regrowth velocity. Lu *et al.* have measured ΔV^* in undoped Si(100) and Ge(100) using high temperature and high pressure diamond anvil cell (DAC) for pressure up to 5 GPa by monitoring the evolution of α/c interface with *in–situ* time–resolved

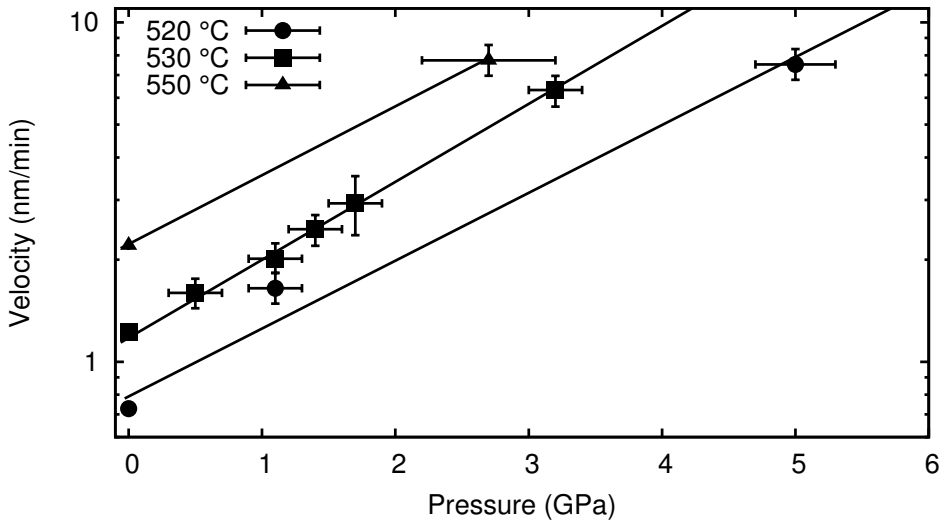

Figure 3.2: Regrowth velocity as a function of hydrostatic pressure in Si(100) at different temperatures from [Lu *et al.* 1991]. Symbols are experimental data and lines correspond to an Arrhenius fit.

interferometry (TRR) [Lu *et al.* 1991]. They found that the SPER rate is exponentially enhanced with pressure for both Si and Ge. They determined negative activation volumes of $-0.28\Omega_{Si}$ and $-0.45\Omega_{Ge}$, where Ω_{Si} and Ω_{Ge} are the silicon and germanium crystalline activation volumes.

3.2.2 Generalization to a non–hydrostatic stress

3.2.2.1 The concept of activation strain tensor

Aziz *et al.* have generalized the concept of activation volume described previously to non–hydrostatic stresses by introducing a 2^{nd} order tensor referred as the activation strain tensor and defined as [Aziz *et al.* 1991]:

$$\Delta V_{ij}^{*} = \begin{bmatrix} \Delta V_{11}^{*} & \Delta V_{12}^{*} & \Delta V_{13}^{*} \\ \Delta V_{21}^{*} & \Delta V_{22}^{*} & \Delta V_{23}^{*} \\ \Delta V_{31}^{*} & \Delta V_{32}^{*} & \Delta V_{33}^{*} \end{bmatrix}. \tag{3.8}$$

The concept of activation strain tensor has been derived from the fluctuation theory similarly to the statistical mechanical treatment of Landau and Lifshitz for fluids under constant hydrostatic pressure [Landau *et al.* 1980]. The complete demonstration is out of the scope of this section but can be found in [Aziz *et al.* 1991]. Similarly to the impact of hydrostatic pressure, the energy barrier upon stress becomes $\Delta E^{*} + \Delta V_{ij}^{*}\sigma^{ij}$ (notice that i and j are summation indices and $\Delta V_{ij}^{*}\sigma^{ij}$ is therefore a scalar). Aziz *et al.* expressed the regrowth velocity as:

$$v = v(\sigma_{ij} = 0) \times \exp\left(\frac{\Delta V_{ij}^{*}\sigma^{ij}}{k_B T}\right), \tag{3.9}$$

where $v(\sigma_{ij} = 0)$ is the stress–free velocity. Again, a negative (positive) activation strain tensor component value will lead to an enhancement (a reduction) of the regrowth velocity in compression and a reduction (an enhancement) of the regrowth velocity in tension with respect to the stress-free velocity. The activation strain tensor components have been measured from different kinds of experiments in Si(100). Indeed, each tensor component is given by:

$$\Delta V_{ij}^{*} = k_B T \frac{\partial\left(\log v\right)}{\partial \sigma_{ij}}. \tag{3.10}$$

For SPER in Si(100), Aziz considered that $\Delta V_{ij}^{*} = 0$ for $i \neq j$ [Aziz 1993] and, by symmetry, $\Delta V_{22}^{*} = \Delta V_{33}^{*} = \Delta V_{\perp}^{*}$ and $\Delta V_{22}^{*} = \Delta V_{\parallel}^{*}$ such as the activation strain tensor can be expressed as:

$$\Delta V_{ij}^{*} = \begin{bmatrix} \Delta V_{\parallel}^{*} & & \\ & \Delta V_{\perp}^{*} & \\ & & \Delta V_{\perp}^{*} \end{bmatrix}. \tag{3.11}$$

Therefore, within Aziz's model the regrowth upon non–hydrostatic stress can be described by a strain activation tensor with two independent components $\Delta V_{\perp}^{*}$ and $\Delta V_{\parallel}^{*}$. Their values have been measured from isothermal SPER experiments in intrinsic Si upon in–plane and normal uniaxial stress, respectively.

Determination of $\Delta V_{\perp}^{*}$ — Aziz *et al.* have carried out measurements of SPER velocity upon in–plane uniaxial stress over a range of ± 600 MPa on elastically bent self–implanted wafers using Rutherford backscattering spectrometry (RBS) and ion channeling techniques

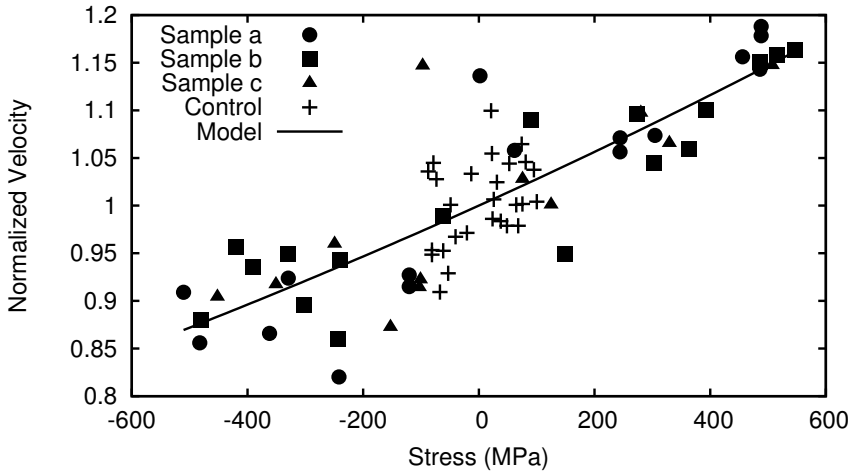

Figure 3.3: Normalized SPER velocity as a function of in–plane uniaxial stress in Si(100) at 540 °C from [Aziz *et al.* 1991]. The line corresponds to the velocity predicted by the model of Aziz *et al.* given by Eq. 3.9: $v = \exp(\Delta V_{\perp}^{*}\sigma_{\perp}/k_B T)$, with $\Delta V_{\perp}^{*} = 0.15\Omega_{\mathrm{Si}}$.

[Aziz *et al.* 1991]. From their results, they obtained $\Delta V_{\perp}^{*} = 0.15 \pm 0.01\Omega_{Si}$. More recently, Barvosa–Carter and Aziz obtained a similar value ($\Delta V_{\perp}^{*} = 0.14 \pm 0.04\Omega_{Si}$) by loading the sample and monitoring the regrowth velocity *in–situ* by time–resolved reflectivy (TRR) [Barvosa-Carter & Aziz 2001]. Barvosa–Carter and Aziz only measured the regrowth velocity for a -0.5 GPa in–plane uniaxial stress. Interestingly, in their experiments they did not observe significant differences between samples regrown with an in–plane uniaxial stress applied along either $\langle 110 \rangle$ or $\langle 100 \rangle$ direction.

Determination of $\Delta V_{\parallel}^{*}$ — The regrowth velocity upon normal uniaxial compression has

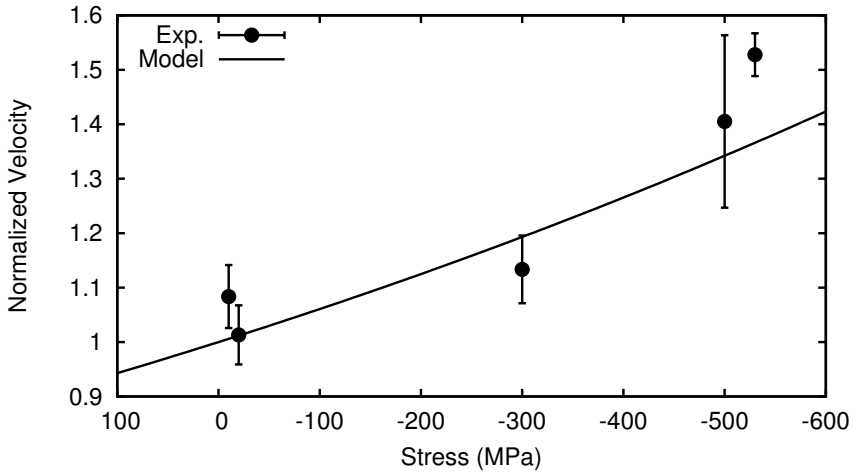

Figure 3.4: SPER velocity as a function of normal uniaxial stress in Si(100) at 540 °C from [Barvosa-Carter & Aziz 1994]. The line corresponds to the velocity predicted by the model of Aziz *et al.* given by Eq. 3.9: $v = \exp(\Delta V_{\parallel}^{*}\sigma_{\parallel}/k_B T)$, with $\Delta V_{\parallel}^{*} = -0.33\Omega_{\mathrm{Si}}$.

been studied by Barvosa–Carter and Aziz [Barvosa-Carter & Aziz 1994, Barvosa-Carter 1997], in order to determine $\Delta V_{\parallel}^{*}$. They used a Si(100) sample with an amorphous layer produced by ion–implantation and applied a normal stress during SPER using a loading apparatus. Experimental details can be found in [Barvosa-Carter & Aziz 1994, Barvosa-Carter 1997]. The

velocity upon stress was determined using *ex–situ* time resolved reflectivity (TRR). To evaluate $\Delta V_{\parallel}^*$, they carried out an isothermal anneal at 540 °C at different stresses. They observed an enhancement of the regrowth velocity with normal uniaxial compression and reported $\Delta V_{\parallel}^* = -0.35\Omega_{Si}$.

Link with the activation volume — In order to get a unified theory between pressure–dependent SPER and non–hydrostatic stress–dependent SPER, the following condition has to be fulfilled:

$$Tr(\Delta V_{ij}^*) \equiv \sum_i \Delta V_{ii}^* = \Delta V^* \tag{3.12}$$

However, from the values of $\Delta V_{\perp}^*$ and $\Delta V_{\parallel}^*$ measured experimentally, we get $Tr(\Delta V_{ij}^*) = -0.05\Omega_{Si}$ which is about 10 times lower than the activation volume in silicon[1]. Unfortunately, $\Delta V_{\perp}^*$ and $\Delta V_{\parallel}^*$ have not been measured in germanium which prevents to draw any conclusion for this material. Nevertheless, in the case of silicon, there seems to be some inconsistencies in Aziz *et al.*'s model. This has given rise to further investigations of stress–dependent SPER by Rudawski *et al.* who proposed a new model based on a dual–timescale process which will be presented hereinafter.

3.2.2.2 A dual–timescale model of stressed SPER

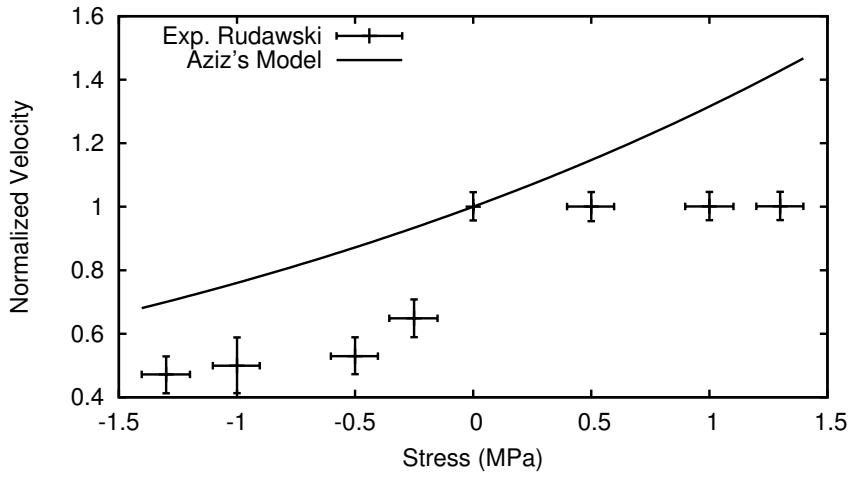

Figure 3.5: Normalized SPER velocity as a function of in–plane uniaxial stress in Si(100). Symbols show experimental results obtained by Rudawski *et al.* at 575 °C [Rudawski *et al.* 2008a]. Line corresponds to Aziz's model [Aziz *et al.* 1991].

Recent measurements of SPER velocity upon in–plane uniaxial stress have been performed by Rudawski *et al.* over a range of ± 1.3GPa (*i.e.* more than twice the range studied by Aziz *et al.*) [Rudawski *et al.* 2008b]. Samples were self–implanted to produce an amorphous layer and annealed at a temperature sufficiently high to induce recrystallization. Stress was applied using a wafer bending technique detailed in [Rudawski *et al.* 2008b] and the evolution of the position of the α/c interface was observed with weak–beam dark–field cross–sectional transmission electron microscopy (WBDF–XTEM). For each applied stress state, they computed an average regrowth velocity using a linear regression on the different α/c interface positions. Fig. 3.5 shows the averaged regrowth velocity as a function of applied stress. Interestingly,

[1] $Tr(\Delta V_{ij}^*) = 2\Delta V_{\perp}^* + \Delta V_{\parallel}^*$

their results exhibit a rather different behavior than those obtained by Aziz *et al.* (see Fig. 3.3). This might be due to the fact that the measurements of Aziz *et al.* are quite scattered. From Fig. 3.5, it is clear that the regrowth velocity is (i) reduced by compressive stress and (ii) not affected by tensile stress. It is also important to notice a saturation of the regrowth velocity for $\sigma_\perp \leqslant -0.5$ GPa.

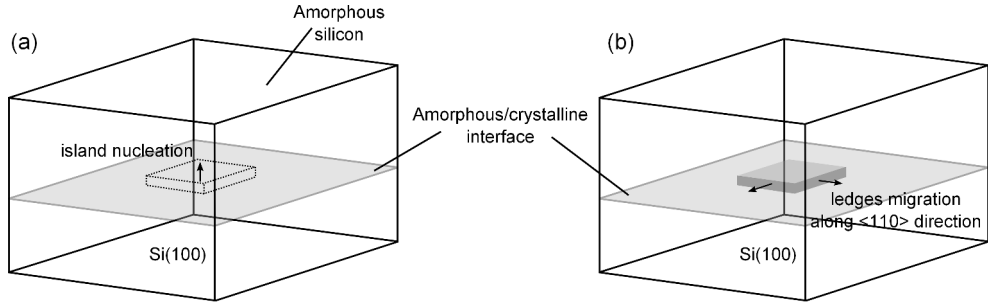

Figure 3.6: Schematic representation of the SPER model from [Williams & Elliman 1983]. (a) Regrowth is initiated by the nucleation of a crystalline island (along $\langle 100 \rangle$ direction). (b) The crystalline island further expands through the migration of $\langle 110 \rangle$ ledges.

The model of Aziz *et al.* cannot predict the data obtained by Rudawski *et al.* suggesting that the underlying physical mechanisms are more complex. Rudawski *et al.* proposed another empirical model [Rudawski *et al.* 2008a]. Recently they improved their model by including more physical insight in order to get a good agreement with their results over a larger temperature range [Rudawski & Jones 2009]. In this manuscript, we will not enter into the details of their model but we will present the physical assumption they used to build it. Their approach is based on the work of Williams and Elliman suggesting that SPER proceeds through a dual–timescale process illustrated in Fig 3.6 [Williams & Elliman 1983]. According to this model, SPER of a planar α/c interface starts with the nucleation of crystalline islands (Fig. 3.6a) which further expand through the migration of ledges along $\langle 110 \rangle$ direction (Fig. 3.6b). In that case, the regrowth velocity is given by:

$$v = \frac{h}{\tau_n + \tau_m} \tag{3.13}$$

where h is the regrown monolayer height and τ_n and τ_m are the timescale of regrowth processes; n and m indices refer to nucleation and migration processes, respectively. Ledge migration process is much faster than nucleation such as $\tau_n \gg \tau_m$ and the regrowth velocity is therefore driven by crystalline island nucleation. Upon a non–hydrostatic stress state, the nucleation timescale can be written in terms of a nucleation activation strain tensor ΔV_{ij}^n yielding:

$$\frac{1}{\tau_n} = \frac{1}{\tau_n(\sigma_{ij} = 0)} \times \exp\left(\frac{\Delta V_{ij}^n \sigma^{ij}}{k_B T}\right). \tag{3.14}$$

On the other hand, the ledge migration can be described by a 2^{nd} order tensor corresponding to the ledge mobility and given by:

$$M_{kl} = M_{kl}(\sigma_{ij} = 0) \times \exp\left(\frac{\Delta V_{ij}^{m,kl} \sigma^{ij}}{k_B T}\right), \tag{3.15}$$

where $\Delta V_{ij}^{m,kl}$ happens to be the 4^{th} order strain activation tensor associated with the ledges mobility. From these observations, Rudawski *et al.* derived an expression of the regrowth velocity upon in–plane uniaxial stress (see [Rudawski & Jones 2009] for further details) which

could fit their experimental data. In their model, an in–plane uniaxial stress happens to reduce (enhance) the ledge migration velocity in compression (tension) and has no impact on the nucleation process. The enhancement of the migration velocity has no effect on the macroscopic SPER velocity because it is controlled by nucleation. In contrast, a reduction of the migration velocity affects directly the regrowth velocity. It is also worth noting that a roughening of the α/c interface was evidenced by WBDF-XTEM images for $\sigma_\perp < 0$. Rudawski *et al.* explained this enhancement of the interface roughness by the difference of local stress at peaks and troughs of the interface (presumably existing after ion–implantation) which tends to amplify this morphological instability. This particular aspect will be discussed in the frame of the stress-dependent SPER LKMC model which offers further insights into the phenomena occurring at the α/c interface (see section 3.4.1.2).

3.3 LKMC Model

As it has been shown in section 3.2.2, within TST, the dependence upon a stress state $\boldsymbol{\sigma}$ of the phase transition frequency is characterized by the activation strain tensor $\boldsymbol{\Delta V^*}$; the energy barrier that has to be overcome during a transition becomes $E^* + \boldsymbol{\Delta V^* \sigma}$. Hence, the stress–free transition frequency given by Eq. 2.13 becomes:

$$\nu(n, \boldsymbol{\sigma}, T) = K(n) \times \exp\left(-\frac{E^* + \boldsymbol{\Delta V^* \sigma}}{k_B T}\right). \tag{3.16}$$

We also introduce $\boldsymbol{d}(n)$, the normalized regrowth direction of the configuration n such as the recrystallization event of a configuration occurs along an orthogonal direction $\boldsymbol{d}$ to the configuration plane. This is illustrated in Fig. 3.7 for a $\{100\}$ event. In the three–dimensional

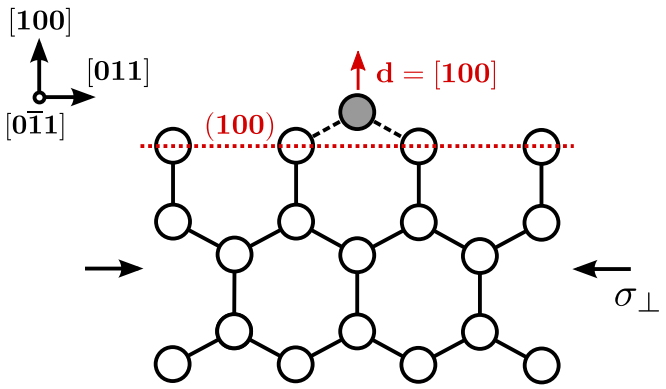

Figure 3.7: Schematic recrystallization of a $\{100\}$ configuration upon in-plane uniaxial stress applied along [011] direction. Regrowth is assumed to proceed along the direction $\boldsymbol{d}$ that is orthogonal to the configuration plane.

case, we define the activation strain tensor ΔV^*_{ij} as:

$$\Delta V^*_{ij} = \Delta V^*_\parallel d_i d_j + \Delta V^*_\perp (\delta_{ij} - d_i d_j), \tag{3.17}$$

where $\Delta V^*_\parallel$ and $\Delta V^*_\perp$ correspond to the dimension changes parallel and perpendicular to the regrowth local direction at the saddle point of the amorphous to crystalline transition, d_i and d_j are the Cartesian components of the vector $\boldsymbol{d}$ and δ_{ij} is the Kronecker delta:

$$\delta_{ij} = \begin{bmatrix} 1 & 0 & 0 \\ 0 & 1 & 0 \\ 0 & 0 & 1 \end{bmatrix}. \tag{3.18}$$

Table 3.1: Values of the components of activation strain tensors depending on the number of crystalline nearest neighbors of the configuration. Ω_{Si} represents the molar volume of silicon.

Configuration	$\Delta V_{\parallel}^{*}$ (Ω_{Si})	$\Delta V_{\perp}^{*}$ (Ω_{Si})
$\{100\}_2$	-0.33	0
$\{100\}_3$	-26	13

The scope of this manuscript is limited to the stress–dependence of $\{100\}$ events driving the SPER of Si(100). For this reason, no stress–dependence is included for $\{110\}$ and $\{111\}$ events. As it has been discussed in section 3.2.2, a unique activation strain tensor in Eq. 3.16 cannot explain the experimental results of Rudawski *et al.* [Rudawski *et al.* 2008a] upon in–plane uniaxial stress. It would also be inconsistent with the activation volume ΔV^{*} because $Tr(\Delta V_{ij}^{*}) \neq \Delta V^{*}$.

The model therefore distinguishes two different activation strain tensors for $\{100\}$ configurations having two ($\{100\}_2$) or three ($\{100\}_3$) crystalline neighbors. An atom tagged as *amorphous* having only one *crystalline* neighbor cannot be a $\{100\}$ configuration; if it has four *crystalline* neighbors it is *crystalline* by definition. It might appear as rather intuitive that for a given stress state, the energy barrier that has to be overcome to perform an amorphous to crystalline transition will differ between $\{100\}_2$ and $\{100\}_3$ configurations and will depend on the values of $\Delta V_{\parallel}^{*}$ and $\Delta V_{\perp}^{*}$. We should emphasize that the first nearest neighbor dependence is actually the simplest one and gives rise to only four independent activation strain tensor components. The values of $\Delta V_{\parallel}^{*}$ and $\Delta V_{\perp}^{*}$ are summarized in Table 3.1 and will be detailed in the next section.

It is worth noting that the distinction between $\{100\}_2$ and $\{100\}_3$ configurations can be compared with the nucleation and migration processes in the Rudawski *et al.* model [Rudawski *et al.* 2008b]. Indeed, $\{100\}_2$ configurations happen to be a particular case of $\{100\}_l$ configurations while $\{100\}_3$ ones can be either $\{100\}_l$ or $\{100\}_h$ configurations. In particular, as it as been shown in the previous chapter, the rate of $\{100\}_h$ configurations is one order of magnitude higher than the one of $\{100\}_l$ configurations resulting in dual–timescale process. As a consequence, the LKMC algorithm performs *per se* a competition between two processes at a macroscopic scale, namely the nucleation of crystalline islands, and their expansion via the migration of the ledges. Moreover, the LKMC model provides an atomistic description of the interface at different stages of the regrowth and can predict faceting and defects formation.

3.4 Atomistic simulation of SPER upon stress

We have used the stress–dependent SPER LKMC model presented in the previous section to study the evolution of the α/c interface upon a non–hydrostatic stress field (sections 3.4.1 and 3.4.2) and hydrostatic pressure (sections 3.4.3) during SPER of Si(100). For these studies, a $105 \times 80\sqrt{2}a_0 \times 80\sqrt{2}a_0$ nm^3 simulation cell has been considered, where a_0 is the basic unit cell length (0.5431 nm). The simulation domain was bonded by two $\{001\}$ planes along x direction and four $\{011\}$ planes along y and z directions. The simulation domain at the beginning of the simulation is shown in Fig. 3.8. A 100 nm thick amorphous layer with an atomically flat α/c interface has been recrystallized such as regrowth occurs along $\langle 100 \rangle$ direction while periodic boundary conditions are applied in the $\langle 110 \rangle$ lateral directions. After $\sim$ 20 nm of the α-layer has been regrown (red plane in Fig. 3.8) the distribution of the positions

of the atoms at the α/c interface is monitored every 70000 events. Finally the simulation has been stopped after $\sim$ 80 nm of the α-layer has been regrown (blue plane in Fig. 3.8).

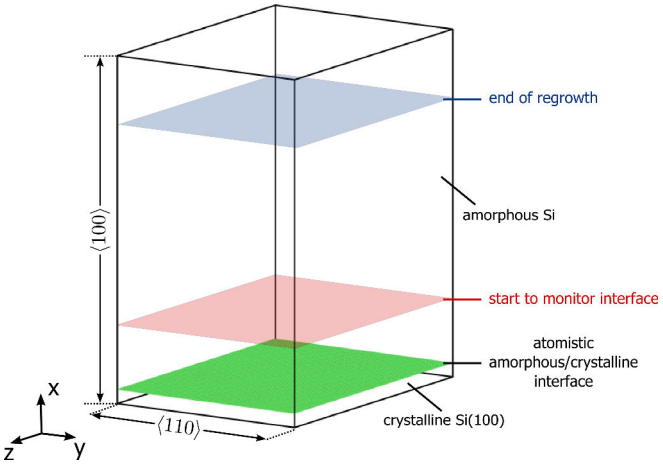

Figure 3.8: Snapshot of the simulation domain at the beginning of the simulation. A $105 \times 80\sqrt{2}a_0 \times 80\sqrt{2}a_0$ nm^3 simulation has been considered, a_0 being the basic unit cell length (0.5431 nm), with a 100 nm thick amorphous layer.

It should be emphasized that the applied stress is assumed to be uniform over the whole simulation domain. On the other hand, the effect of the viscosity of α-Si has been neglected [Witvrouw & Spaepen 1993]. This assumption could be relaxed by coupling our model with a mechanical solver and modeling the amorphous solid by Stokes flow with a time-dependent viscosity as in [Barvosa-Carter *et al.* 2004]. However, in the frame of an atomistic model, the coupling between a continuum field and particles is not straightforward and implies several complications. Further work is being done to address this topic but is out of the scope of this chapter.

3.4.1 In–plane uniaxial stress

3.4.1.1 Regrowth velocity

During the α/c transition of $\{100\}_2$ configurations, as for the formation of a point defect at an interface [Aziz *et al.* 2006], the volume change occurs in the growth direction rather than in the in-plane direction, thus $\Delta V_\perp \sim 0$. In contrast, the transition of $\{100\}_3$ configurations causes a high volume expansion in the in-plane direction to allow the bonds to rearrange. The high $\Delta V_\perp$ value for $\{100\}_3$ configurations results from the fact that the transition necessitates the motion of multiple surrounding atoms to occur.

Fig. 3.9 shows the simulated regrowth velocity at 575 °C as a function of in–plane uniaxial stress $\sigma_\perp$ (see Fig. 3.1b for schematic representation), compared with experimental measurements taken from [Rudawski & Jones 2009] and showing an excellent agreement. The velocities in stress conditions were normalized with the stress-free value. When tensile stress is applied ($\sigma_\perp > 0$), no noticeable variation of the macroscopic interface velocity is observed. In contrast, under compressive stress ($\sigma_\perp < 0$) the velocity is reduced ($\sim 40\%$ for $\sigma_\perp < -0.5$ GPa).

The observed behavior can be explained by considering the kinetics of the microscopic events upon stress within our model. When no stress is applied, $\nu(\{100\}_l)$ is about one order of magnitude lower than for $\nu(\{100\}_h)$ ($K(\{100\}_h) \sim 10K(\{100\}_l)$). Then, the macroscopic regrowth velocity is limited by $\{100\}_l$ events. Similarly, in tension, the rate of $\{100\}_3$ events

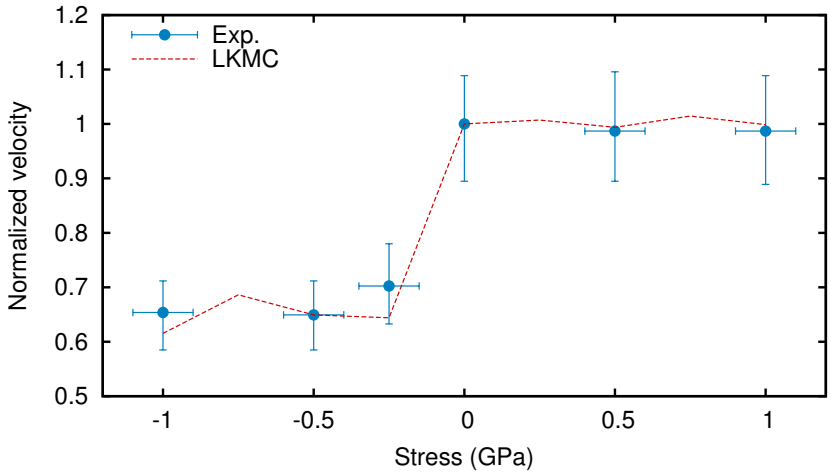

Figure 3.9: Evolution of normalized regrowth velocity as a function of in-plane uniaxial stress ($\sigma_\perp$). Experimental data (symbols) are taken from [Rudawski *et al.* 2008b] for a 575 °C anneal.

– that are a particular case of $\{100\}_h$ events – is increased, hence the macroscopic regrowth velocity remains limited by $\{100\}_l$ events and the situation is unchanged with respect to the stress free case. In contrast, in compression, the rate of $\{100\}_3$ events is reduced by a factor $\exp(\Delta V_\perp^* \sigma_\perp / kT)$. Therefore, the reduction of the rate of certain $\{100\}_h$ configurations destabilizes the growth kinetics leading to a lowering of the macroscopic velocity. However, the velocity cannot decrease indefinitely since it is related to the rate of $\{100\}_3$ configurations that are finite. Then, the velocity reduction saturates when $\{100\}_3$ configurations do not contribute to phase transition anymore (for $\sigma \lesssim -0.5$ GPa).

From this analysis, one can give some additional interpretation of Fig. 3.9:

1. the slope of the velocity reduction in compression before reaching the saturation is determined by $V_\perp^*$ associated to $\{100\}_3$ configurations,

2. the value of the velocity saturation in compression is determined by the competition between $\{100\}_l$ and remaining $\{100\}_h$ events.

It is important to point out that the rates of $\{100\}_l$ and $\{100\}_h$ events are calibrated using the experimental stress free data of [Csepregi *et al.* 1977] as shown in previous works [Martin-Bragado & Moroz 2009, Martin-Bragado & Sklenard 2012]. Then, the impact of stress is only determined by the values of the activation strain tensors and the value of the velocity saturation is a consequence of the model.

3.4.1.2 Interface roughness

It is interesting to correlate the regrowth velocity with the evolution of the interface roughness shown in Fig. 3.10. Under compressive stress, the interface becomes morphologically unstable and the roughness increases while for tensile stress, the roughness is close to the stress free reference, in good agreement with experimental observations [Barvosa-Carter *et al.* 1998, Barvosa-Carter *et al.* 2004, Sage *et al.* 2000, Rudawski *et al.* 2008a]. In particular, Barvosa–Carter *et al.* have measured the evolution of interface roughness in B doped samples using time–resolved reflectivity and have reported an enhancement by a factor 1.5–2 at -0.5 GPa [Barvosa-Carter *et al.* 2004] which corresponds to the range we obtain in our simulations. It

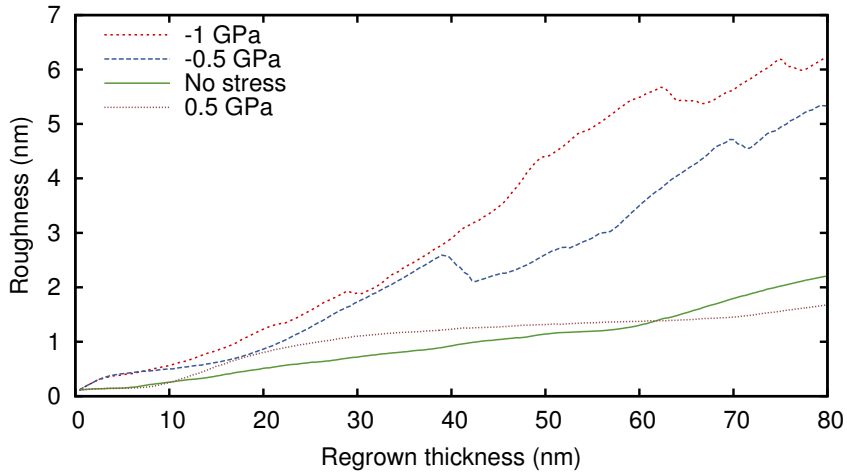

Figure 3.10: Evolution of the α/c interface roughness predicted by LKMC simulations during a 575 °C upon different in-plane uniaxial stress states (σ_{22}).

has to be pointed out that the roughness is a consequence of our model and there is no adjustable parameter. Indeed, configurations with three crystalline neighbors (and more generally $\{100\}_h$ configurations) play a role in the "planarization" of the α/c interface. Then, the reduction of their rate as it is the case under compressive stress breaks this planarization process and contributes to increase the interface roughness. For this reason, starting with an atomically flat interface, we observe (i) a progressive roughening of the interface for $\sigma_{22} < 0$, (ii) a morphologically stable interface under stress free conditions and (iii) no particular influence of tensile stress on interface roughness. Note that our atomistic interpretation of the evolution of interface roughness upon stress contrasts with previous studies. Indeed, morphological instability was assumed to be the result of a stress variation between peaks and troughs at the α/c interface giving different local regrowth velocities and causing the roughness to increase [Barvosa-Carter *et al.* 1998, Sage *et al.* 2000, Rudawski *et al.* 2008a]. Instead, our work proposes an alternative atomistic mechanism that explains, not only the stress influence, but also the potential cause for interface roughening in terms of different responses of the microscopic configurations to a stress field.

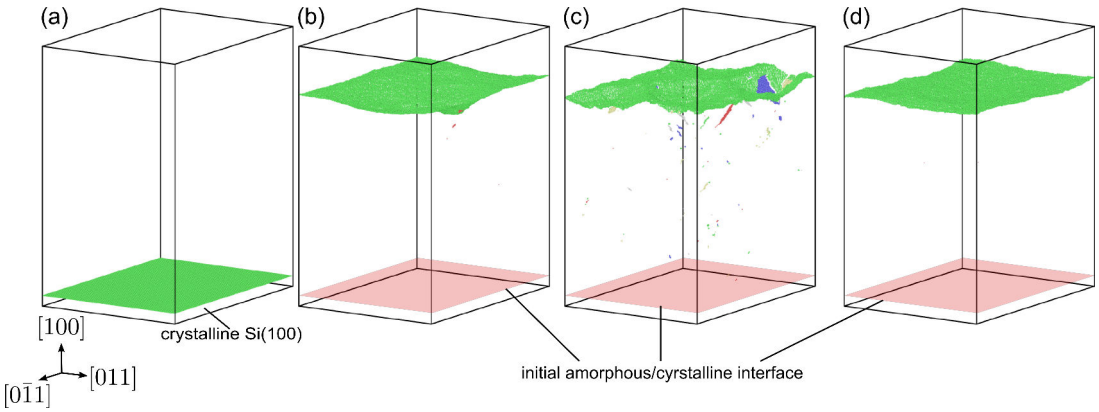

Figure 3.11: Snapshots of the evolution of the α/c interface upon in–plane uniaxial stress: (a) initial structure and after the regrowth of ∼80 nm at 575 °C (b) without applied stress, (c) upon -0.5 GPa in–plane stress and (d) upon 0.5 GPa in–plane stress.

Experimental observations of stressed SPER have shown that regrown layers are very defective upon compressive stress [Barvosa-Carter *et al.* 2004, Rudawski *et al.* 2008b]. However, no dedicated study has been carried out to determine the character of the observed defects. Similarly, SPER of SiGe epilayers on Si with an amount of Ge higher than 3–7% has been shown to be defective, which should result in a degradation of the device performances [Sage *et al.* 2006]. The formation of these defects has been attributed to the increase of interface roughness. The LKMC model accounts for the formation of twins on {111} facets that can lead to different defective configurations, as it has been shown in the previous chapter. Simulation snapshots at the end of the regrowth for different in–plane uniaxial stress states are shown in Fig. 3.11. Without applied stress (Fig 3.11b), the α/c interface is planar and very few defective configurations have been formed. In contrast, for -0.5 GPa stress, the α/c interface is very rough, and we identify many defective configurations in the regrown region (Fig 3.11c). This shows how compressive stress induces roughness that in turn produces twins. Once the twins start appearing, they facilitate further roughening. As expected from the evolution of the interface roughness shown in Fig. 3.10, tensile stress leads to a similar behavior than without any applied stress (Fig 3.11d).

3.4.2 Normal uniaxial stress

Fig. 3.12 shows the evolution of the regrowth velocity as a function of a uniaxial compressive stress applied perpendicular to the α/c interface ($\sigma_{\parallel}$). Molecular dynamics data from [Bernstein *et al.* 2000] and experimental data from [Barvosa-Carter 1997] are also reported. Simulation results are in reasonable agreement with both experimental and molecular dynamics data. In contrast to in-plane uniaxial stress, an enhancement of the regrowth velocity is observed when an uniaxial compressive stress is applied. This effect results from the negative activation volume $\Delta V^*_{\parallel}$ for both $\{100\}_l$ and $\{100\}_h$ events. On the other hand, the large activation volume for configurations with three crystalline neighbors does not seem to affect the macroscopic regrowth velocity suggesting that SPER is still limited by $\{100\}_l$ events. For this reason, the previous studies of Aziz *et al.* and Barvosa–Crater and Aziz assuming that SPER occurs through a single atomistic mechanism predicted a similar activation volume to that used in our work for configurations with two crystalline neighbors [Barvosa-Carter 1997, Aziz *et al.* 1991].

3.4.3 Hydrosatic pressure

Simulation results of regrowth velocity as a function of hydrostatic pressure ($\sigma_{11} = \sigma_{22} = \sigma_{33}$) are reported in Fig. 3.13 and compared with experimental data of Lu *et al.* [Lu *et al.* 1991]. We observe an enhancement of regrowth velocity with hydrostatic pressure, in good agreement with experimental data of Lu *et al.* and with predictions of molecular dynamics simulations [Bernstein *et al.* 2000, Shanavas *et al.* 2012]. This behavior is very close to the evolution of α/c interface with normal uniaxial stress and linked to the fact that the regrowth velocity is limited by $\{100\}_l$ events. However, the study of SPER under pressure has permitted us to calibrate the large activation volume for configurations with three crystalline neighbors ($\Delta V^*_{\parallel} = -2\Delta V^*_{\perp}$). The negative activation volume for {100} configurations (and therefore the SPER velocity enhancement) suggests a volumetric compression during phase transition which is consistent with the difference of densities between amorphous and crystalline materials [Custer *et al.* 1994].

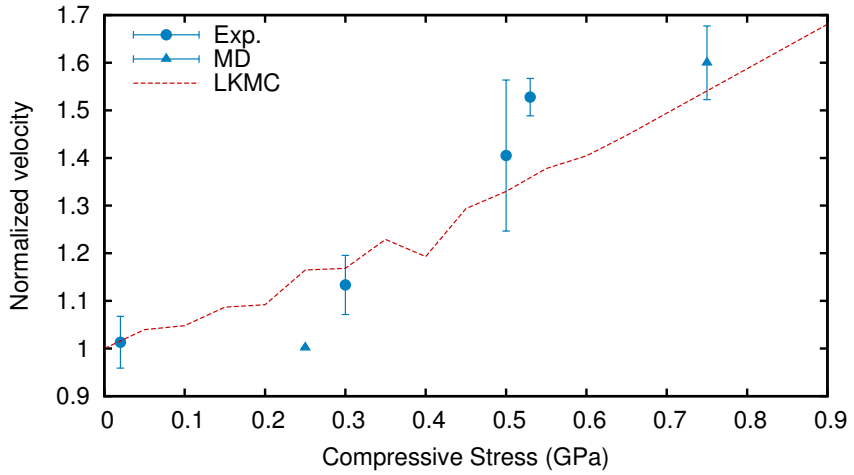

Figure 3.12: Evolution of normalized regrowth velocity as a function of normal uniaxial compressive stress (σ_{11}). Experimental data (circle symbols) are taken from [Barvosa-Carter 1997] and molecular dynamics (MD) data (triangle symbols) from [Bernstein *et al.* 2000].

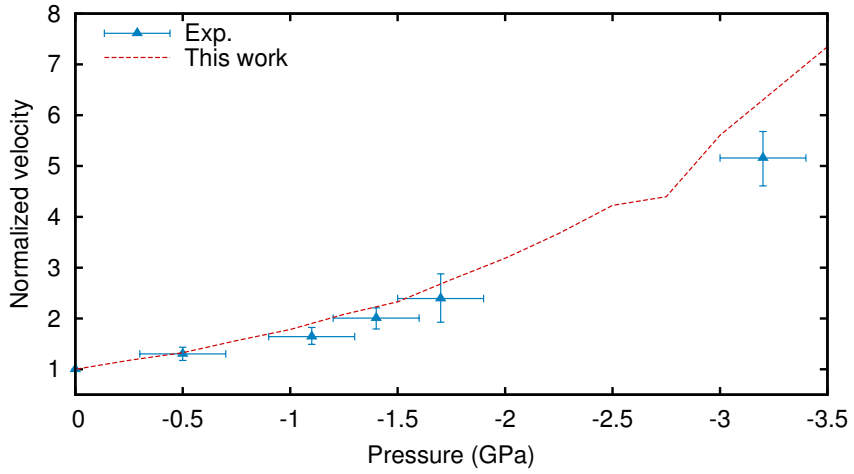

Figure 3.13: Evolution of normalized regrowth velocity as a function of hydrostatic pressure ($\sigma_{11} = \sigma_{22} = \sigma_{33}$). Experimental data (symbols) are taken from [Lu *et al.* 1991] for a 530 °C anneal.

3.5 Summary

In this chapter, the stress–dependent SPER of Si(100) has been examined under different stress states using the LKMC model implemented in MMonCa. The model relies on a correction of the transition rate given by:

$$\nu = \nu(\sigma_{ij} = 0) \times \exp\left(\frac{\Delta V^*_{ij}\sigma^{ij}}{k_B T}\right), \tag{3.19}$$

where ΔV^*_{ij} is the activation strain tensor [Aziz *et al.* 1991], σ_{ij} is the stress tensor, $\nu(\sigma_{ij} = 0)$ is the stress-free rate and $k_B T$ has the usual meaning. It turns out that depending on the sign of the activation strain tensor component, the correction will lead to an increase or a reduction of the transition rate. Typically a negative (positive) value will result in an enhancement (a reduction) of the transition rate in compression ($\sigma < 0$) and the contrary in tension ($\sigma > 0$).

In the LKMC model, a distinction is made between {100} configurations with two and three *crystalline* neighbors leading to two distinct activation strain tensors. By symmetry,

$\Delta V_{22}^* = \Delta V_{33}^* = \Delta V_{\perp}^*$ and $\Delta V_{11}^* = \Delta V_{\parallel}^*$ and off-diagonal components are zero. Therefore, the model contains 4 independent parameters for non–hydrostatic stress–dependent SPER.

We have shown that the LKMC model improves the understanding of the phenomena occuring at the atomistic scale during stressed SPER of Si(100):

- The study of the impact of in–plane uniaxial stress on the macroscopic regrowth velocity shows no influence of tensile stress but a significant reduction in compression. The velocity reduction upon compressive stress results from a decrease of the transition rate of $\{100\}$ configurations bonded to three *crystalline* atoms leading to an enhancement of the amorphous/crystalline interface roughness. This model is in contrast with the previous theoretical models of the evolution of the morphological instabilities which suggested that the roughness results from variations of the stress states at peaks and troughs of the interface. Additionally, the roughness enhancement of the interface in compression is shown to lead to the formation of defective $\{111\}$ facets.

- Stressed SPER upon a compressive normal uniaxial stress appears as very close to the recrystallization under hydrostatic pressure. In both cases, SPER exhibits an exponential enhancement of the regrowth velocity with the same magnitude.

Finally, we should emphasize that the LKMC model explains the inconsistencies between the strain activation tensor and activation volume obtained with Aziz's model. The difference relies in the introduction of two activation strain tensors corresponding to two distinct atomistic mechanisms suggesting that (100) SPER occurs through a dual–timescale process.

In this PhD, we have expanded the LKMC model in order to account for the influence of an arbitrary stress field on the regrowth kinetics of $\{100\}$ microscopic configurations that play the main role during SPER of Si(100) substrates. Further developments may be carried out in order to generalize this model to $\{110\}$ and $\{111\}$ microscopic configurations in order to take into account the influence of stress on an arbitrary orientation. In particular, such an improvement could allow the study of the influence of stress on multidirectional SPER that is of great technological interest.

CHAPTER 4

Influence of impurities on Solid Phase Epitaxial Regrowth

TECHNOLOGICALLY, the SPER process is used to form junctions since it allows to incorporate dopants into substitutional lattice site positions. In particular, it allows to achieve (i) very abrupt junctions by using a low processing temperature (typically $\leqslant$ 600 °C) with respect to a conventional process and (ii) highly activated junctions exceeding solid solubility which are very suitable for advanced device scaling. There is therefore a strong interest in introducing the influence of impurities on SPER in the LKMC model. In this chapter, we propose an extension of the LKMC model to take into account dopant–enhanced regrowth velocity arising from the presence of electronic active impurities.

Contents

4.1 Background

4.1.1 Solid solubility and metastable solubility

In this section we will start by reviewing the concept of solid solubility which is an important property to characterize the solubility of impurities in a crystalline material at equilibrium (section 4.1.1.1). Solid solubility is technologically relevant since it is related to the maximum activation level that can be expected for a given impurity. In the case of dopant activation obtained by solid phase epitaxial regrowth, supersaturated solutions result in free–carrier concentration far exceeding the solid solubility which is of high interest for the junction formation

in advanced electronic devices. This maximum achievable out–of–equilibrium solubility is called metastable solubility and will be discussed in section 4.1.1.2.

4.1.1.1 Solid solubility

The solid solubility of an impurity is defined as the maximum concentration leading to an homogeneous solution with the solid host at thermal equilibrium. Above this limit, an heterogeneous phase transformation occurs resulting in the formation of a precipitate phase (for example, rhombohedral SiB_4 for boron in silicon and monoclinic SiAs and SiP for arsenic and phosphorus respectively). Conventional dopants used in microelectronics have a relatively high solid solubility in silicon and tend to occupy substitutional site positions at equilibrium where they are electrically active. However, for some species, at a concentration below solubility limit, it becomes energetically more favorable to form electrically inactive dopant complexes. In that case, the solubility limit does not correspond to the maximum dopant activation. We should point out that this distinction may lead to some confusions in the literature since some authors consider the solubility limit as the activation limit.

In presence of other impurities or lattice damage, clustering phenomena may also occur at lower concentrations being driven by kinetics. This is typically the case during junction formation of microelectronic devices. Dopants are incorporated into the Si lattice through ion–implantation resulting in the generation of defects (self–interstitials and vacancies) that can interact with implanted dopants during subsequent annealing. Upon certain conditions (prolonged anneals at high temperature), the equilibrium can be attained and the relative defect concentrations (dopants in substitutional position or in complexes) can be predicted by thermodynamics [Zhang & Northrup 1991]. From a technological point of view, the equilibrium is generally not reached after the annealing steps involved in the fabrication process of advanced devices. Therefore, continuum or atomistic process simulation are of great interest to predict the time evolution of the system in order to have an insight in the mechanisms leading to dopant activation or deactivation depending on the process conditions. In this section, we restrict our attention to thermal equilibrium situations and present a comprehensive theoretical approach of the concept of solid solubility of impurities in crystalline materials.

At thermal equilibrium, the concentration of an impurity X is given by:

$$[X]^* = C_{sites} \times \exp\left(-\frac{G_f(X)}{k_B T}\right) \tag{4.1}$$

where C_{sites} is the site concentration and G_f is the formation energy being a Gibbs–free energy defined as $G_f \equiv H_f - TS_f$ where H_f and S_f are the formation enthalpy and entropy, respectively [Van de Walle *et al.* 1993]. G_f includes a pressure–dependent contribution in the enthalpy term which can be neglected for a solid phase. The formation entropy S_f is also generally neglected (see [Van de Walle *et al.* 1993, and references therein]) yielding $G_f \approx E_f$, where E_f is the internal energy change upon the presence of X. The formation energy is dependent on the chemical potentials of the atomic constituents, and, in the case of a charged impurity of charge Q, on the electron chemical potential μ_e [Zhang & Northrup 1991].

$$E_f(X^Q) = \Delta E_{tot}(X^Q) - \mu_X + Q\mu_e, \tag{4.2}$$

where ΔE_{tot} is the total internal energy variation resulting from the presence of the impurity X and can be determined using first–principles calculations by $\Delta E_{tot} = E_{tot}^X - E_{tot}^{ref}$, where E_{tot}^X and E_{tot}^{ref} are the total energy of supercells with and without the impurity X in charge state Q [Zhang & Northrup 1991, Van de Walle *et al.* 1993, Northrup & Zhang 1993]

and μ_X is the chemical potential of the impurity X in cluster. It has to be emphasized that chemical potentials have to satisfy some constraints and may vary over a limited range [Van de Walle *et al.* 1993]. For example, the restriction for the electron chemical potential is $0 \leqslant \mu_e \leqslant E_g$, where E_g is the gap of the host material.

The solid solubility is obtained by minimizing E_f. As it has been previously mentioned, for common dopants in silicon, this is generally achieved when the impurity is in substitutional lattice position. In this case, the sites concentration in Eq. 4.1 corresponds to the atomic density of silicon ($N_{Si} = 5 \times 10^{22}$ at/cm^3) yielding:

$$[SS] = N_{Si} \times \exp\left(-\frac{E_f^{min}}{k_B T}\right) \tag{4.3}$$

If all impurities are in substitutional position, $\mu_X = 0$ and $E_f^{min}(X^Q) = \Delta E_{tot}(X^Q) + Q\mu_e$. The solubility limit can therefore be computed by coupling first–principles calculations and a self–consistent calculation of Eq. 4.3 (see for example [Luo *et al.* 2003] for the case of B in Si).

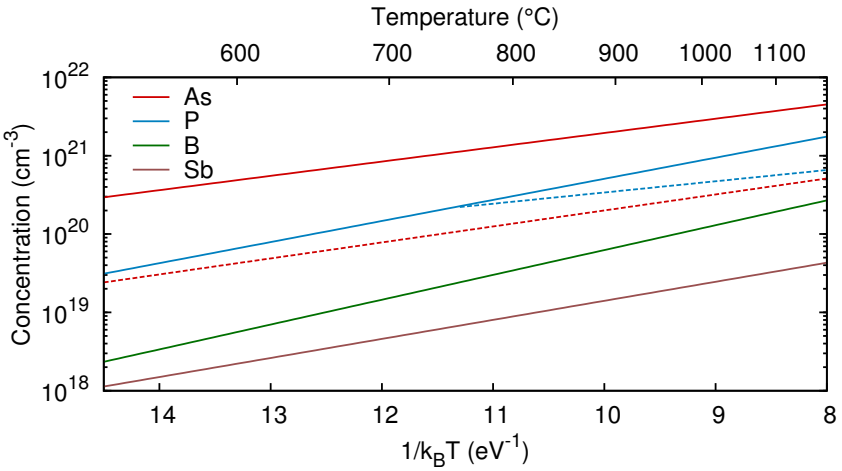

Figure 4.1: Arrhenius plot of experimental solid solubility of As, P, Sb and B (lines) and maximum carrier concentrations (dashed lines) in Si. Pre–exponential factors and activation energies are summarized in Table 4.1.

From a more pragmatic point of view, solubility limits for common dopants in Si have been measured experimentally (see [Solmi 2001] for details) and are reported in Fig. 4.1. Solubility limits can be empirically modeled by an Arrhenius' equations: $[SS] = C_0 \times \exp(-E_a/k_B T)$. The values of the pre–exponential factor C_0 and E_a corresponding to the solid solubility reported in Fig. 4.1 are summarized in Table 4.1. Interestingly, for B or Sb doped Si, the carrier concentration at equilibrium corresponds to the solubility limit. In other words, for concentrations below the solubility limit, B and Sb dopants are electrically active and above this limit precipitation phenomena occur [Solmi *et al.* 1990, Nobili *et al.* 1989]. In contrast, As and P exhibit a high solid solubility in Si which is higher than the maximum carrier concentration at equilibrium n_e. Indeed, electrical inactive As or P complexes are stable at equilibrium and coexist with dopants in substitutional position resulting in a lower carrier concentration [Nobili *et al.* 1994, Solmi *et al.* 1996]. The experimental values of n_e are also reported in table 4.1 and are shown with dashed lines in Fig. 4.1.

Table 4.1: Solid solubilities of various impurities in silicon.

Species	Property	C_0 (cm^{-3})	E_a (eV)	Reference
As	[SS]	1.3×10^{23}	0.42	[Nobili *et al.* 1994]
	n_e	2.2×10^{22}	0.47	[Nobili *et al.* 1994]
P	[SS]	2.5×10^{23}	0.62	[Solmi *et al.* 1996]
	n_e[a]	9.2×10^{21}	0.33	[Solmi *et al.* 1996]
Sb	[SS]	3.81×10^{23}	0.56	[Nobili *et al.* 1989]
B	[SS]	9.25×10^{22}	0.73	[Solmi *et al.* 1990]

[a]Only at high temperature (T > 750 °C)

4.1.1.2 Metastable Solubility

During SPER, dopant atoms confined in the as–implanted amorphous layer are incorporated into crystal lattice sites at concentration levels exceeding the solid solubility of the impurity in silicon [Narayan & Holland 1982, Duffy *et al.* 2006]. As a consequence, SPER allows to reach very high activation levels which are particularly suitable for the junction formation of advanced electrical devices. The maximum achievable concentration is often called metastable solubility. Indeed, this situation corresponds to a metastable equilibrium and with further annealing the system returns to thermodynamic equilibrium (*i.e.* solid solubility).

Narayan and Holland proposed a theoretical model to predict the maximum solubility of impurities in substitutional position during SPER based on a thermodynamical approach [Narayan & Holland 1982, Narayan *et al.* 1983]. They used the arguments of Cahn *et al.* for metastable solubility during liquid phase epitaxy (LPE) [Cahn *et al.* 1980] considering that the maximum solubility is achieved when the free–energy change of the phase transformation is equal to the strain energy due to the incorporation of the impurity. In the case of SPER, the maximum concentration is obtained when:

$$\Delta G_{ac} = \Delta G_{strain} \tag{4.4}$$

where ΔG_{ac} is the crystallization free energy (see section 2.1.1) and ΔG_{strain} is the strain free energy due to the incorporation of the impurity. Since entropy terms are small with respect to enthalpy terms, Eq. 4.4 can be written:

$$\Delta H_{ac} = \Delta H_{strain} \tag{4.5}$$

Narayan and Holland evaluated ΔH_{strain} following continuum elasticity theory of Eshelby and Friedel [Eshelby 1956] yielding:

$$\Delta H_{strain} = \frac{2\gamma\mu_H C_I}{3}\frac{(V_I - V_H)^2}{V_H} \tag{4.6}$$

where $\lambda = 1 + 3\mu_H/4K_I$, μ_H is the shear modulus of the host, K_I the bulk modulus of the solute, C_I is the impurity concentration, and V_I and V_H are impurity and host atoms volumes respectively. V_I and V_H can be obtained by the covalent–radius r_I and r_H of impurity and host atoms by $V_I = (4/3)\pi r_I^3$ and $V_I = (4/3)\pi r_H^3$ respectively.

The predicted maximum concentration using the assumption of Eq. 4.5 for various impurities in silicon are reported in Table 4.2. The theoretical values include the calculations of Narayan and Holland [Narayan & Holland 1982] and calculations performed in our work. We assumed a relaxed amorphous silicon and used $\Delta H_{ac} = 11.6$ kJ/mol [Donovan *et al.* 1985]

Table 4.2: Summary of theoretical and experimental maximum solubilities of various impurities in silicon during SPER. Theoretical data include the values computed by Narayan and Holland using the assumption given by Eq. 4.5 (see text for details) [Narayan & Holland 1982]. The theoretically predicted maximum concentration has also been computed in the frame of this work using the same equation and the corresponding values are reported. Experimental data are taken from the literature and experimental details can be found in associated references.

Species	Theory (at.cm^{-3})	Experiments (at.cm^{-3})
As	1.7×10^{22}[a]	9.0×10^{21}[a]
	4.2×10^{22}[b]	9.6×10^{21}[c]
Sb	3.0×10^{21}[a]	1.3×10^{21}[a]
	1.9×10^{21}[b]	6.4×10^{20}[c]
		1.3×10^{21}[d]
In	1.7×10^{21}[a]	5.5×10^{19}[a]
	1.1×10^{21}[b]	6.0×10^{19} (Estimation)[c]
Ga	6.0×10^{21}[a]	2.5×10^{19}[a]
	1.9×10^{22}[b]	5.5×10^{19} (Estimation)[c]
B	4.7×10^{21}[b]	6.5×10^{20}[e]
P	4.0×10^{22}[b]	$\gg 10^{21}$ (Estimation)[c]

[a]From [Narayan & Holland 1982]
[b]This work
[c]From [Duffy *et al.* 2006]
[d]From [Williams & Elliman 1982]
[e]From [Jain *et al.* 2004]

(see section 2.1.1). Bulk modulus values of considered impurities were taken from [Kittel 2005] and covalent radii from [Pyykkö & Atsumi 2009]. These values can be compared to experimental data taken from the literature. It should be admitted that the quantitative agreement between theory and experiments is not perfect, nevertheless there is a good qualitative agreement. We should point out that differences between theory and experiment may arise from various influencing factors. First of all, we have shown in section 2.1.1 that the crystallization enthalpy may vary over a significant range (see for example [Kail *et al.* 2011]). Then, in their model, Narayan and Holland only assumed an elastic contribution but it might be necessary to also include a chemical contribution [Alonso & Simozar 1980]. Alternatively, an approach based on first–principle calculation may be more appropriated as shown by Luo *et al.* for supersaturated solutions formed by molecular beam epitaxy (MBE) [Luo *et al.* 2003]. Finally, it is experimentally quite difficult to determine maximum solubility during SPER as evidenced by the differences between experimental results for a given dopant in Table 4.2.

We should emphasize that at the maximum impurity concentration, the regrowth front stops. Indeed, in section 2.1.1, we have shown that the regrowth velocity can be expressed as a product of a kinetic and a thermodynamical factor $v = v_{kinetic} \times v_{df}$ where the subscript df stands for "driving force" and corresponds to the thermodynamical factor. In the case of undoped Si SPER, the regrowth is kinetically driven and v_{df} can be dropped. However, in presence of dopants, the driving force term becomes important at high concentration and can be expressed as:

$$v_{df} = 1 - \exp\left(-\frac{\Delta H_{ac} - \Delta H_{strain}}{k_B T}\right). \tag{4.7}$$

From Eq. 4.7, it turns out that at the maximum impurity concentration achievable during SPER, $v_{df} = 0$. In other words the regrowth front does not advance anymore because the transition is not thermodynamically favorable. Actually, the presence of impurities during SPER gives rise

to various correlated effects on the regrowth kinetics that will be addressed in section 4.1.2.

Interestingly it seems that there is also an orientation–dependence of dopant activation. Indeed, Nishi *et al.* compared dopant activation of arsenic–implanted samples in (100), (110) and (111) silicon [Nishi *et al.* 1978]. They observed an almost complete activation in Si(100) but a lower one in Si(110) and Si(111) corresponding to 0.83 $\pm$ 0.04 and 0.66 $\pm$ 0.04 of the dopant fraction respectively.

4.1.2 Impurity–related mechanisms during SPER

It has been shown that the presence of impurities has a strong influence on SPER kinetics. In particular, the regrowth velocity exhibits an impurity–dependent behavior. On the other hand, impurity segregation at the α/c interface has been also observed resulting in a redistribution of the impurity profile towards the surface. This mechanism is often referred as snowplow in the literature. In this section, we will present a brief review of the impurity–dependent regrowth rate (section 4.1.2.1) and of the impurity redistribution during SPER (section 4.1.2.2).

4.1.2.1 Impurity–dependent regrowth velocity

From a thermodynamical point of view, the presence of an impurity during the amorphous to crystalline transition should result in a lower crystallization free–energy and therefore a slower regrowth velocity. In particular, as it has been shown in section 4.1.1.2, the α/c interface will stop at the maximum solubility (*i.e.* when there is no gain in free-energy to incorporate an impurity). However, it appears important to distinguish among dopants and other impurities because they lead to an opposed behavior as we shall show in this section.

Non–dopant impurities. The presence of non–dopant impurities has been reported to cause a retardation of the regrowth velocity. In particular, Narayan has evidenced that the presence of C, O or N in the amorphous phase results in a slower regrowth velocity and the development of microtwins during SPER in Si(100) [Narayan 1982]. Similarly Olson and Roth observed a retardation of the regrowth velocity with F [Olson & Roth 1988]. An interesting case occurs for H, which also causes a velocity retardation but also diffuses in the amorphous phase with a similar activation energy than for SPER ($\approx$ 2.7 eV) [Johnson *et al.* 2009]. It has been been postulated that H diffuses in α–Si and segregates at the α/c interface causing a retardation velocity. In an atomistic point of view, H may fix to dangling bonds that are suspected to be the SPER controlling defects [Spaepen & Turnbull 1979]. Technologically, such impurities may be present either intentionally or not. For example, species such as C or F are often used for co–doping in order to limit the diffusion of fast–diffusing species. In contrast H, O, N contamination may arise at different stages of the fabrication process.

An other interesting case is the SPER of SiGe which exhibits an enhanced regrowth rate with Ge content but (i) an increase of the activation energy for Ge content between 5 and 40 at.% with respect to pure silicon and (ii) a lower activation for higher Ge content up to $\approx$ 2.2 eV for pure germanium. This behavior has been observed by Haynes *et al.* in unstrained SiGe layer using *in–situ* Time Resolved Reflectivity (TRR) as shown in Fig. 4.2 [Haynes *et al.* 1995].

Dopant impurities. In contrast to non–dopant impurities, both n– and p–doped Si exhibits an enhancement of the regrowth velocity for concentrations lower than a critical concentration [Olson & Roth 1988]. However, the simultaneous presence of both n– and p–type impurities

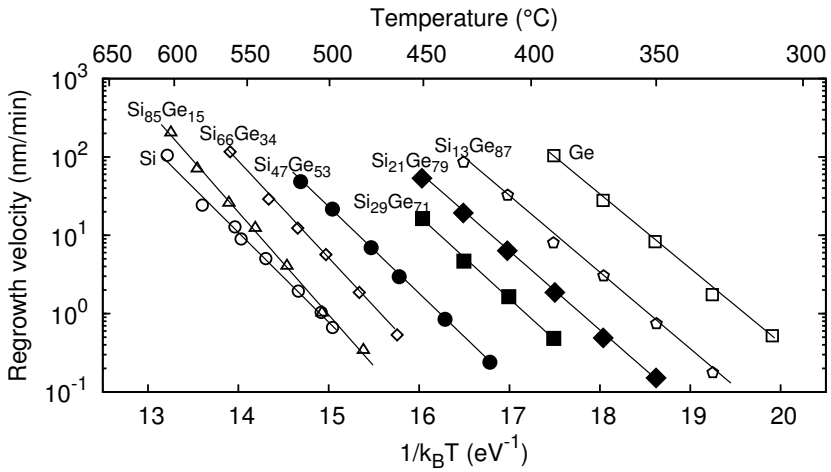

Figure 4.2: Experimental observations of the regrowth rate in unstrained SiGe for different Ge contents from [Haynes *et al.* 1995].

have been shown to have a compensating effect on the regrowth rate. This suggest an electrostatic effect on the SPER kinetics which has given rise to the development of various models to explain the influence of electrically active dopants on the regrowth velocity. A good review has been carried out by Lu *et al.* who examined their validity in terms of the involved physical mechanisms [Lu *et al.* 1991]. It turns out that the generalized Fermi–level shifting (GFLS) model introduced by Williams and Elliman can correctly account for the dopant–enhanced SPER observed experimentally [Williams & Elliman 1983]. Recently, Johnson *et al.* performed measurements of regrowth velocity using *in–situ* TRR in buried amorphous layers containing constant concentration dopant profiles at temperatures in the range 460–660 °C. In particular, the use of deep buried amorphous layer allows to get data that are not influenced by the eventual presence of H. Based on these data, they used the GFLS model to compute the dopant–enhanced regrowth rates [Johnson & McCallum 2007, Johnson *et al.* 2012]. In our work, we also used the GFLS model within an analytical model similarly to the approach of Johnson *et al.* and then in the frame of the LKMC SPER model. The obtained results will be presented in sections 4.2.1 and 4.2.2, respectively.

At high–dopant concentrations, the regrowth rate has been shown to start decreasing starting from a critical concentration which is dopant–dependent [Olson & Roth 1988]. This suggests that the dopant–dependent SPER kinetics is the result of a competition between electrostatic and thermodynamical effects. Indeed, in highly doped samples, the Fermi–level is pinned to the conduction or valence band–edge which should limit the enhancement of the regrowth velocity while the incorporation of a dopant atom implies an energetic cost which increases with dopant concentration as discussed in section 4.1.1.2. The reduction of the regrowth velocity has also been shown to be correlated with a segregation of impurities at the moving α/c interface resulting in a redistribution of the doping profile towards the surface that we will briefly present in the next section [Duffy *et al.* 2005, Demenev *et al.* 2012]. Nevertheless, the physical mechanisms involved during SPER of highly–doped remain quite unclear. In particular, there is, to date, no model accounting for the synergy between regrowth velocity and dopant segregation at the α/c interface.

4.1.2.2 Impurity redistribution

As we mentioned in the previous section, a redistribution of the dopant profile towards the surface can take place during SPER. This situation typically occurs at high concentration and corresponds to the dopant segregation at the moving α/c interface. Various authors have reported that the segregation at the α/c interface begins when the dopant concentration exceeds its solid solubility in crystalline silicon [Duffy *et al.* 2005, Simoen *et al.* 2009]. However, there is no particular reason to believe that there is a direct relation between solid solubility plays and the threshold at which dopant atoms begin to be redistributed during the solid–solid amorphous to crystalline transition.

The impact of dopant redistribution on the concentration profile is illustrated schematically in Fig. 4.3. After SPER, the initial dopant profile (Fig. 4.3a) is shifted towards the surface and a fraction of the dose is redistributed (Fig. 4.3b). Interestingly, experimental observations show a higher dopant redistribution along $\langle 111 \rangle$ than $\langle 100 \rangle$ direction [Williams & Elliman 1981].

Several continuum models have been proposed to account for the dopant segregation at the α/c interface based on a phase–field equation [Zechner *et al.* 2004] or a segregation model [Suzuki *et al.* 2007]. In the Synopsys SProcess KMC simulator, a simple model is also implemented by introducing a probability to deposit the considered impurity in the recrystallized area [Zographos & Martin-Bragado 2008]. However, as we mentioned in the previous section, none of these models treat dopant redistribution and regrowth kinetics in a consistent way.

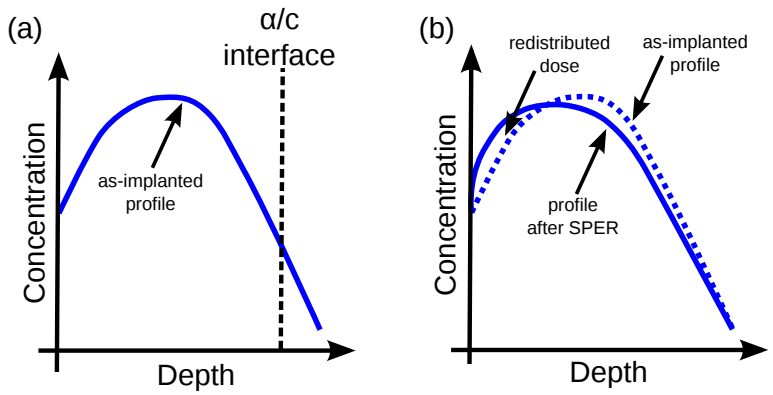

Figure 4.3: Schematic representation of the concentration profile (a) after ion–implantation and (b) after SPER. During SPER, a fraction of the implanted profile is redistributed towards the surface because of dopant segregation at the α/c interface.

4.2 Dopant–enhanced regrowth velocity

4.2.1 Analytical modeling

In this section, we present an analytical modeling of dopant–enhanced SPER based on the generalized Fermi level shifting (GFLS) model [Williams & Elliman 1983, Lu *et al.* 1991, Johnson & McCallum 2007, Johnson *et al.* 2012]. This model will then be used as a correction of the regrowth rates in the LKMC SPER model as we shall show in next section. In this work, only As and B have been considered.

The idea of the GFLS model is that SPER takes place via a defect existing in a neutral charge state X^0 but also its negatively and positively charged counterparts X^- and X^+ re-

spectively. The regrowth rate in intrinsic and doped conditions is then given by:

$$v_i = v_0 \times \left([X^0] + [X^-]\big|_i + [X^+]\big|_i \right) \tag{4.8}$$

and

$$v_d = v_0 \times \left([X^0] + [X^-]\big|_d + [X^+]\big|_d \right) \tag{4.9}$$

respectively, where v_0 is a constant. Assuming that the concentration of neutral defects is the same for doped or intrinsic material:

$$\frac{v_d}{v_i} = \frac{1 + \left.\dfrac{[X^-]}{[X^0]}\right|_d + \left.\dfrac{[X^+]}{[X^0]}\right|_d}{1 + \left.\dfrac{[X^-]}{[X^0]}\right|_i + \left.\dfrac{[X^+]}{[X^0]}\right|_i}. \tag{4.10}$$

In the general case, the ratio concentrations of a defect in charge states j and $j+1$ is given by Fermi-Dirac statistics:

$$\frac{[X^j]}{[X^{j+1}]} = \frac{g^j}{g^{j+1}} \times \exp\left(\frac{e_F - e(j+1, j)}{k_B T} \right) \tag{4.11}$$

where g is the defect level degeneracy, $e(j+1, j)$ is the energy level associated with the charge transition and $k_B T$ has the usual meaning. Hence:

$$\frac{[X^+]}{[X^0]} = \frac{g^+}{g^0} \times \exp\left(\frac{e(+, 0) - e_F}{k_B T} \right) \tag{4.12}$$

and

$$\frac{[X^-]}{[X^0]} = \frac{g^-}{g^0} \times \exp\left(\frac{e_F - e(0, -)}{k_B T} \right). \tag{4.13}$$

To compute the velocity ratio given by Eq. 4.10, it is necessary to determine e_F. This can be done by solving self–consistently the charge balance equation:

$$n_e - n_h + \sum_i Q_i [N_i^Q] = 0 \tag{4.14}$$

where n_e and n_h are electron and hole concentrations and $[N_i^Q]$ are ionized dopants of charge Q. Using degenerate semiconductor statistics:

$$n_e = N_C \mathcal{F}_{1/2} \left(\frac{e_F - e_C}{k_B T} \right) \tag{4.15}$$

and

$$n_h = N_V \mathcal{F}_{1/2} \left(\frac{e_V - e_F}{k_B T} \right) \tag{4.16}$$

where e_C and e_V are conduction and valence band edges respectively, $\mathcal{F}_{1/2}$ is the Fermi integral of order one–half[1] and N_C and N_V are the effective density of states in conduction and valence band respectively given by:

$$N_C = 2 \left(\frac{2\pi m_e^* k_B T}{h^2} \right)^{3/2} \tag{4.17}$$

[1] Notice that $\mathcal{F}_{1/2} \equiv (2/\sqrt{\pi}) F_{1/2}$ [Kim & Lundstrom 2008].

and

$$N_V = 2\left(\frac{2\pi m_h^* k_B T}{h^2}\right)^{3/2} \tag{4.18}$$

where h is Planck constant and m_e^* and m_h^* are electron and holes effective mass respectively. In this work we used the expressions of effective masses given in [Green 1990]:

$$m_e^* = 6^{2/3}\left(m_t^{*2} m_l^*\right)^{1/3} \tag{4.19}$$

and

$$m_h^* = m_0\left(\frac{a + bT + cT^2 + dT^3 + eT^4}{1 + fT + gT^2 + hT^3 + iT^4}\right)^{2/3} \tag{4.20}$$

where $m_t = 0.1905 m_0$ and $m_l = 0.9163 m_0$ are the longitudinal and transverse effective masses associated with the ellipsoidal constant energy surfaces and m_0 is the electron mass. The polynomial expression used for m_h^* is taken from [Lang *et al.* 1983] and the values of the different parameters are summarized in Table 4.3. We followed the assumption of Johnson *et al.* who considered that the fraction of ionized dopants is given by the Fermi–Dirac weighting function. For ionized donor $[N_d^+]$ and acceptor $[N_a^-]$ concentrations it yields:

Table 4.3: Values of the parameters of Eq. 4.20 from [Lang *et al.* 1983].

Parameter	Value
a	0.4435870
b	0.3609528×10^{-2}
c	0.1173515×10^{-3}
d	0.1263218×10^{-5}
e	0.3025581×10^{-8}
f	0.4683382×10^{-2}
g	0.2286895×10^{-3}
h	0.7469271×10^{-6}
i	0.1727481×10^{-8}

$$[N_d^+] = \frac{[N_d]}{g_d \exp\left[\beta(e_f - e_d)\right] + 1} \tag{4.21}$$

$$[N_a^-] = \frac{[N_a]}{g_a \exp\left[\beta(e_a - e_f)\right] + 1} \tag{4.22}$$

where a and d indices refer to "acceptor" and "donor" respectively and $\beta \equiv 1/k_B T$ is the inverse of the thermal energy, g is the shallow energy level degeneracy e_d and e_a are donor and acceptor energy level with respect to conduction minimum band edge and valence maximum band edge respectively; $[N_d]$ and $[N_a]$ are donor and acceptor dopant concentrations. Energy level degeneracies are such that $g_d = 2$ and $g_a = 4$ and the energy levels for As and B in Si at 300 K are $e_c - 54$ meV and $e_v + 45$ meV, respectively.

The band–gap of Si e_g exhibits a temperature dependence that should be taken into account. We used the band–gap narrowing model of Varshni with the parameters of Alex *et al.* [Alex *et al.* 1996] yielding:

$$e_g = e_0 - \frac{\alpha T^2}{T + \beta} \tag{4.23}$$

where $e_0 = 1.1692$ eV is the energy gap at 0 K, T is the temperature and $\alpha = 4.9 \times 10^{-4}$ eV.K^{-1} and $\beta = 655$ K. We also assumed a linear temperature dependence of the energy levels (which are given at 300 K in the manuscript) following $e_g(T)/e_g(300\text{ K})$.

Finally, Eq. 4.14 is solved numerically in a self–consistent way using Newton's iterative method for each temperature and concentration considered. It implies calculating the derivatives of Eq. 4.15, 4.16, 4.21 and 4.22 at each iteration step[2].

Table 4.4: Defects energy levels (at 300 K) and degeneracies used to compute the charged fraction of defects in Eq. 4.10. Values from [Johnson & McCallum 2007, Johnson *et al.* 2012] are also reported.

Reference	g^-	$e_C - e(0,-)$	g^+	$e_V + e(+,0)$
This work	$1/2$	0.2 eV	$3/2$	0.26 eV
[Johnson & McCallum 2007]	0.53 ± 0.07	0.16 ± 0.01 eV	1.5 ± 0.2	0.17 ± 0.01 eV
[Johnson *et al.* 2012]	$1/2$	0.118 ± 0.009 eV	1	0.149 ± 0.009 eV

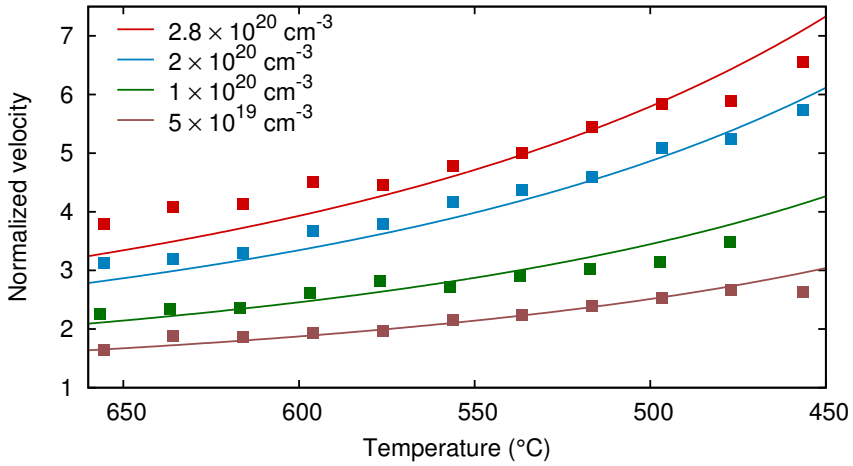

Figure 4.4: Normalized regrowth velocity as a function of temperature for different As concentrations. Theoretical results (lines) given by Eq. 4.10 with the parameters in Table 4.4 are compared with experimental data (symbols) from [Johnson & McCallum 2007].

Eq. 4.10 is used to predict the regrowth rate enhancement factor for different dopant concentrations as a function of the temperature. The results are plotted in Fig. 4.4 and 4.5 for As and B respectively and compared with experimental data of Johnson and McCallum [Johnson & McCallum 2007]. The values of the defect energy levels and degeneracy are reported in Table 4.4. The agreement of theoretical predictions with experimental data is quite good. Interestingly, the energy levels used in this work are slightly different than those obtained by Johnson *et al.* in either [Johnson & McCallum 2007] or [Johnson *et al.* 2012]. This can arise from the fact that Johnson *et al.* do not consider a temperature dependence of the energy level while we do. On the other hand, in [Johnson *et al.* 2012] they add a contribution of the strain created by substitutional impurities based on the model of Aziz *et al.* (see [Aziz *et al.* 1991]) and use extrinsinc semiconductor statistics in order to get a more "unified" model than in [Johnson & McCallum 2007]. However, their approach lacks of physical basis which can lead to inconsistencies. On one hand, extrinsinc semiconductor statistics should not be used in the concentration range they are considering. On the other hand, the strain term

[2]Note that $\partial \mathcal{F}_{1/2}(x)/\partial x = \mathcal{F}_{-1/2}(x)$

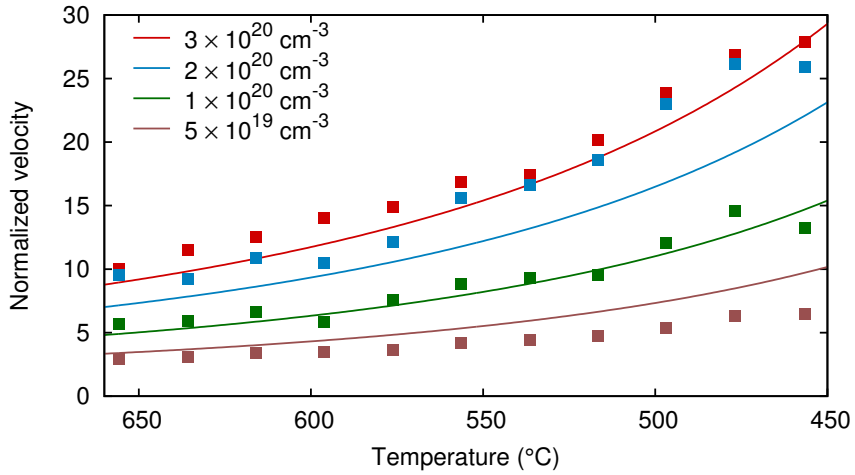

Figure 4.5: Normalized regrowth velocity as a function of temperature for different B concentrations. Theoretical results (lines) given by Eq. 4.10 with the parameters in Table 4.4 are compared with experimental data (symbols) from [Johnson & McCallum 2007].

is not consistent with recent experimental data of Rudawski *et al.* (see [Rudawski 2008]) as discussed in chapter 3.

The formulation we are using in this work is more general since it can be used for both n– and p–type dopants. Nevertheless, it also cannot explain the velocity differences between species of the same type at a given concentration that have been observed experimentally [D'Angelo *et al.* 2008, Johnson & McCallum 2007, Johnson *et al.* 2012].

Finally, we should point out that in our calculation the Fermi level is pinned to the crystalline value. However, band bending should exist between amorphous and crystalline phases. This would change the values of the defect energy levels we obtained in table 4.4 but would require assumptions about the Fermi level position at the α/c interface [Williams & Elliman 1983, Johnson & McCallum 2007]. In this work we have relaxed this assumption in the frame of the LKMC SPER model by coupling it with a three–dimensional Poisson solver as it will be shown in the following.

4.2.2 Atomistic LKMC modeling

In the previous section, we have presented the physical background of the generalized Fermi level shifting (GFLS) model. We have also shown the results of the analytical GFLS model by solving numerically the charge neutrality equation to determine the Fermi level position using degenerate semiconductor statistics. The good agreement of theoretical predictions with experimental data suggests that the first order dependence of enhanced regrowth velocity is correctly captured by the GFLS model. In this section, we introduce the GFLS correction into the regrowth rates used in the SPER LKMC model. We, again consider dopant–enhanced SPER upon the presence of As and B dopants.

4.2.2.1 Electrostatic calculation

The main difference existing between the analytical formulation presented in the previous section and the atomistic modeling arises from the fact that in the latter case it is necessary to consider the three–dimensional nature of the problem. It involves determining the electrostatic potential over the whole simulation domain. Martin–Bragado *et al.* proposed a resolution re-

lying on the charge neutrality assumption in order to model Fermi–level effects of species diffusing in silicon [Martin-Bragado *et al.* 2005a, Martin-Bragado *et al.* 2005b]. However, it turns out that their approach require to perform a charge smoothing instead of solving the Poisson's equation in order to be physically consistent. This approach allows to limit the computational cost but can give rise to differences with respect to the exact electrostatic solution in regions where abrupt band bending occurs or when dealing with heterojunctions. In this work, we use the semi–classical electrostatic potential by solving self–consistently the non–linear Thomas–Fermi approximation for carrier densities with Poisson's equation:

$$\varepsilon(x,y,z)\boldsymbol{\Delta}V(x,y,z) = -4\pi\left[\rho_{TF}(x,y,z) + \sum_i Q_i[N_i^Q]\right] \tag{4.24}$$

where V is the electrostatic potential, $\boldsymbol{\Delta}$ is the Laplacian, ε is the dielectric constant, $[N_i^Q]$ is the density of ionized dopants i of charge Q and ρ_{TF} is the carriers density given by:

$$\rho_{TF}(x,y,z) = N_C\mathcal{F}_{1/2}\left[\beta\left(e_F - e_C\right)\right] - N_V\mathcal{F}_{1/2}\left[\beta\left(e_V - e_F\right)\right] \tag{4.25}$$

where N_C and N_V are the effective density of states in conduction and valence bands respectively, e_F, e_C and e_V are the Fermi level, minimum conduction band edge and maximum valence band edge and $\beta \equiv 1/k_BT$. The expressions of N_C and N_V are given by Eq. 4.17 and 4.18, respectively. In Eq. 4.25, we fix $e_F = 0$ yielding:

$$e_F - e_C = -\frac{e_g}{2} + V \tag{4.26}$$

and

$$e_V - e_F = -\frac{e_g}{2} - V. \tag{4.27}$$

where e_g is the bandgap given by Eq. 4.23. The details of the solver of Eq. 4.24 are presented in appendix B. At the dopant concentrations considered in this work ($> 10^{19}$ at.cm^{-3}), the dopant shallow levels are merged with conduction or valence band because of metal/insulator transition [Dai *et al.* 1992]. We therefore assume that all dopants are ionized, *i.e.* $[N_i^Q] = [N_i]$, in contrast to the previous section.

4.2.2.2 LKMC model

During the α/c transition, dopants are incorporated into the crystalline lattice and become electrically active. In the LKMC model, we consider that (i) dopants in substitutional position in the crystalline phase are ionized and (ii) dopants in the amorphous phase are electrically inactive. When an *amorphous* element of the grid becomes *crystalline*, the dopant species present in this element become "substitutional". We do not take into account the fact that the dopants can segregate at the α/c interface leading to a redistribution of the implanted profile towards the surface as shown schematically in Fig. 4.3. Dopant atoms could presumably interact with each other or with point defects present in the simulation cell using the OKMC module giving rise to diffusion or clustering. Even if the implementation of the code permits it, we did not allow any interaction in the presented calculations.

The LKMC model includes the electrostatic–dependence by modifying the transition frequency given by Eq. 3.16 as:

$$\nu(n,\boldsymbol{\sigma},V,T) = \nu_{GFLS}(V) \times K(n) \times \exp\left(-\frac{E^* + \boldsymbol{\Delta V}^*\boldsymbol{\sigma}}{k_BT}\right). \tag{4.28}$$

where $\nu_{GFLS}(V)$ is the electrostatic correction relying on GFLS model, given by Eq. 4.10. We should emphasize that the model allows *per se* to take into account the influence of stress arising from the incorporation of a dopant through the activation strain tensor $\boldsymbol{\Delta V}^*$, as shown in chapter 3. However, it has not been included in the calculation since stress are expected to be too small to have a significant impact for the concentrations considered.

Another important aspect of the problem is how the electrostatic potential is updated. Indeed, we should theoretically update it each time an element becomes crystalline since it involves a change in the distribution of ionized species. However this option represents a very high computational cost and has only been used for calibration purposes. Instead, the Poisson solver is only called every n events using the solution of the previous step in order to minimize the overhead. We obtained converged results for $n = 5 \times 10^4$ events with respect to a reference corresponding to an update everytime an element becomes crystalline; this scheme leads to a strong improvement of the computational time.

4.2.2.3 Results

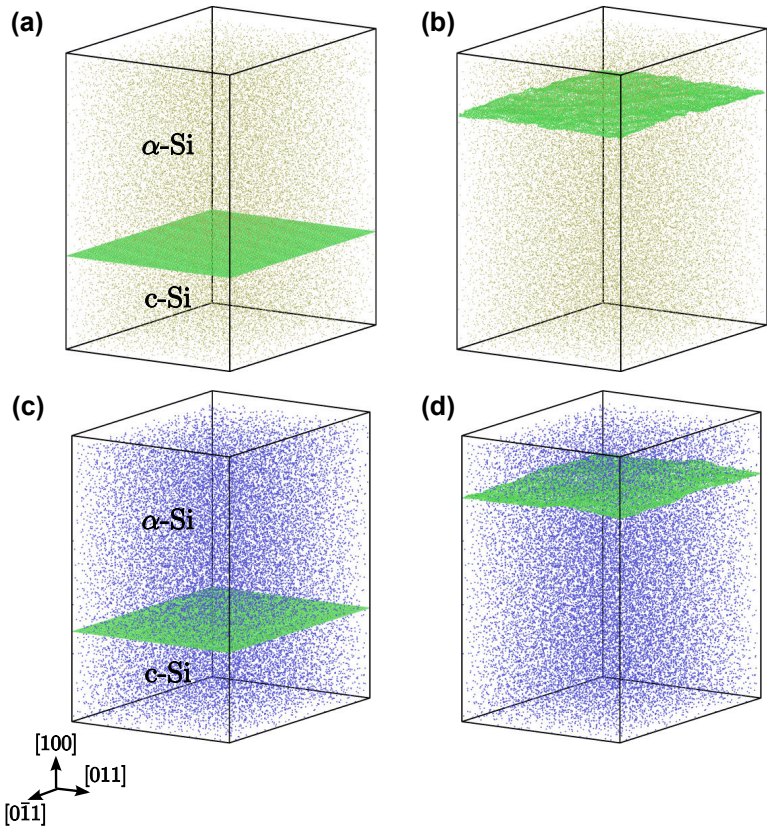

Figure 4.6: Snapshots of the simulation cells used for LKMC simulations of SPER upon the presence of dopants. (a) initial structure containing a 3×10^{20} at/cm^3 B constant concentration and (b) after SPER of $\sim$ 30 nm α–Si at 550 °C. (c) initial structure containing a 2.8×10^{20} at/cm^3 As constant concentration and (d) after SPER of $\sim$ 30 nm α–Si at 550 °C.

The LKMC model has been used to study the evolution of the α/c interface upon the presence of As or B during SPER of Si(100). For these studies, a $60 \times 50\sqrt{2}a_0 \times 50\sqrt{2}a_0$ nm^3 simulation cell has been considered, where a_0 is the basic unit cell length (0.5431 nm). The simulation domain was bonded by two $\{001\}$ planes along x direction and four $\{011\}$ planes along y and z directions. A 40 nm thick amorphous layer with an atomically flat α/c interface

has been recrystallized. SPER proceeds along $\langle 100 \rangle$ direction and periodic boundary conditions (PBC) are applied in the $\langle 110 \rangle$ lateral directions. As or B atoms were inserted randomly in the simulation cell in order to form a constant profile concentration. Fig 4.6a and 4.6c show the initial simulation cell for a 3×10^{20} at.cm^{-3} B and a 2.8×10^{20} at.cm^{-3} As constant concentration over the whole simulation domain respectively.

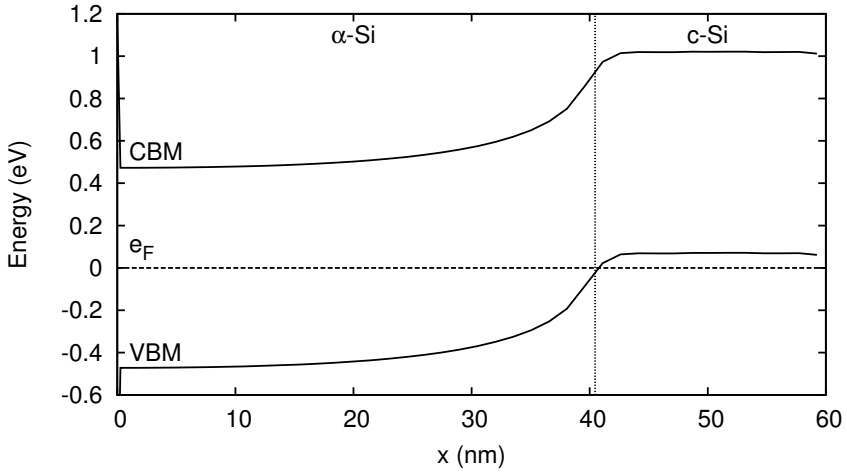

(a)

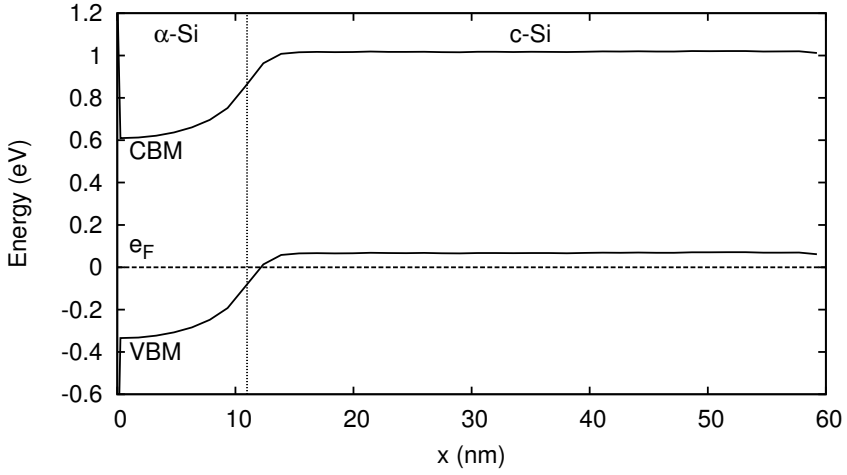

(b)

Figure 4.7: Band structure at the α/c interface for a 3×10^{20} at/cm^3 B concentration at 550 °C: (a) initial structure and (b) after the regrowth of $\sim$ 30 nm.

Poisson's equation is solved using PBC along y and z and Newman boundary conditions along x direction and the solver is called every 5×10^4 events. The evolution of the α/c interface is monitored using the method described in appendix A and is used to compute the averaged regrowth velocity v_d. A reference simulation cell with no dopants inside is used to compute the averaged regrowth velocity in intrinsic Si and for each simulation point the normalized regrowth velocity is calculated as v_d/v_i. Fig. 4.7 show the band structure of the simulation cell along the x direction for a 3×10^{20} at/cm^3 B concentration at the beginning of the simulation (Fig. 4.7a) and after SPER of $\sim$ 30 nm α–Si at 550 °C (4.7b). Similarly, Fig. 4.8a and 4.8b show the band structure for a 2.8×10^{20} at/cm^3 As concentration. It highlights the fact that band bending between the amorphous and crystalline phases is taken into account in the atomistic implementation, in contrast to the analytical model discussed in previous section.

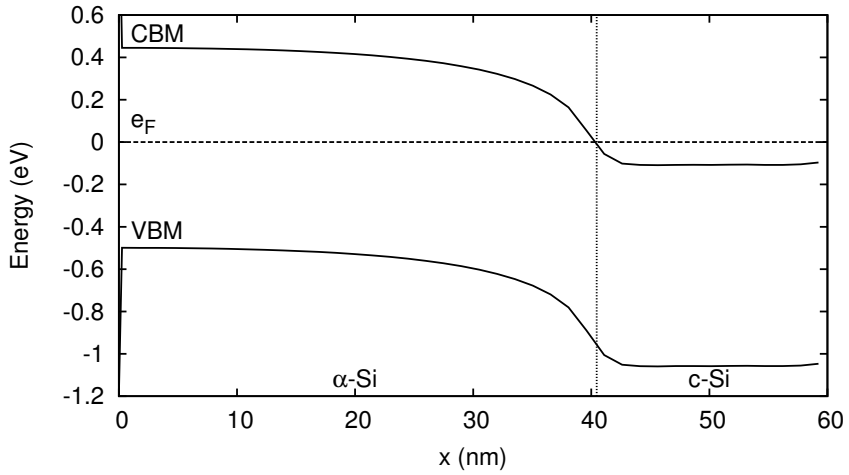

(a)

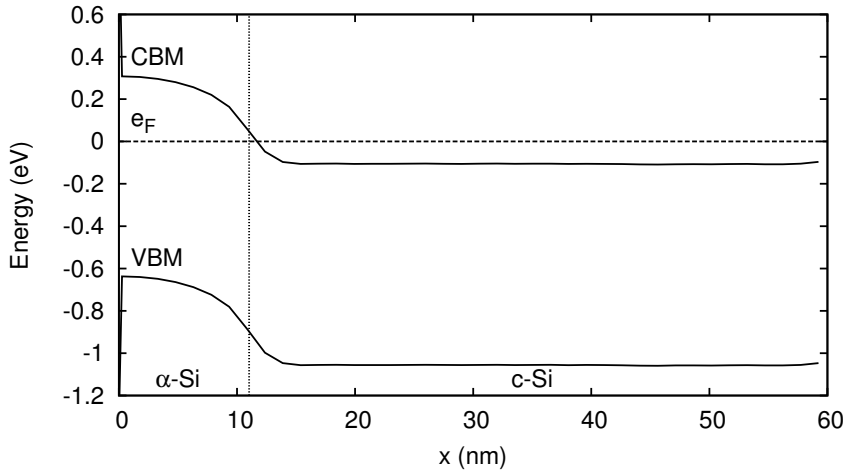

(b)

Figure 4.8: Band structure at the α/c interface for a 2.8×10^{20} at/cm^3 As concentration at 550 °C: (a) initial structure and (b) after the regrowth of $\sim$ 30 nm.

However, we should point out that (i) we used the same parameters of the band structure for α–Si as those for c–Si and (ii) the presence of charged defects at the α/c interface is not introduced in the right hand side of Eq. 4.28 so that the calculation is not fully self–consistent. Unfortunately details of the band structure of α–Si formed by ion–implantation are very sparse which prevents us to use reliable data in our electrostatic calculation [Johnson & McCallum 2007, and references therein]. Nevertheless, because of band–bending, the energy levels used in our atomistic model are higher than those used in the analytical model (see table 4.4) and are summarized in Table 4.5.

Table 4.5: Defects energy levels (at 300 K) and degeneracies used to compute the charged fraction of defects (see Eq. 4.12 and 4.13) in Eq. 4.10.

g^-	$e_C - e(0,-)$	g^+	$e_V + e(+,0)$
$1/2$	0.31 eV	$3/2$	0.36 eV

Fig. 4.9 and 4.10 show the normalized regrowth velocity predicted by the LKMC model (lines) as a function of temperature for B and As concentrations ranging from 5×10^{19} to $3 \times$

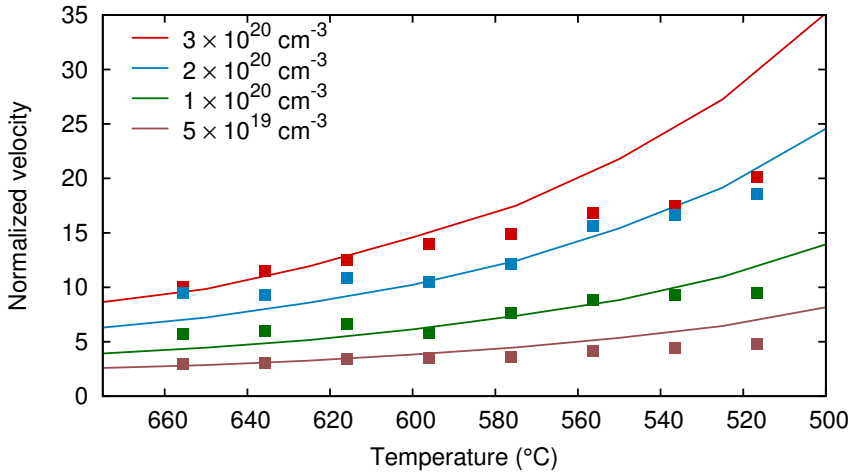

Figure 4.9: Normalized SPER velocity as a function of temperature for different B concentrations. Simulations results (lines) are compared with experimental data (symbols) from [Johnson & McCallum 2007].

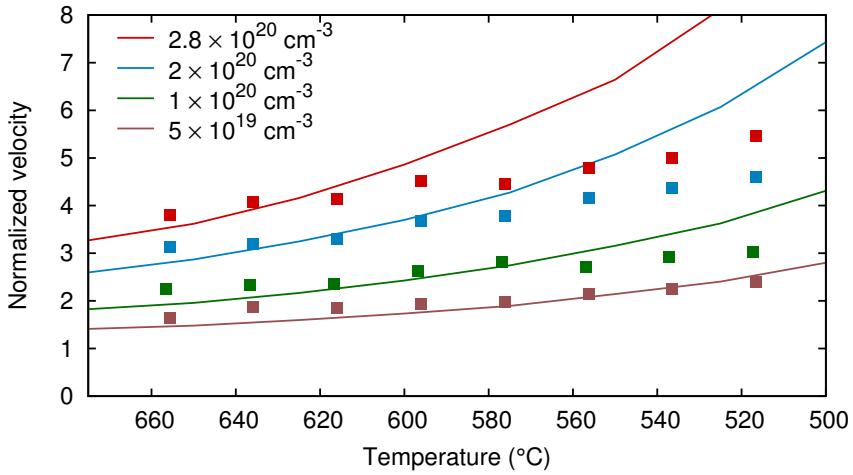

Figure 4.10: Normalized SPER velocity as a function of temperature for different As concentrations. Simulations results (lines) are compared with experimental data (symbols) from [Johnson & McCallum 2007].

10^{20} at/cm^3 and compared with experimental data taken from [Johnson & McCallum 2007]. Results predicted by the LKMC model are in relatively good agreement with experimental data even if some discrepancies appear for concentrations higher than 2×10^{20} at/cm^3. The origin of these differences is quite unclear and may arise because various factors relative to high concentration phenomena are not taken into account in our calculation: influence of the stress generated by substitutional impurities, clustering, segregation at the α/c interface. On the other hand, the influence of charged defects in the right hand side of the Poisson equation might be not negligible. Relaxing this assumption would be somewhat more demanding and would require further investigations. In particular, it becomes necessary to introduce LKMC information in the Poisson which is not straightforward.

4.3 Summary

In this chapter, we have discussed the concepts of solid solubility and metastable solubility. Solid solubility is a parameter which defines the maximum dopant concentration before form-

ing a precipitate phase in the solid at equilibrium. In contrast, metastable solubility is a kinetic quantity which corresponds, in the case of SPER, to the maximum dopant concentration that can be incorporated into the silicon lattice during recrystallization. In particular, it explains the fact that SPER allows to achieve dopant concentrations exceeding solid solubility. Both of these quantities are technologically relevant since they can be used to determine which species are suitable for a given application.

In presence of impurities, SPER exhibits various interesting behaviors. First of all, its velocity appears to be reduced with non–dopant impurities. In contrast, ionized dopants create an enhancement of the regrowth velocity until a critical concentration. This effect has been related to an electrostatic contribution suggesting the presence of charged defects at the α/c interface. However, beyond a critical concentration the regrowth velocity is reduced until the metastable solubility where the α/c interface is stopped because the amorphous to crystalline is not thermodynamically favorable. On the other hand, for various impurities, a segregation at the α/c has been observed and is correlated with the regrowth kinetics. This segregation phenomenon leads to the redistribution of dopant species towards the surface in a mechanism often referred as “snowplow”.

To take into account some of these mechanisms, the LKMC model has been extended to include an electrostatic dependence in the regrowth rates given by:

$$\nu = \nu_{intrinsic} \times \nu_{GFLS} \tag{4.29}$$

where $\nu_{intrinsic}$ is the intrinsic rate and ν_{GFLS} is the electrostatic–dependent correction based on the generalized Fermi level shifting model [Williams & Elliman 1983]. This model relies on the assumption that the relative position of the Fermi level with respect to minimum conduction band edge and maximum valence band edge gives rise to the formation of charged defects X^+ or X^-, while the concentration of neutral defects X^0 is the same as in the intrinsic material. The presence of these charged defects leads to an enhancement of ν and therefore of the regrowth velocity. This model requires to compute the electrostatic potential over the whole three–dimensional simulation domain and update it with the evolution of the α/c interface. This has been achieved by implementing a numerical solver of the Poisson’s equation self–consistently with the Thomas–Fermi approximation in a finite difference scheme. Simulation results of the normalized regrowth velocity in Si(100) doped with As or B at different concentrations show a relative good agreement with experimental data. Nevertheless some discrepancies exist at high concentration and further investigation are still required.

CHAPTER 5

Summary and suggestions for future work

Contents

In this manuscript, we explored the physical mechanisms involved in the recrystallization of silicon amorphized by ion–implantation through solid phase epitaxial regrowth (SPER). This technique is used to form junctions at low processing temperature in order to facilitate device scaling. Indeed, this process enables to achieve highly activated and abrupt junctions that are suitable for advanced devices. It is also used to fabricate top layer transistors in a 3D sequential integration scheme which has been emerging in recent years, in particular at CEA Leti [Batude *et al.* 2013]. The development of a comprehensive SPER model relying on lattice kinetic Monte Carlo (LKMC) method allowed us to study the regrowth kinetics upon the influence of different technologically relevant parameters. This model can also be successfully used to predict the evolution of the regrowth front in advanced silicon devices. In this chapter, we summarize the work achieved during this PhD (section 5.1), and conclude with suggestions for future work (section 5.2).

5.1 Summary

The work carried out during this PhD has been focused on the modeling of SPER relying on LKMC method including the influence of different parameters. The models have been implemented in the MMonCa simulator that has been recently created by Dr. Ignacio Martín–Bragado at IMDEA Materials. Our achievements are summarized in the following sections.

5.1.1 Regrowth anisotropy and regrowth–induced defects

To include the influence the of crystalline orientation on regrowth kinetics in order to account for regrowth anisotropy, the model distinguishes among microscopic configurations lying on a {100}, {110} or a {111} plane, depending on atoms at the α/c interface forming two undistorted bonds or needing one or two extra atoms to form them. For each configuration, the regrowth probability follows an Arrhenius law with a different prefactor. During this PhD, the model has been extended in order to account for the formation of twin defects on {111} planes [Martin-Bragado & Sklenard 2012]. Defective configurations are built on–the–fly when a {111} microscopic event occurs giving rise to better physical insight.

LKMC simulations have been carried out to simulate the regrowth velocity of single–directional SPER for different crystalline orientations. Comparison with experimental data from the literature allowed us to validate the developed model and its prediction capabilities. In particular, we studied the regrowth of Si(111) and explained the origin for the formation and subsequent evolution of different type of twins (parallel to the interface and inclined) and its implication in the overall evolution of Si(111) recrystallization.

On a more technologically relevant aspect, LKMC simulations have been carried out to analyze the regrowth kinetics of multi–directional SPER in the case of Si(100) substrates. We simulated the regrowth of $\langle 110 \rangle$–aligned structures and $\langle 100 \rangle$–aligned structures in Si(100) and observed the formation of $\{111\}$ and $\{110\}$ facets respectively. $\{111\}$ faceting produces defective regions because twin defects can be formed during the recrystallization of $\{111\}$ configurations while it is not the case with $\{110\}$ faceting. As a consequence, SPER of $\langle 100 \rangle$–aligned structures has been shown to succeed with a better crystalline quality in contrast to $\langle 110 \rangle$–aligned structures. In box–shaped amorphous regions, SPER proceeds through a lateral and a vertical regrowth front competing with each other. As for the regrowth of trench–bounded regions, simulations predict a better crystalline quality after SPER for $\langle 100 \rangle$–aligned box–shaped regions than for $\langle 110 \rangle$–aligned box–shaped regions, in good agreement with experimental observations. We observed this behavior in the regrowth of amorphized regions in FDSOI MOSFETs: $\langle 110 \rangle$–channel devices give rise to $\{111\}$ faceting and defects formation at the spacer edge while in $\langle 100 \rangle$–channel devices the regrowth is much less defective. This result may have important implications in the technological options in the formation of junctions with a low processing temperature.

5.1.2 Influence of stress

We improved the LKMC model to account for the impact of a non–hydrostatic stress field on microscopic regrowth rates using the concept of activation strain tensor introduced by Aziz *et al.* [Aziz *et al.* 1991]. In our stress model, we considered two different configuration–dependent activation strain tensors. This allowed us to reproduce recent experimental data of SPER velocity upon in–plane uniaxial stress [Sklenard *et al.* 2013a]. Such a distinction has important implications in the physical understanding of SPER microscopic mechanisms. Indeed, within this model, SPER is driven by a dual–timescale process rather than a single atomistic mechanism.

LKMC simulations of in–plane uniaxial stress showed that regrowth velocity is not affected by tensile stress while is is significantly reduced upon compressive stress up to -0.5 GPa. Interestingly, without extra parameters, observation of the morphological evolution of the α/c interface showed that the interface roughness is enhanced (reduced) with compressive (tensile) stress, in good agreement with experimental observations.

Finally we have shown that the model offers an unified treatment of the influence of non–hydrostatic stresses on SPER [Sklenard *et al.* 2014].

5.1.3 Influence of dopants

The role of dopants on the regrowth kinetics is probably one of the most complex phenomena to model. Indeed, dopants have been reported to cause an enhancement of the regrowth velocity. However, for several the species (*e.g.* P or As), the regrowth velocity happens to slow down at a certain doping concentration. This phenomenon seems to be related to the so–called snowplow effect where impurities move ahead of the α/c interface instead of being incorporated into substitutional positions in the crystalline phase. All these mechanisms appear to be

strongly correlated. In particular, dopant activation through SPER depends on the regrowth kinetics, and the regrowth kinetics depends on dopant activation.

In this manuscript, we have introduced an electrostatic contribution into the LKMC model in order to account for the presence of ionized dopants. This correction of the microscopic regrowth rates relies on the generalized Fermi–level shifting (GFLS) model proposed by Williams and Elliman [Williams & Elliman 1983]. A three–dimensional Poisson solver has been implemented in the MMonCa simulator and coupled to the LKMC module in order to compute the recrystallization probabilities. In our simulations, we assumed that all the dopants were incorporated into the crystalline lattice during the α/c transition and became electrically active. Despite this approximation we obtained a reasonable agreement with experimental data.

5.2 Suggestions for future work

In this PhD, we mainly focused on the description of SPER using the LKMC module of MMonCa, and dopants were assumed to be systemically incorporated in the silicon lattice. However, this approximation cannot apply to junction formation at low processing temperature in actual FDSOI devices where the situation is far more complicated. The work presented in chapter 4 has been carried out in order to improve the description of regrowth kinetics in presence of dopants and can be used as a basis to model the dopant redistribution during recrystallization (*i.e.* the snowplow effect). At the end of this PhD, some developments have been achieved to integrate this mechanism using a three–phase segregation model at the α/c interface but have not been included in this manuscript. As a consequence, further work could be done to correctly model dopant redistribution phenomena which are quite related with the incorporation of dopants in the crystalline lattice. In particular, a coupling between the LKMC and OKMC modules of MMonCa would be necessary and would give rise to the possibility of studying the evolution of incorporated dopants and their interactions with crystalline defects.

Another topic of interest that is also technologically relevant is the extension of the LKMC model to describe SPER in other materials. This has been recently carried out for germanium [Darby *et al.* 2013] but there is a growing interest in the study of SiGe alloys and III–V materials. The evolution of twin–defects upon further annealing and their eventual healing also remains an unsolved problem.

As shown in chapter 3, the stress model has been limited to the regrowth of {100} configurations. As a consequence, further work has to be carried out to expend it to {110} and {111} configuration in order to study the influence of stress during multi–directional regrowth. In particular, stress memorization techniques (SMT) relying on dislocations formation using SPER are being used in actual advanced devices to induce stress in the channel transistors in order to enhance the carriers' mobility. Such techniques could be, in principle, simulated with the LKMC model coupled to a mechanical solver.

Finally, the simulation of epitaxy (*i.e.* through a gas/solid transition) is becoming an important field of investigation that is in line with technological trends. Indeed, the process of future advanced CMOS devices rely on the use of:

- in–situ doped epitaxy to form source and drain regions without using ion implantation anymore,
- epitaxy of III–V materials to form transistor channel.

Such mechanisms could be simulated with the LKMC model as they are quite related to SPER.

APPENDIX A

Amorphous/Crystalline interface extraction

The extraction of the amorphous/crystalline (α/c) interface position is an important feature in order to be able to compare simulations with experimental results. As it has been discussed in chapter 2, lattice atoms located at the α/c interface are explicitly represented in the LKMC module. Each atom is defined by a set of coordinates (x, y, z) and a tag representing whether it is *amorphous* or *crystalline*. The coordinates correspond to the atomic positions for a perfect crystal structure. However, twin defects can be generated during the recrystallization of {111} configurations, giving rise to coordinates different than those for a perfect crystal structure. As a consequence, a second tag is used to distinguish among atoms that are *defective* or not. Fig. A.1 shows a simulation cell containing an α/c interface. Atoms in red are *crystalline* and those in green are *amorphous*.

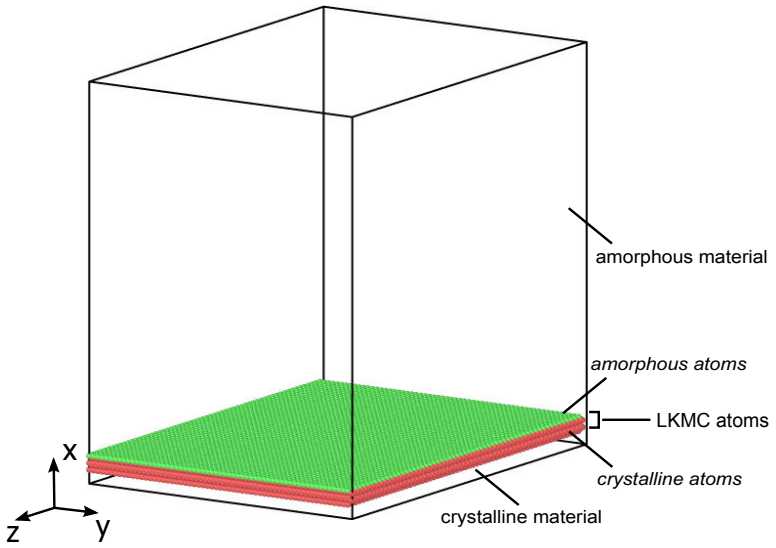

Figure A.1: Simulation cell containing an α/c interface. Atoms in red are *crystalline* and those in green are *amorphous*.

A.1 Interface position

To determine the α/c interface position, a list containing the coordinates of *crystalline* atoms having one or more *amorphous* first nearest neighbors is built. From this list, the mean values $\langle x \rangle$, $\langle y \rangle$ and $\langle z \rangle$ are calculated:

$$\langle x \rangle = \frac{1}{N} \sum_{i=1}^{N} x_i \tag{A.1}$$

$$\langle y \rangle = \frac{1}{N} \sum_{i=1}^{N} y_i \tag{A.2}$$

$$\langle z \rangle = \frac{1}{N} \sum_{i=1}^{N} z_i \tag{A.3}$$

with N being the total number of atoms in the list and x_i, y_i and z_i the values of the x, y and z coordinates for the atom i. In the case of Fig. A.1, the position of the α/c is given by $\langle x \rangle$.

A.2 Interface roughness

The interface roughness is obtained from the standard deviation of the atoms distribution at α/c interface (see section A.1), yielding:

$$\sigma_x = \sqrt{\frac{1}{N} \sum_{i=1}^{N} \left(x_i - \langle x \rangle\right)^2}, \tag{A.4}$$

$$\sigma_y = \sqrt{\frac{1}{N} \sum_{i=1}^{N} \left(y_i - \langle y \rangle\right)^2}, \tag{A.5}$$

and

$$\sigma_z = \sqrt{\frac{1}{N} \sum_{i=1}^{N} \left(z_i - \langle z \rangle\right)^2}. \tag{A.6}$$

In the case of Fig. A.1, the interface roughness $\sigma_{if} = \sigma_x$.

A.3 Interface velocity

The interface velocity is calculated from the α/c interface position (see section A.1) by a post–processing procedure. It is obtained by computing the time derivative of the averaged position, $\partial_t \langle x \rangle$, $\partial_t \langle y \rangle$ and $\partial_t \langle z \rangle$[1]. In the case of Fig. A.1, the interface instantaneous regrowth velocity is given by $\partial_t \langle x \rangle$.

We should point out that this calculation involves monitoring the evolution of the moving α/c interface positions. Typically, for a given regrowth condition, we save the α/c interface position every n events (n being a tunable parameter) and compute the averaged velocity $v = \langle \partial_t \langle x \rangle \rangle$.

[1] In this work, a backward difference form has been used to numerically compute the derivatives.

APPENDIX B

Numerical solution of the 3D Poisson equation

B.1 Linear Poisson equation

We consider a three-dimensional system where (x, y, z) are the cartesian coordindates of a point P. The charge density $\rho(x, y, z)$, the dielectric constant $\varepsilon(x, y, z)$ and therefore the electrostatic potential $V(x, y, z)$ at point P only depend of the x, y and z and the Poisson equation is given by:

$$\varepsilon(x, y, z)\boldsymbol{\Delta} V(x, y, z) = \boldsymbol{\nabla} \cdot [\varepsilon(x, y, z)\boldsymbol{\nabla} V(x, y, z)] = -4\pi\rho(x, y, z) \tag{B.1}$$

The electric field $\boldsymbol{E}(P)$ is by definition the gradient of the potential and can be written:

$$\boldsymbol{E}(P) = -\boldsymbol{\nabla} V(x, y, z) = E_x(x, y, z)\boldsymbol{x} + E_y(x, y, z)\boldsymbol{y} + E_z(x, y, z)\boldsymbol{z} \tag{B.2}$$

Considering the mesh shown Fig.B.1, we will use finite differences to compute partial derivatives appearing in Eq. B.1. The axis x, y and z are respectively divided in m intervals $[x_i, x_{i+1}]$, n intervals $[y_j, y_{j+1}]$ and p intervals $[z_k, z_{k+1}]$.

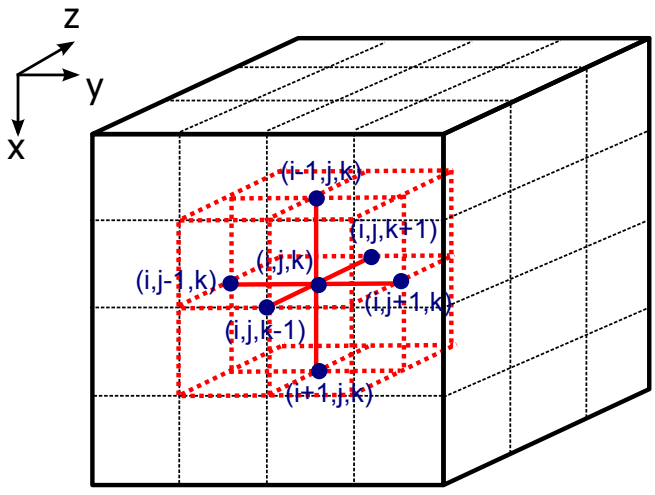

Figure B.1: Schematic representation of the three–dimensional domain mesh used by the Poisson solver in MMonCa.

Applying Gauss's law, we can write the electric flux from Eqs. B.1 and B.2:

$$\iiint \varepsilon(x, y, z)\boldsymbol{\nabla} \cdot \boldsymbol{E}(P)\, dP = \oiint_S \varepsilon(x, y, z)\boldsymbol{E}(P) \cdot d\boldsymbol{S}(P) = 4\pi Q_{ijk} \tag{B.3}$$

Then, upon the finite difference assumption, we obtain[1] from Eq. B.3:

$$
\begin{aligned}
&E_x(x_{i+\frac{1}{2}}, y_j, z_k)[\\
&\qquad \varepsilon_1 \left(y_{j+\frac{1}{2}} - y_j\right)\left(z_{k+\frac{1}{2}} - z_k\right) + \varepsilon_2 \left(y_j - y_{j-\frac{1}{2}}\right)\left(z_{k+\frac{1}{2}} - z_k\right) + \\
&\qquad \varepsilon_3 \left(y_{j+\frac{1}{2}} - y_j\right)\left(z_k - z_{k-\frac{1}{2}}\right) + \varepsilon_4 \left(y_j - y_{j-\frac{1}{2}}\right)\left(z_{k+\frac{1}{2}} - z_k\right)] \\
&-E_x(x_{i-\frac{1}{2}}, y_j, z_k)[\\
&\qquad \varepsilon_5 \left(y_{j+\frac{1}{2}} - y_j\right)\left(z_{k+\frac{1}{2}} - z_k\right) + \varepsilon_6 \left(y_j - y_{j-\frac{1}{2}}\right)\left(z_{k+\frac{1}{2}} - z_k\right) + \\
&\qquad \varepsilon_7 \left(y_{j+\frac{1}{2}} - y_j\right)\left(z_k - z_{k-\frac{1}{2}}\right) + \varepsilon_8 \left(y_j - y_{j-\frac{1}{2}}\right)\left(z_{k+\frac{1}{2}} - z_k\right)] \\
&+E_y(x_i, y_{j+\frac{1}{2}}, z_k)[\\
&\qquad \varepsilon_9 \left(x_{i+\frac{1}{2}} - x_i\right)\left(z_{k+\frac{1}{2}} - z_k\right) + \varepsilon_{10} \left(x_i - x_{i-\frac{1}{2}}\right)\left(z_{k+\frac{1}{2}} - z_k\right) + \\
&\qquad \varepsilon_{11} \left(x_{i+\frac{1}{2}} - x_i\right)\left(z_k - z_{k-\frac{1}{2}}\right) + \varepsilon_{12} \left(x_i - x_{i-\frac{1}{2}}\right)\left(z_{k+\frac{1}{2}} - z_k\right)] \\
&-E_y(x_i, y_{j-\frac{1}{2}}, z_k)[\\
&\qquad \varepsilon_{13} \left(x_{i+\frac{1}{2}} - x_i\right)\left(z_{k+\frac{1}{2}} - z_k\right) + \varepsilon_{14} \left(x_i - x_{i-\frac{1}{2}}\right)\left(z_{k+\frac{1}{2}} - z_k\right) + \\
&\qquad \varepsilon_{15} \left(x_{i+\frac{1}{2}} - x_i\right)\left(z_k - z_{k-\frac{1}{2}}\right) + \varepsilon_{16} \left(x_i - x_{i-\frac{1}{2}}\right)\left(z_{k+\frac{1}{2}} - z_k\right)] \\
&+E_z(x_i, y_j, z_{k+\frac{1}{2}})[\\
&\qquad \varepsilon_{17} \left(x_{i+\frac{1}{2}} - x_i\right)\left(y_{j+\frac{1}{2}} - y_j\right) + \varepsilon_{18} \left(x_i - x_{i-\frac{1}{2}}\right)\left(y_{j+\frac{1}{2}} - y_j\right) + \\
&\qquad \varepsilon_{19} \left(x_{i+\frac{1}{2}} - x_i\right)\left(y_j - y_{j-\frac{1}{2}}\right) + \varepsilon_{20} \left(x_i - x_{i-\frac{1}{2}}\right)\left(y_{j+\frac{1}{2}} - y_j\right)] \\
&-E_z(x_i, y_j, z_{k-\frac{1}{2}})[\\
&\qquad \varepsilon_{21} \left(x_{i+\frac{1}{2}} - x_i\right)\left(y_{j+\frac{1}{2}} - y_j\right) + \varepsilon_{22} \left(x_i - x_{i-\frac{1}{2}}\right)\left(y_{j+\frac{1}{2}} - y_j\right) + \\
&\qquad \varepsilon_{23} \left(x_{i+\frac{1}{2}} - x_i\right)\left(y_j - y_{j-\frac{1}{2}}\right) + \varepsilon_{24} \left(x_i - x_{i-\frac{1}{2}}\right)\left(y_{j+\frac{1}{2}} - y_j\right)] \\
&\quad = 4\pi Q_{ijk}
\end{aligned}
\tag{B.4}
$$

where

$$x_{i+\frac{1}{2}} = \frac{1}{2}\left(x_i + x_{i+1}\right) \qquad x_{i-\frac{1}{2}} = \frac{1}{2}\left(x_i + x_{i-1}\right) \tag{B.5}$$

$$y_{j+\frac{1}{2}} = \frac{1}{2}\left(y_j + y_{j+1}\right) \qquad y_{j-\frac{1}{2}} = \frac{1}{2}\left(y_j + y_{j-1}\right) \tag{B.6}$$

$$z_{k+\frac{1}{2}} = \frac{1}{2}\left(z_k + z_{k+1}\right) \qquad z_{k-\frac{1}{2}} = \frac{1}{2}\left(z_k + z_{k-1}\right) \tag{B.7}$$

The electric field on each segment is defined as:

$$E_x(x_{i+\frac{1}{2}}, y_j, z_k) = -\frac{V_{i+1jk} - V_{ijk}}{dx_i} \qquad E_x(x_{i-\frac{1}{2}}, y_j, z_k) = -\frac{V_{ijk} - V_{i-1jk}}{dx_{i-1}} \tag{B.8}$$

[1] We have chosen to split each surface in four different dielectric constants to account for the fact we can have different materials.

$$E_y(x_i, y_{j+\frac{1}{2}}, z_k) = -\frac{V_{ij+1k} - V_{ijk}}{dy_j} \qquad E_y(x_i, y_{j-\frac{1}{2}}, z_k) = -\frac{V_{ijk} - V_{ij-1k}}{dy_{j-1}} \tag{B.9}$$

$$E_z(x_i, y_j, z_{k+\frac{1}{2}}) = -\frac{V_{ijk+1} - V_{ijk}}{dz_k} \qquad E_z(x_i, y_j, z_{k-\frac{1}{2}}) = -\frac{V_{ijk} - V_{ijk-1}}{dz_{k-1}} \tag{B.10}$$

with:

$$dx_i = x_{i+1} - x_i \qquad dy_j = y_{j+1} - y_j \qquad dz_k = z_{k+1} - z_k \tag{B.11}$$

Using the previous equations in Eq. B.4, we can establish the equation to be solved for node (x_i,y_j,z_k):

$$\begin{aligned} a_{ijk}V_{ijk} - a_{i+1jk}V_{i+1jk} - a_{i-1jk}V_{i-1jk} - a_{ij+1k}V_{ij+1k} - \\ a_{ij-1k}V_{ij-1k} - a_{ijk+1}V_{ijk+1} - a_{ijk-1}V_{ijk-1} = 4\pi Q_{ijk}, \end{aligned} \tag{B.12}$$

where:

$$a_{i+1jk} = \frac{1}{4dx_i}\left(\varepsilon_1 dy_j dz_k + \varepsilon_2 dy_{j-1} dz_k + \varepsilon_3 dy_j dz_{k-1} + \varepsilon_4 dy_{j-1} dz_{k-1}\right) \tag{B.13}$$

$$a_{i-1jk} = \frac{1}{4dx_{i-1}}\left(\varepsilon_5 dy_j dz_k + \varepsilon_6 dy_{j-1} dz_k + \varepsilon_7 dy_j dz_{k-1} + \varepsilon_8 dy_{j-1} dz_{k-1}\right) \tag{B.14}$$

$$a_{ij+1k} = \frac{1}{4dy_j}\left(\varepsilon_6 dx_i dz_k + \varepsilon_7 dx_{i-1} dz_k + \varepsilon_8 dx_i dz_{k-1} + \varepsilon_9 dx_{i-1} dz_{k-1}\right) \tag{B.15}$$

$$a_{ij-1k} = \frac{1}{4dy_{j-1}}\left(\varepsilon_7 dx_i dz_k + \varepsilon_8 dx_{i-1} dz_k + \varepsilon_9 dx_i dz_{k-1} + \varepsilon_{10} dx_{i-1} dz_{k-1}\right) \tag{B.16}$$

$$a_{ijk+1} = \frac{1}{4dz_k}\left(\varepsilon_{11} dx_i dy_j + \varepsilon_{12} dx_{i-1} dy_j + \varepsilon_{13} dx_i dy_{j-1} + \varepsilon_{14} dx_{i-1} dy_{j-1}\right) \tag{B.17}$$

$$a_{ijk-1} = \frac{1}{4dz_{k-1}}\left(\varepsilon_{11} dx_i dy_j + \varepsilon_{12} dx_{i-1} dy_j + \varepsilon_{13} dx_i dy_{j-1} + \varepsilon_{14} dx_{i-1} dy_{j-1}\right) \tag{B.18}$$

$$a_{ijk} = a_{i+1jk} + a_{i-1jk} + a_{ij+1k} + a_{ij-1k} + a_{ijk+1} + a_{ijk-1} \tag{B.19}$$

We can then build the discrete laplacian and solve Eq. B.1 using an interative method. In our case, a Conjugate-Gradient resolution is used. Note that in MMonCa, the charge Q_{ijk} resulting from ionized impurities is computed at each node by a dedicated algorithm (not detailed here) to map discrete particles on nodes.

B.2 Non-linear Poisson equation

In the previous section, we were computing the unscreened potential created by ionized impurities. However, in a semiconductor free carriers rearrange around the ionized impurity and impact the potential. To do that we need to account for the impact of electron and holes concentrations in the calculation of the charge. However, their concentration is given by Fermi-Dirac statistics that makes appear the unknown potential in the calculation of Fermi-Dirac integral. Then, the resulting Poisson equation becomes non-linear:

$$\varepsilon \boldsymbol{\Delta} E_F = -4\pi\left(Nv \times \mathcal{F}_{1/2}\left(-\frac{E_F}{kT}\right) - Nc \times \mathcal{F}_{1/2}\left(\frac{E_F - E_G}{kT}\right) + \rho\right) \tag{B.20}$$

In MMonCa, the self–consistent resolution of Eq. B.20 is achieved using the Newton–Raphson method [Selberherr 1984].

Résumé en français

Introduction

La fabrication de circuits intégrés nécessite de réduire les dimensions des dispositifs microélectroniques dans le but d'augmenter leurs performances et d'accroître la densité des composants (c'est à dire intégrer de plus en plus de dispositifs sur une même puce). Au cours des 40 dernières années, la taille des transistors a été réduite de façon drastique en suivant la fameuse loi de Moore selon laquelle le nombre de transistors des microprocesseurs double tous les deux ans. Cela a contribué au développement de circuits de plus en plus performants. Néanmoins, il existe un consensus sur le fait que les dimensions des transistors actuels approchent les limites physiques de miniaturisation. Au delà de cette limite, des alternatives doivent être introduites afin de remplacer l'architecture planaire sur substrat massif utilisée classiquement. Parmi elles, l'utilisation de substrat silicium sur isolant (*Silicon–On–Insulator*, SOI), d'architectures non planaires telles que FinFETs ou nanofils ou une combinaison des deux, sont considérées comme étant les options technologiques les plus prometteuses par l'industrie de la microélectronique. Par exemple, STMicroelectronics a choisi de développer une technologie de silicium sur isolant complètement déplétée (*fully depleted Silicon–On–Insulator*, FDSOI) pour les nœuds 28 nm et 14 nm. En revanche, Intel a développé une architecture de transistors non-planaires sur substrat massif, dit *Trigate* pour son nœud 22 nm.

Une alternative à la réduction des dimensions tout en augmentant la densité des circuit intégrés est l'intégration 3D séquentielle (également appelée intégration 3D monolithique). Cette technique consiste à empiler successivement sur un même substrat plusieurs couches de transistors séparées par un isolant [Batude *et al.* 2011a, Batude *et al.* 2013]. Il s'agit d'un domaine de recherche actif au sein du CEA Leti. Toutefois sa mise en œuvre est confrontée à une difficulté technique de taille qui consiste à être capable de fabriquer un transistor sur les étages supérieurs avec un budget thermique réduit (typiquement moins de 600 °C). Cette réduction de budget thermique permet de préserver les transistors situés sur les étages inférieurs de toute dégradation dans la mesure où les couches sont fabriquées les unes à la suite des autres. Cela implique un changement drastique de l'activation des dopants qui est classiquement réalisée à une température élevée (recuit spike de l'ordre de 1050 °C). Jusqu'à maintenant, l'option technologique choisie par le CEA Leti est de former les jonctions en utilisant la recristallisation par épitaxie en phase solide (*Solid Phase Epitaxial Regrowth*, SPER) d'une région préalablement amorphisée, ce qui permet de réduire le recuit d'activation à des températures entre 500 et 600 °C et qui sont compatibles avec une intégration 3D séquentielle.

De façon plus générale, la formation de jonction est une étape particulièrement critique pour les nœuds technologiques avancés. En effet, d'un côté, des niveaux élevés d'activation des dopants sont nécessaires afin de réduire les résistances d'accès. De l'autre, la diffusion des dopants doit être faible pour limiter les effets canaux–courts et éviter les problèmes liés à la réduction des dimensions. Parmi les options technologiques disponibles, l'activation SPER évoquée précédemment permet de répondre à ces deux critères dans la mesure où elle permet de former des jonctions abruptes avec des niveaux d'activation élevés. Cette technique implique une amorphisation préalable du substrat cristallin, soit en utilisant le dopant lui même lors de l'étape d'implantation, soit en réalisant une étape dite de pré–amorphisation

(*pre–amorphizing implantation*, PAI) en implantant une espèce plus lourde. Ensuite la région amorphisée recristallise par épitaxie en phase solide. Les dopants présents dans la zone amorphe sont incorporés en position substitutionnelle lors de la transformation de phase. En particulier, la nature hors équilibre de la SPER permet d'atteindre des niveaux d'activation métastables environ un à deux ordre de grandeurs plus élevés que la solubilité limite de l'impureté considérée dans le silicium.

Ce travail est destiné à modéliser et simuler la recristallisation par épitaxie en phase solide en utilisant une méthode de Monte Carlo cinétique (*kinetic Monte Carlo*, KMC) dans le but de mieux comprendre les mécanismes physiques jouant un rôle dans la formation de jonctions lors des procédés de fabrications à faible budget thermique.

Chapitre 1: Contexte et but de ce travail

Ce chapitre présente tout d'abord le contexte technologique et de simulation. Le procédé d'intégration 3D séquentielle est détaillé et permet d'introduire les procédés pour lesquels le budget thermique est limité à des températures inférieurs à 600 °C. Lors de la réalisation d'un tel procédé, l'étape de formation des jonctions se retrouve modifiée car les recuits utilisés conventionnellement pour l'activation des dopants dépassent les 1000 °C. C'est la raison pour laquelle la recristallisation par épitaxie en phase solide (*Solid Phase Epitaxial Regrowth*, SPER) est utilisée car elle permet d'atteindre des concentrations de dopants électriquement actifs élevées tout en limitant leur diffusion, ce qui est souhaitable pour les nœuds technologiques considérés. Néanmoins cette étape requiert des précautions particulières lors de l'implantation ionique utilisée pour incorporer les dopants et pour la création de la région amorphe. Pour optimiser le procédé, l'utilisation de la simulation numérique constitue un outil incontournable.

Aux échelles considérées, la nature atomistique des phénomènes observés devient importante et il est par conséquent indispensable d'utiliser des outils de simulation atomistique. Parmi eux, la dynamique moléculaire et les méthodes de Monte Carlo cinétique (*kinetic Monte Carlo* KMC) permettent de simuler la dynamique d'un système sous l'influence de la température. Néanmoins, bien que plus fondamentale que la simulation KMC, la dynamique moléculaire ne permet pas d'atteindre les temps physiques utilisés dans les procédés car elle est limitée à quelques microsecondes. La majeur partie de la simulation est dédié à la description de la vibration atomique (de l'ordre de 100 femtosecondes) et qui nécessite des pas d'intégration beaucoup plus petits (de l'ordre de la femtoseconde). C'est la raison pour laquelle la méthode KMC a été introduite: à partir d'un catalogue d'évènements possibles (qui doivent par conséquent être connus à l'avance), l'évolution du système se fait par des tirages aléatoires des évènements possibles. La méthode KMC est adaptée pour étudier l'évolution des matériaux lors des étapes de fabrication d'un procédé technologique. Toutefois, un certain *a priori* est nécessaire sur la nature des évènements microscopiques jouant un rôle ainsi que leur cinétique et peut s'avérer être une étape extrêmement complexe. La cinétique peut être modélisée par la théorie de l'état de transition dans son approximation harmonique ce qui revient à exprimer la fréquence de transition sous la forme:

$$k^{HTST} = \nu_0 \times \exp\left(-\frac{\Delta V}{k_B T}\right), \tag{B.21}$$

où ν_0 est un préfacteur, ΔV la barrière d'énergie pour la transition considérée, et $k_B T$ l'énergie thermique.

L'objectif de ce travail de thèse est de modéliser la SPER à partir de simulations atomistiques en prenant en compte les différentes dépendances auxquelles sa cinétique est sensible. Le cadre informatique de ce développement repose sur l'outil MMonCa qui a été créé par le Dr. Ignacio Martín–Bragado à l'IMDEA Materials institute (Madrid, Espagne).

Chapitre 2: Recristallisation par épitaxie en phase solide du silicium intrinsèque

Ce chapitre présente un résumé des aspects thermodynamiques et cinétiques de la SPER. Il apparaît que la SPER est principalement régie par la cinétique et est un phénomène qui se déroule à l'interface amorphe/cristal du fait de sa forte dépendance avec l'orientation cristalline. En effet, il est observé expérimentalement que la vitesse peut varier d'un facteur 20 selon l'orientation cristalline considérée. La vitesse de recristallisation peut être décrite par un comportement de type Arrhenius et peut donc s'écrire:

$$v(\theta, T) = K(\theta) \exp\left(-\frac{E_a}{k_B T}\right), \tag{B.22}$$

où E_a désigne l'énergie d'activation (2.7 eV pour le silicium) et K(θ) est un pré–facteur dépendant de l'orientation cristalline où θ est l'angle allant de la direction $\langle 100 \rangle$ à la direction $\langle 110 \rangle$.

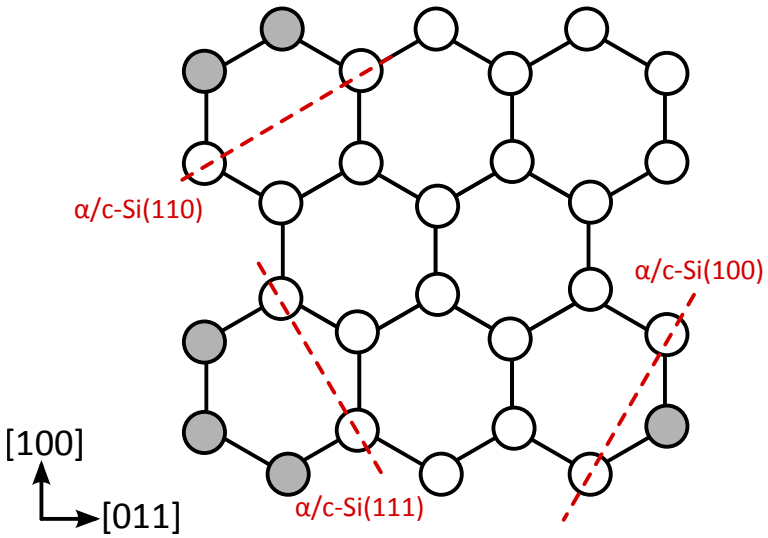

Figure 1: Schéma des différentes configurations microscopiques {100},{110} et {111} considérées dans le modèle LKMC. Les atomes appartenant à la phase cristalline sont représentés en blanc et ceux appartenant à la phase amorphe en gris.

A partir de ces considérations, un modèle atomistique phénoménologique a été introduit en s'appuyant sur une méthode de type Monte Carlo cinétique (KMC). Ce modèle considère une représentation explicite de l'interface amorphe/cristal et assigne un drapeau à chaque atome selon s'il est *amorphe* ou *cristallin* (c'est à dire appartenant à la phase amorphe ou la phase cristalline). Ce modèle a par la suite été étendu dans le module de Monte Carlo cinétique sur réseau (*lattice kinetic Monte Carlo*, LKMC) du simulateur MMonCa durant cette thèse. Ce modèle permet de simuler à la fois l'anisotropie et la formation de défauts cristallins de type macles. L'anisotropie est implémentée en introduisant une distinction entre les configurations

microscopiques {100}, {110} and {111} (en fonction du plan cristallographique dans lequel elles se trouvent), représentées schématiquement sur la Fig.1. Chaque configuration située à l'interface amorphe/cristal est déterminée à la volée par une analyse des plus proches voisins et en considérant le critère émis par Drosd and Washburn [Drosd & Washburn 1982] selon lequel deux liaisons non déformées doivent être formées pour recristalliser. Ainsi une configuration {100} nécessitera seulement un atome pour compléter un hexagone caractéristique d'une structure de type diamant. De façon similaire, une configuration {110} ou {111} nécessitera respectivement deux et trois atomes. La probabilité de recristallisation pour chacune des configurations considérées est donnée par l'équation:

$$\nu = K_{configuration} \times \exp\left(-E_a/k_B T\right), \tag{B.23}$$

où $K_{configuration}$ est un pré–facteur dépendant de la configuration et E_a désigne l'énergie d'activation du processus (2.7 eV pour le silicium et indépendant de la configuration). La formation de macles (Fig. 2) durant la recristallisation des configurations {111} a été introduite récemment (voir [Martin-Bragado & Sklenard 2012]). Pour cela, l'algorithme de reconstruction du réseau cristallin à partir de l'interface amorphe/cristal détermine à la volée la configuration correspondant à une macle permettant de compléter un hexagone.

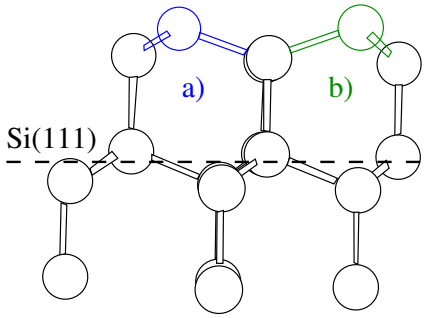

Figure 2: (a) Configuration normale et (b) macle sur un plan de {111}.

Le modèle a été utilisé pour simuler la recristallisation d'une interface amorphe/cristal planaire, selon différentes orientations (Fig. 3 et 4). Les résultats de simulations de la vitesse de recroissance en fonction de l'orientation cristalline reproduisent très bien les mesures expérimentales issues de la littérature. En outre, dans le cas de la recristallisation de substrats Si(111), les simulations mettent en évidence l'existence d'un double régime de vitesse (lente puis rapide) représenté sur la Fig. 5 et qui a été observé expérimentalement dans les années 70 [Csepregi *et al.* 1976]. Nous avons pu expliquer le phénomène en analysant l'origine microscopique de la formation puis l'évolution de différents types de macles (parallèles à l'interface puis inclinés). Nous avons observé que durant le régime initial, la recristallisation du Si(111) est réalisée majoritairement à travers des évènements de type {111} et est par conséquent très lente et très défectueuse (car les macles se forment sur un plan {111}). Le second régime est quant–à–lui produit par le fait que les défauts générés donnent naissance à un germe sur lequel des macles inclinées vont croître tout en étant compatibles avec la structure. Cela conduit à la formation d'un grain dont les mécanismes de recristallisation ne sont pas régis par des configurations {111}. Ce second régime est donc (i) plus rapide car il implique des configuration microscopiques {110} ou {100} qui ont une fréquence de recristallisation plus élevée que celle des configurations {111}, (ii) plus rugueuse car les grains ne suivent pas l'orientation du substrat Si(111) initial et (iii) moins défectueux mais avec des macles plus grosses.

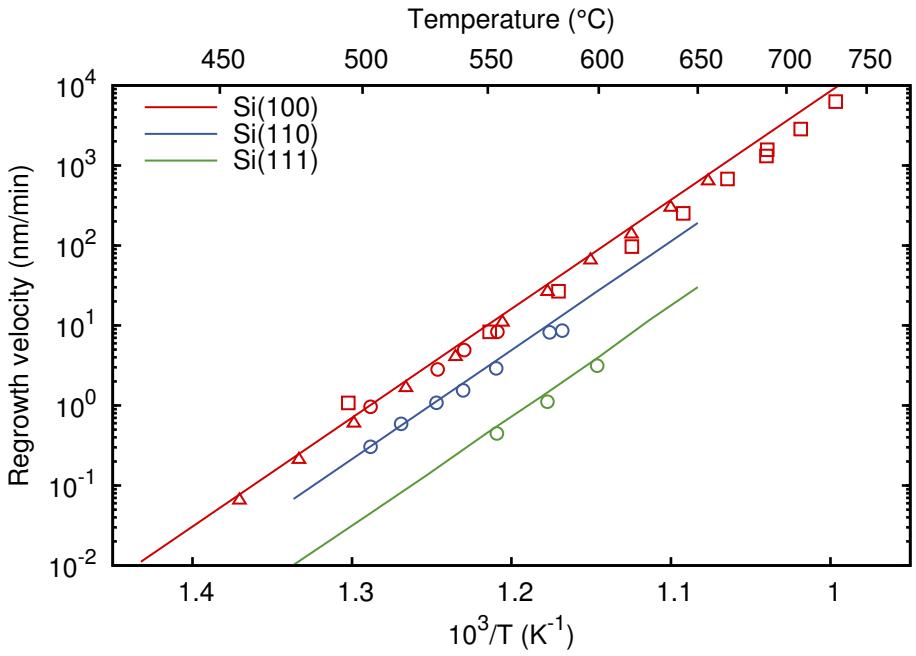

Figure 3: Vitesse de recristallisation dans les directions ⟨100⟩, ⟨110⟩ et ⟨111⟩. Les symboles correspondent aux données expérimentales de [Roth *et al.* 1990] (□), [Csepregi *et al.* 1978] (○) et [Johnson & McCallum 2007] (△) et les lignes aux résultats de simulations en utilisant le modèle LKMC.

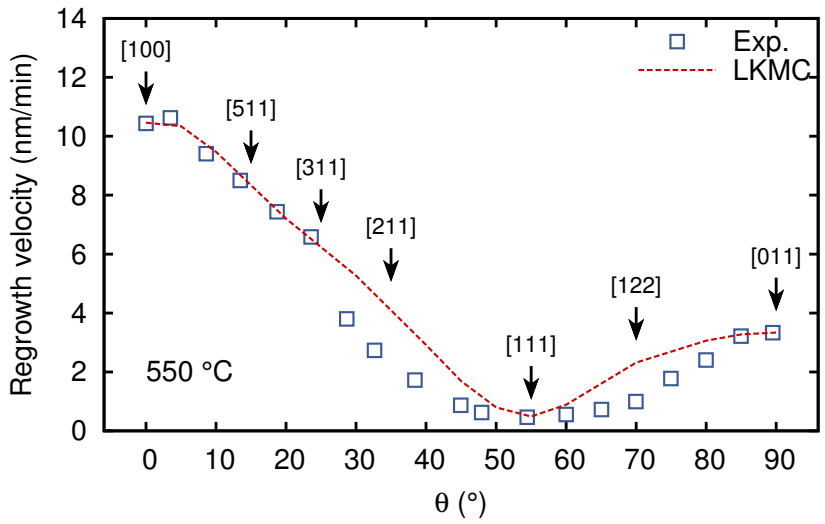

Figure 4: Vitesse de recristallisation à 550 °C en fonction de l'angle allant d'une recristallisation dans une direction [100] à une recristallisation dans une direction [011]. Les symboles correspondent aux mesures expérimentales de [Csepregi *et al.* 1978] et les lignes les résultats de simulations en utilisant le modèle LKMC.

La recristallisation multi–directionnelle a également été étudiée avec le modèle LKMC et constitue un intérêt du point de vu technologique. Pour cela, deux situations ont été considérées:

1. des régions amorphes délimitées par des tranchées remplies d'un isolant (ces régions correspondent à des zones actives délimitées latéralement par des tranchées d'isolation)

2. des régions amorphes ayant une forme rectangulaire (ces régions correspondent à des structures délimitées latéralement par du Si cristallin)

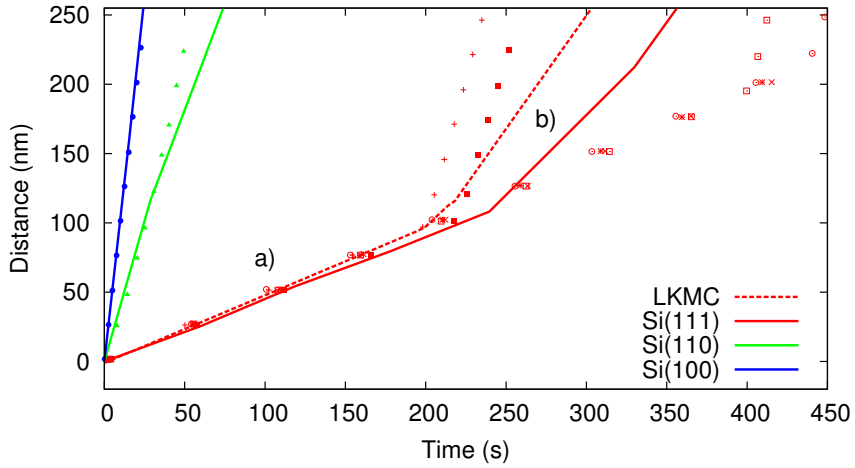

Figure 5: Comparaison des résultats de simulations LKMC (lignes) avec des mesures expérimentales de [Csepregi *et al.* 1976] (symboles) pour des substrats Si(100), Si(110) et Si(111). Dans le cas du Si(111) différents résultats sont représentés correspondant à différents tirages aléatoires ainsi que la moyenne de ces résultats (ligne en pointillés). Le modèle LKMC permet de reproduire et expliquer le double régime de vitesse (a) et (b).

Dans le cas de la recristallisation de régions amorphes délimitées par des tranchées d'isolation, des facettes se forment au niveau de l'interface entre le silicium amorphe et l'isolant du fait du manque de l'information cristalline permettant une recroissance "normale". Nous avons utilisé le modèle LKMC pour simuler la recroissance d'un substrat Si(100) de structures dont la direction cristallographique perpendiculaire à la tranchée est $\langle 110 \rangle$ ou $\langle 100 \rangle$. Nous avons observé la formation de facettes $\{111\}$ dans le premier cas et $\{110\}$ dans le second. Les facettes $\{111\}$ donnent lieu à des régions défectives du fait de la formation de macles contrairement au cas où des facettes $\{110\}$ apparaissent. Par conséquent, la SPER de régions amorphes dont la direction cristallographique latérale est $\langle 100 \rangle$ permet une recristallisation de meilleure qualité contrairement à celles dont la direction cristallographique latérale est $\langle 110 \rangle$.

Lors de la SPER de régions amorphes ayant une forme rectangulaire, trois fronts de recristallisation coexistent: deux latéralement et un verticalement. Comme pour la recristallisation de zones amorphes délimitées par des tranchées d'isolation, des structures dont la direction cristallographique latérale est $\langle 100 \rangle$ conduisent à une meilleure qualité cristalline que celles dont la direction cristallographique latérale est $\langle 110 \rangle$, en bon accord avec les observations expérimentales.

Dans le cas de jonctions formées par recristallisation par épitaxie en phase solide à faible température dans des dispositifs MOSFETs FDSOI, les simulations LKMC montrent la formation de zone défectueuses délimitées par des facettes $\{111\}$ lorsque la direction du canal est $\langle 110 \rangle$ (Fig.6) . Au contraire, pour des transistors dont le canal est orienté dans la direction $\langle 100 \rangle$, on observe une recristallisation complète.

Des développements futurs devraient adresser le problème de l'évolution des macles avec des traitement thermique additionnels. En effet, Duffy *et al.* ont observés par microscopie électronique à transmission à haute résolution que ces défauts de recristallisation peuvent être guéris dans des structures germanium [Duffy *et al.* 2011]. Il faut noter que le modèle LKMC a également été utilisé pour simuler la SPER du germanium (voir [Darby *et al.* 2013]). Il serait donc technologiquement pertinent d'étendre le modèle aux alliages SiGe qui sont utilisés dans la formation des régions de source/drain des transistors MOSFETs de type *p*.

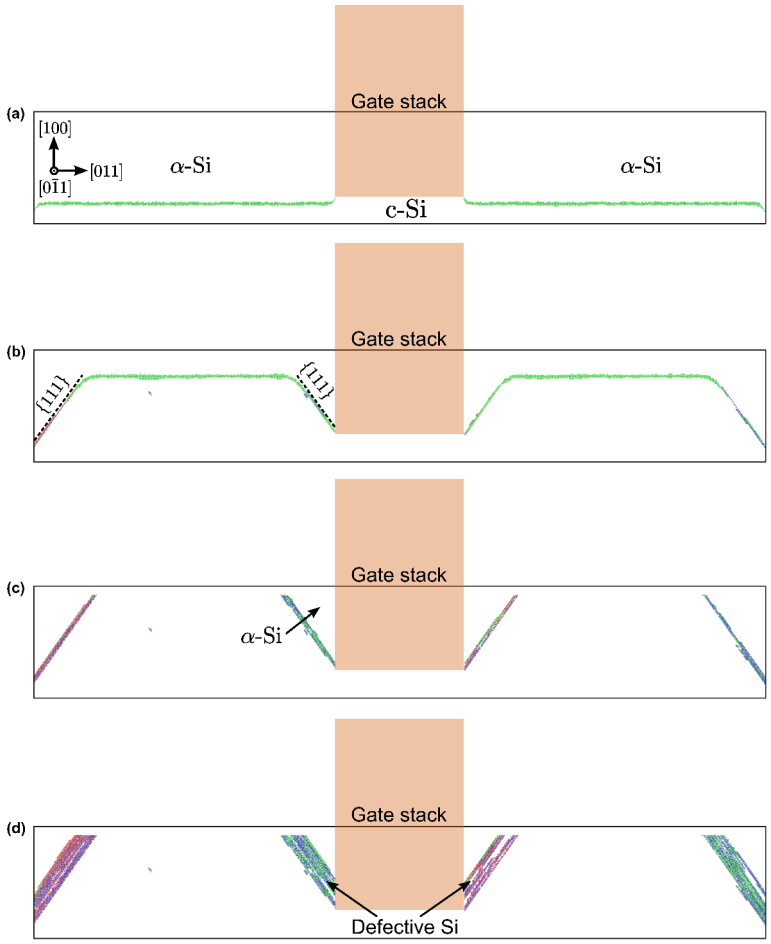

Figure 6: Représentation de l'interface amorphe/cristal à différents stade de la recristallisation d'une région amorphe dans un MOSFET FDSOI à 550 °C et dont le canal est orienté dans la direction $\langle 110 \rangle$: (a) après 10 s, (b) après 100 s, (c) après 200 s, et (d) après 600 s.

Chapitre 3: Impact de la contrainte sur la recristallisation par épitaxie en phase solide

Dans ce chapitre, l'impact de la contrainte sur la SPER a été examiné sur du Si(100). Différents états de contrainte ont été considérés: contrainte uniaxiale perpendiculaire à l'interface amorphe/cristal, contrainte uniaxiale dans le plan de recristallisation et contrainte hydrostatique. Le modèle LKMC implémenté dans MMonCa a été étendu afin de prendre en compte l'influence d'une contrainte locale sur les fréquences de recristallisation:

$$\nu = \nu(\sigma_{ij} = 0) \times \exp\left(\frac{\Delta V_{ij}^{*} \sigma^{ij}}{k_B T}\right), \tag{B.24}$$

où ΔV_{ij}^{*} est le tenseur d'activation introduit par Aziz *et al.* (voir [Aziz *et al.* 1991]), σ_{ij} est le tenseur des contraintes et $\nu(\sigma_{ij} = 0)$ la fréquence de recristallisation sans contrainte appliquée qui a été défini dans le chapitre précédent. En fonction du signe de la composante du tenseur d'activation, la correction conduit à une augmentation ou une réduction de la fréquence de recristallisation. Typiquement, une valeur négative (positive) entraine une augmentation (diminution) de la fréquence de recristallisation dans le cas d'une contrainte compressive ($\sigma < 0$). Ce sera le contraire pour une contrainte tensile ($\sigma > 0$).

Dans le modèle, on introduit une distinction entre les configurations $\{100\}$ ayant deux ou trois premiers voisins *cristallins* ce qui conduit à la définition de deux tenseurs d'activation différents. Par symétrie, $\Delta V^*_{22} = \Delta V^*_{33} = \Delta V^*_{\perp}$ et $\Delta V^*_{11} = \Delta V^*_{\parallel}$. Les composantes non diagonales sont considérées égales à zéro. Ainsi, le modèle contient quatre paramètres indépendants pour la prise en compte d'une contrainte non–hydrostatique.

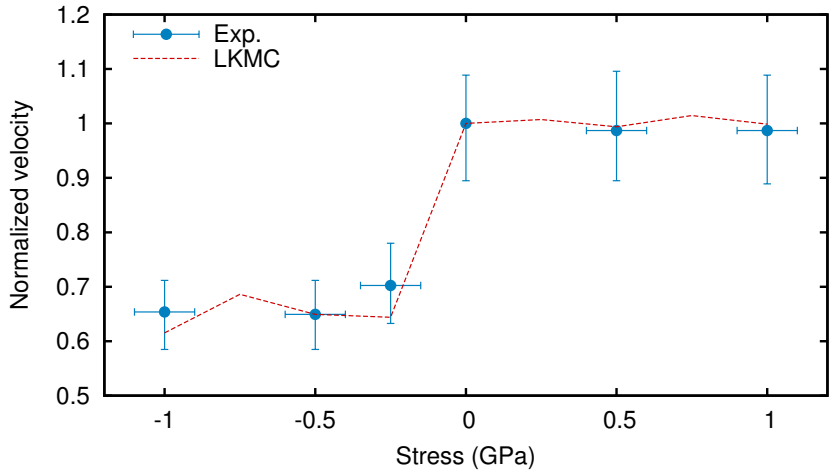

Figure 7: Évolution de la vitesse de recristallisation normalisée en fonction d'une contrainte uniaxiale appliquée dans le plan ($\sigma_{\perp}$). Les mesures expérimentales (symboles) sont issues de [Rudawski *et al.* 2008b] pour un recuit à 575 °C.

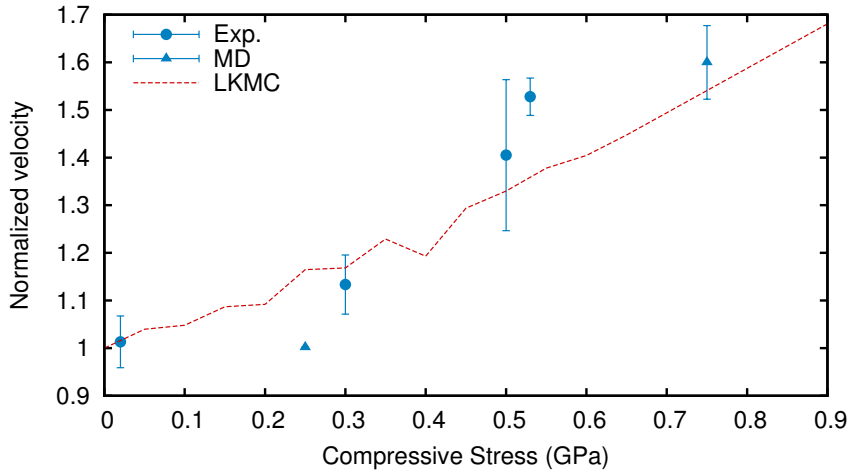

Figure 8: Évolution de la vitesse de recristallisation normalisée en fonction d'une contrainte uniaxiale compressive appliquée perpendiculairement à l'interface amorphe/cristal (σ_{11}). Les mesures expérimentales (cercles) proviennent de [Barvosa-Carter 1997] et les points issus de simulations en dynamique moléculaire (triangles) de[Bernstein *et al.* 2000].

Dans ce chapitre, nous montrons que ce modèle LKMC permet d'améliorer la compréhension des phénomènes microscopiques jouant un rôle lors de la SPER du Si(100) soumis à une contrainte:

- L'étude de l'impact d'une contrainte uniaxiale appliquée dans le plan de recristallisation (Fig. 7) montrent qu'une contrainte tensile n'induit pas de modification de la vitesse de

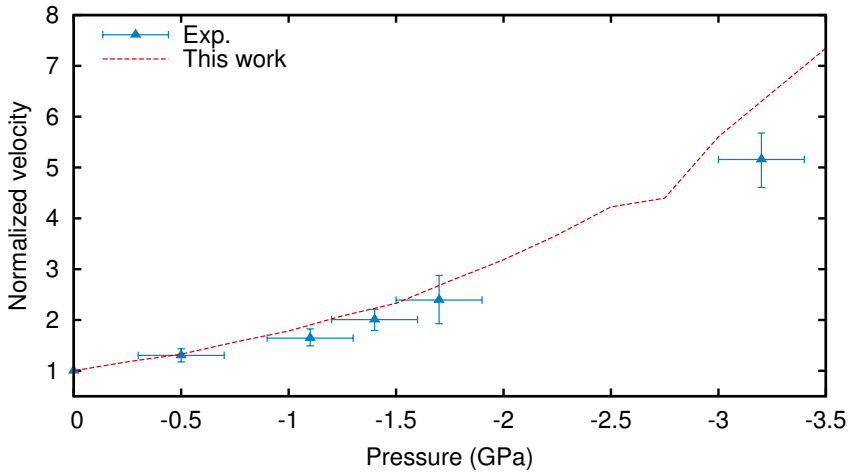

Figure 9: Évolution de la vitesse de recristallisation normalisée en fonction d'une contrainte hydrostatique ($\sigma_{11} = \sigma_{22} = \sigma_{33}$). Les mesures expérimentales (symboles) proviennent de [Lu *et al.* 1991] pour un recuit à 530 °C.

recroissance. En revanche, un ralentissement significatif de la vitesse est observée en compression. Cette diminution de la vitesse est due à une réduction de la fréquence des évènements {100} ayant 3 premiers voisins *cristallins* ce qui conduit à une augmentation de la rugosité de l'interface amorphe/cristal. Ces configurations jouent en effet un rôle important dans le processus de planarisation de l'interface. En outre, l'augmentation de la rugosité de l'interface lorsqu'une contrainte compressive est appliquée donne lieu à une recristallisation plus défectueuse à cause de la formation locale de facettes {111}.

- La recristallisation lorsqu'une contrainte compressive perpendiculaire à l'interface amorphe/cristal est appliquée (Fig. 8) donne lieu à un comportement similaire à celui obtenu lorsqu'une pression hydrostatique est appliquée (Fig. 9). Dans les deux cas, la vitesse de recristallisation augmente exponentiellement avec la contrainte.

Finalement, nous devons souligner que le modèle LKMC permet d'expliquer les incohérences entre le tenseur d'activation et le volume d'activation obtenues avec le modèle d'Aziz. La différence repose sur l'introduction de deux tenseurs d'activations correspondant à des configurations microscopiques distinctes.

Dans cette thèse, nous avons étendu le modèle LKMC afin de prendre en compte l'influence d'un champ de contrainte arbitraire sur la cinétique de recristallisation pour les configurations microscopiques {100} qui jouent un rôle principal lors de la SPER sur des substrats Si(100). Des développements additionnels seraient nécessaires pour généraliser ce modèle aux configurations microscopiques {110} et {111} afin de prendre en compte l'influence de la contrainte sur une direction arbitraire de recristallisation. Un tel modèle permettrait notamment l'étude de l'influence de la contrainte sur une recristallisation multi–directionnelle ce qui constitue un intérêt technologique majeur.

Chapitre 4: Influence des impuretés sur la recristallisation par épitaxie en phase solide

Dans ce chapitre, on discute dans un premier temps les concepts de solubilité limite et de solubilité métastable pour un dopant. Le premier correspond à la concentration maximale de dopant pouvant être incorporé lorsque le système est à l'équilibre thermodynamique (au delà, des précipités commencent à se former). Le second est défini hors équilibre thermodynamique et constitue un minimum énergétique local pouvant être plusieurs ordres de grandeur supérieur à la solubilité limite. Il s'agit par conséquent d'une quantité cinétique qui correspond, dans le cas de la SPER, à la concentration maximale de dopants pouvant être incorporés dans la phase cristalline lors de la transition amorphe/cristal. Cela permet d'expliquer le fait que la SPER permet d'atteindre des niveaux d'activation dépassant la solubilité limite du dopant considéré dans le silicium. Ces deux quantités sont importantes pour caractériser un procédé de fabrication technologique dans la mesure où elles permettent de déterminer quelle espèce s'avère être adaptée pour une application donnée.

En présence d'impuretés, la cinétique de recristallisation présente plusieurs comportements aussi étranges qu'intéressants. Tout d'abord, la vitesse de recroissance est plus lente par rapport à une référence intrinsèque en présence d'impuretés non dopantes. En revanche, en présence de dopants (qui a priori sont actifs et donc ionisés aux températures considérées), la vitesse augmente par rapport au cas intrinsèque jusqu'à atteindre une concentration critique. L'explication la plus vraisemblable de cet effet à ce jour correspond à une contribution d'ordre électrostatique où des défauts chargés seraient présents à l'interface amorphe/cristal. En outre pour certaines impuretés, un phénomène de ségrégation à l'interface amorphe/cristal est observés et serait corrélé avec la concentration critique au delà de laquelle la vitesse commence à ralentir. Cette ségrégation donne lieu à une redistribution du profil de dopants vers la surface (ce mécanisme est souvent appelé l'effet "chasse neige" dans la littérature).

Pour prendre en compte l'influence de la présence de dopants (actifs) sur la cinétique de recristallisation dans le modèle LKMC, une correction supplémentaire a été ajoutée dans le calcul des fréquences de recristallisation qui devient alors:

$$\nu = \nu_{intrinsic} \times \nu_{GFLS} \tag{B.25}$$

où $\nu_{intrinsic}$ est la fréquence dans le cas intrinsèque et ν_{GFLS} est une correction électrostatique basée sur un modèle de décalage du niveau de Fermi généralisé (*Generalized Fermi level shifting model*, GFLS) [Williams & Elliman 1983]. Ce modèle est basé sur la considération que la position relative du niveau de Fermi par rapport au minimum de la bande de conduction et le maximum de la bande de valence donne lieu à la formation de défauts chargés X^+ ou X^-, tandis que la concentrations de défauts neutres X^0 reste la même que dans le matériau intrinsèque. La présence de ces défauts chargés conduit à une accélération de la fréquence de recristallisation ν et donc une accélération de la vitesse de recristallisation. Ce modèle nécessite de calculer le potentiel électrostatique sur l'ensemble du domaine de simulation en 3D et d'actualiser le calcul au fur et à mesure que l'interface amorphe/cristal avance. Cela a été réalisé en implémentant un algorithme de résolution numérique non–linéaire de l'équation de Poisson couplé de façon auto–cohérente avec le modèle de Thomas–Fermi pour la description de la charge, à partir de la méthode des différences finies.

Les résultats de simulation de la vitesse de recristallisation normalisée par rapport au cas intrinsèque dans du Si(100) dopé avec de l'arsenic (Fig. 10) ou du bore (Fig. 11) en considérant

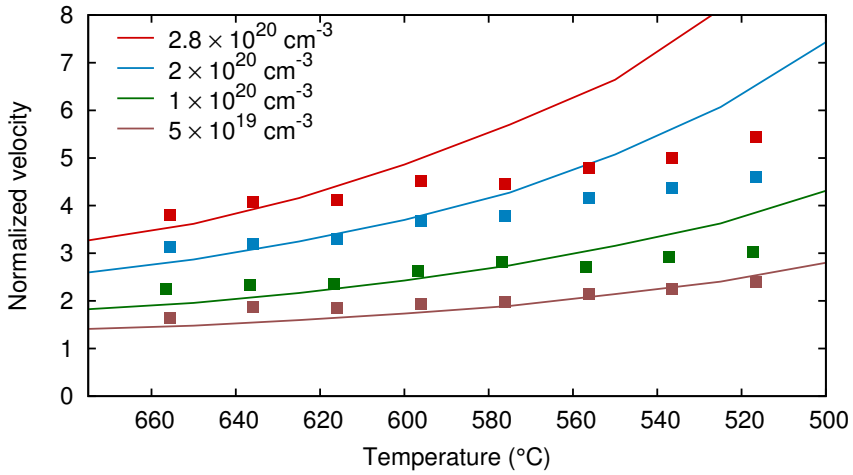

Figure 10: Vitesse de recristallisation normalisée en fonction de la température pour différentes concentrations d'As. Les résultats de simulations LKMC (lignes) sont comparés avec des mesures expérimentales (symboles) de [Johnson & McCallum 2007].

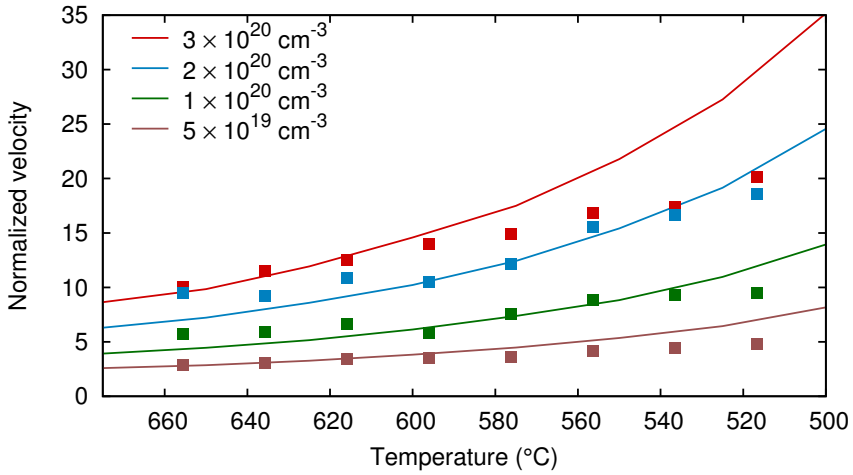

Figure 11: Vitesse de recristallisation normalisée en fonction de la température pour différentes concentrations de B. Les résultats de simulations LKMC (lignes) sont comparés avec des mesures expérimentales (symboles) de [Johnson & McCallum 2007].

différentes concentrations (constantes sur l'ensemble du domaine de simulation) montrent un relativement bon accord avec les mesures expérimentales. Néanmoins, à forte concentration on observe un désaccord entre la théorie et les résultats expérimentaux qui nécessiterait une analyse approfondie.

Conclusion et suggestions pour les recherches futures

Dans ce manuscrit, nous explorons les mécanismes physiques impliqués dans la recristallisation du silicium amorphisé par implantation ionique à travers le phénomène de recristallisation par épitaxie en phase solide. Cette technique est utilisée pour la formation de jonctions dans le cadre de procédés de fabrication de dispositifs dont le budget thermique est limité à des températures inférieures à 600 °C. L'avantage de ce procédé réside dans le fait qu'il permet d'atteindre des niveaux d'activation très élevés (au delà de la solubilité limite) tout en limitant

significativement la diffusion. Ces deux critères sont en effet importants pour les nœuds technologiques actuels et futurs. En outre, la limitation du budget thermique est nécessaire pour une intégration 3D séquentielle.

Le développement d'un modèle atomistique de SPER basé sur une approche Monte Carlo cinétique nous a permis de mettre en évidence l'influence de différents paramètres technologiques sur la cinétique de recroissance et pouvant conduire à une recristallisation de plus ou moins bonne qualité.

Dans ce travail de thèse, nous nous sommes principalement focalisé sur la description de la recristallisation en utilisant le module LKMC du simulateur MMonCa et les dopants ont été systématiquement considérés comme étant incorporés en position substitutionnelle lors de la transition amorphe/cristal (c'est à dire qu'ils deviennent électriquement "actifs" dans la phase cristalline). Toutefois, cette approximation, bien que valable pour des concentrations modérées n'est plus correcte à des fortes concentrations. A la fin de cette thèse, des analyses et des développements ont été entrepris afin d'intégrer un modèle de ségrégation trois–phases en vue de prendre en compte le phénomène de ségrégation à l'interface amorphe/cristal mais n'ont pas été présentés dans ce manuscrit. Des travaux supplémentaires seront nécessaires pour correctement prendre en compte ce phénomène complexe et directement lié à l'incorporation de dopants lors de la transition amorphe/cristal. Dans un second temps, il serait souhaitable de coupler les modules LKMC et OKMC de MMonCa afin de permettre la prise en compte des interactions entre les dopants incorporés dans le cristal avec les défauts cristallins.

Un autre sujet représentant un intérêt technologique serait d'étendre le modèle LKMC présenté à d'autres matériaux, et en particulier pour des alliages tels que le SiGe. L'évolution des macles avec la température et leur guérison éventuelle reste également un problème non résolu.

Comme il l'a été présenté dans le chapitre 3, la prise en compte de l'influence de la contrainte sur la recristallisation dans le modèle LKMC a été limitée aux configurations $\{100\}$. Un travail supplémentaire serait nécessaire afin de l'étendre aux configurations $\{110\}$ et $\{111\}$ afin d'être en mesure d'étudier la SPER dans un dispositif réel. En particulier, les techniques de mémorisation de la contrainte (*stress memorization techniques*, SMT) basées sur la formation de dislocations à partir de la SPER sont utilisées pour introduire de la contrainte dans les canaux de transistors afin d'augmenter la mobilité des porteurs. Ce type de techniques pourraient être en principe être étudiées par des simulations utilisant une approche KMC.

Enfin, la simulation de l'épitaxie (c'est à dire une croissance par une transition gas/solide) est en train de devenir un champ de recherche important, notamment du fait de son intérêt pour les nœuds technologiques futurs. En effet, les procédés de fabrication pour les nœuds à partir du 14 nm nécessitent:

- des épitaxies dopées *in–situ* pour former les régions source/drain,
- des épitaxies de matériaux à forte mobilité (tels que les III–V) pour la réalisation du canal du transistor.

Bibliography

[Albenze & Clancy 2005] Erik J. Albenze and Paulette Clancy. *Interface Response Functions for Amorphous and Crystalline Si and the Implications for Explosive Crystallization*. Mol. Simul., vol. 31, no. 1, pages 11–24, 2005.

[Alder & Wainwright 1957] B. J. Alder and T. E. Wainwright. *Phase Transition for a Hard Sphere System*. J. Chem. Phys., vol. 27, no. 5, pages 1208–1209, 1957.

[Alex *et al.* 1996] V. Alex, S. Finkbeiner and J. Weber. *Temperature dependence of the indirect energy gap in crystalline silicon*. J. Appl. Phys., vol. 79, no. 9, pages 6943–6946, 1996.

[Alonso & Simozar 1980] J. A. Alonso and S. Simozar. *Prediction of solid solubility in alloys*. Phys. Rev. B, vol. 22, pages 5583–5589, Dec 1980.

[Ashcroft & Mermin 1976] Neil W Ashcroft and N David Mermin. Solid State Physics. Holt Rinehart & Winston, 1976.

[Atkins 1986] P.W. Atkins. Physical Chemistry. W. H. Freeman, 3rd édition, 1986.

[Aziz *et al.* 1991] Michael J. Aziz, Paul C. Sabin and Guo-Quan Lu. *The activation strain tensor: Nonhydrostatic stress effects on crystal-growth kinetics*. Phys. Rev. B, vol. 44, pages 9812–9816, Nov 1991.

[Aziz *et al.* 2006] Michael J. Aziz, Yuechao Zhao, Hans-J. Gossmann, Salman Mitha, Stephen P. Smith and David Schiferl. *Pressure and stress effects on the diffusion of B and Sb in Si and Si-Ge alloys*. Phys. Rev. B, vol. 73, page 054101, Feb 2006.

[Aziz 1993] Michael J. Aziz. *Questions And Answers On The Activation Strain*. MRS Proceedings, vol. 321, 1 1993.

[Barkema & Mousseau 2000] G. T. Barkema and Normand Mousseau. *High-quality continuous random networks*. Phys. Rev. B, vol. 62, pages 4985–4990, Aug 2000.

[Barvosa-Carter & Aziz 1994] W. Barvosa-Carter and M. J. Aziz. *Nonhydrostatic Stress Effects on Solid Phase Epitaxial Growth in Silicon*. MRS Proceedings, vol. 356, 1 1994.

[Barvosa-Carter & Aziz 2001] W. Barvosa-Carter and M. J. Aziz. *Time-resolved measurements of stress effects on solid-phase epitaxy of intrinsic and doped Si*. Appl. Phys. Lett., vol. 79, no. 3, pages 356–358, 2001.

[Barvosa-Carter *et al.* 1998] William Barvosa-Carter, Michael J. Aziz, L. J. Gray and Theodore Kaplan. *Kinetically Driven Growth Instability in Stressed Solids*. Phys. Rev. Lett., vol. 81, pages 1445–1448, Aug 1998.

[Barvosa-Carter *et al.* 2004] William Barvosa-Carter, Michael J. Aziz, A.-V. Phan, T. Kaplan and L. J. Gray. *Interfacial roughening during solid phase epitaxy: Interaction of dopant, stress, and anisotropy effects*. J. Appl. Phys., vol. 96, no. 10, pages 5462–5468, 2004.

[Barvosa-Carter 1997] William Barvosa-Carter. *Stress Effects on Kinetics and Interfacial Roughening During Solid Phase Epitaxy*. PhD thesis, Harvard University, 1997.

[Batude *et al.* 2011a] P. Batude, M. Vinet, B. Previtali, C. Tabone, C. Xu, J. Mazurier, O. Weber, F. Andrieu, L. Tosti, L. Brevard, B. Sklenard, P. Coudrain, S. Bobba, H. Ben Jamaa, P. Gaillardon, A. Pouydebasque, O. Thomas, C. Le Royer, J. Hartmann, L. Sanchez, L. Baud, V. Carron, L. Clavelier, G. De Micheli, S. Deleonibus, O. Faynot and T. Poiroux. *Advances, challenges and opportunities in 3D CMOS sequential integration*. In Electron Devices Meeting (IEDM), 2011 IEEE International, pages 7.3.1–7.3.4, 2011.

[Batude *et al.* 2011b] P. Batude, M. Vinet, C. Xu, B. Previtali, C. Tabone, C. Le Royer, L. Sanchez, L. Baud, L. Brunet, A. Toffoli, F. Allain, D. Lafond, F. Aussenac, O. Thomas, T. Poiroux and O. Faynot. *Demonstration of low temperature 3D sequential FDSOI integration down to 50 nm gate length*. In VLSI Technology (VLSIT), 2011 Symposium on, pages 158–159, June 2011.

[Batude *et al.* 2013] P. Batude, B. Sklenard, C. Xu, B. Previtali, B. De Salvo and M. Vinet. *Low temperature FDSOI devices, a key enabling technology for 3D sequential integration*. In VLSI Technology, Systems, and Applications (VLSI-TSA), 2013 International Symposium on, pages 1–4, 2013.

[Bazant *et al.* 1997] Martin Z. Bazant, Efthimios Kaxiras and J. F. Justo. *Environment-dependent interatomic potential for bulk silicon*. Phys. Rev. B, vol. 56, pages 8542–8552, Oct 1997.

[Bernstein *et al.* 1998] N. Bernstein, M. J. Aziz and E. Kaxiras. *Amorphous-crystal interface in silicon: A tight-binding simulation*. Phys. Rev. B, vol. 58, pages 4579–4583, Aug 1998.

[Bernstein *et al.* 2000] N. Bernstein, M. J. Aziz and E. Kaxiras. *Atomistic simulations of solid-phase epitaxial growth in silicon*. Phys. Rev. B, vol. 61, pages 6696–6700, Mar 2000.

[Bortz *et al.* 1975] A.B. Bortz, M.H. Kalos and J.L. Lebowitz. *A new algorithm for Monte Carlo simulation of Ising spin systems*. J. Comput. Phys., vol. 17, no. 1, pages 10 – 18, 1975.

[Burbure *et al.* 2007] N. Burbure, N. G. Rudawski and K. S. Jones. *Effect of Oxide on Trench Edge Defect Formation in Ion-Implanted Silicon*. Electrochem. Solid State Lett., vol. 10, no. 6, pages H184–H185, 2007.

[Burke *et al.* 2005] Kieron Burke, Jan Werschnik and E. K. U. Gross. *Time-dependent density functional theory: Past, present, and future*. J. Chem. Phys., vol. 123, no. 6, page 062206, 2005.

[Cahn *et al.* 1980] J.W. Cahn, S.R. Coriell and W.J. Boettinger. *Rapid Solidification*. In C.W. WHITE and P.S. PEERCY, editeurs, Laser and Electron Beam Processing of Materials, pages 89 – 103. Academic Press, 1980.

[Cerva & Küsters 1989] H. Cerva and K.-H. Küsters. *Defect formation in silicon at a mask edge during crystallization of an amorphous implantation layer*. J. Appl. Phys., vol. 66, no. 10, pages 4723–4728, 1989.

[Csepregi *et al.* 1976] L. Csepregi, J. W. Mayer and T. W. Sigmon. *Regrowth behavior of ion-implanted amorphous layers on $\langle 111 \rangle$ silicon*. Appl. Phys. Lett., vol. 29, no. 2, pages 92–93, 1976.

[Csepregi *et al.* 1977] L. Csepregi, E. F. Kennedy, T. J. Gallagher, J. W. Mayer and T. W. Sigmon. *Reordering of amorphous layers of Si implanted with ^{31}P, ^{75}As, and ^{11}B ions*. J. Appl. Phys., vol. 48, no. 10, pages 4234–4240, 1977.

[Csepregi *et al.* 1978] L. Csepregi, E. F. Kennedy, J. W. Mayer and T. W. Sigmon. *Substrate-orientation dependence of the epitaxial regrowth rate from Si-implanted amorphous Si*. J. Appl. Phys., vol. 49, no. 7, pages 3906–3911, 1978.

[Custer *et al.* 1994] J. S. Custer, Michael O. Thompson, D. C. Jacobson, J. M. Poate, S. Roorda, W. C. Sinke and F. Spaepen. *Density of amorphous Si*. Appl. Phys. Lett., vol. 64, no. 4, pages 437–439, 1994.

[Dai *et al.* 1992] Peihua Dai, Youzhu Zhang and M. P. Sarachik. *Electrical conductivity of metallic Si:B near the metal-insulator transition*. Phys. Rev. B, vol. 45, pages 3984–3994, Feb 1992.

[D'Angelo *et al.* 2008] D. D'Angelo, L. Romano, I. Crupi, E. Carria, V. Privitera and M. G. Grimaldi. *Role of the strain in the epitaxial regrowth rate of heavily doped amorphous Si films*. Appl. Phys. Lett., vol. 93, no. 23, page 231901, 2008.

[Darby *et al.* 2013] B. L. Darby, B. R. Yates, I. Martin-Bragado, J. L. Gomez-Selles, R. G. Elliman and K. S. Jones. *Substrate orientation dependence on the solid phase epitaxial growth rate of Ge*. J. Appl. Phys., vol. 113, no. 3, page 033505, 2013.

[Demenev *et al.* 2012] E. Demenev, D. Giubertoni, S. Gennaro, M. Bersani, E. Hourdakis, A. G. Nassiopoulou, M. A. Reading and J. A. van den Berg. *Arsenic redistribution after solid phase epitaxial regrowth of shallow pre-amorphized silicon layers*. AIP Conference Proceedings, vol. 1496, no. 1, pages 272–275, 2012.

[Donovan *et al.* 1985] E. P. Donovan, F. Spaepen, D. Turnbull, J. M. Poate and D. C. Jacobson. *Calorimetric studies of crystallization and relaxation of amorphous Si and Ge prepared by ion implantation*. J. Appl. Phys., vol. 57, no. 6, pages 1795–1804, 1985.

[Drosd & Washburn 1982] R. Drosd and J. Washburn. *Some observations on the amorphous to crystalline transformation in silicon*. J. Appl. Phys., vol. 53, no. 1, pages 397–403, 1982.

[Duffy *et al.* 2005] R. Duffy, V. C. Venezia, K. van der Tak, M. J. P. Hopstaken, G. C. J. Maas, F. Roozeboom, Y. Tamminga and T. Dao. *Impurity redistribution due to recrystallization of preamorphized silicon*. Journal of Vacuum Science & Technology B: Microelectronics and Nanometer Structures, vol. 23, no. 5, pages 2021–2029, 2005.

[Duffy *et al.* 2006] R. Duffy, T. Dao, Y. Tamminga, K. van der Tak, F. Roozeboom and E. Augendre. *Groups III and V impurity solubilities in silicon due to laser, flash, and solid-phase-epitaxial-regrowth anneals*. Appl. Phys. Lett., vol. 89, no. 7, page 071915, 2006.

[Duffy *et al.* 2007] R. Duffy, M. J. H. Van Dal, B. J. Pawlak, M. Kaiser, R. G. R. Weemaes, B. Degroote, E. Kunnen and E. Altamirano. *Solid phase epitaxy versus random nucleation and growth in sub–20 nm wide fin field–effect transistors*. Appl. Phys. Lett., vol. 90, no. 24, page 241912, 2007.

[Duffy *et al.* 2010] R. Duffy, A. Heringa, V.C. Venezia, J. Loo, M.A. Verheijen, M.J.P. Hopstaken, K. van der Tak, M. de Potter, J.C. Hooker, P. Meunier-Beillard and R. Delhougne. *Quantitative prediction of junction leakage in bulk-technology {CMOS} devices*. Solid-State Electronics, vol. 54, no. 3, pages 243 – 251, 2010.

[Duffy *et al.* 2011] R. Duffy, M. Shayesteh, B. McCarthy, A. Blake, M. White, J. Scully, R. Yu, A.-M. Kelleher, M. Schmidt, N. Petkov, L. Pelaz and L. A. Marqués. *The curious case of thin–body Ge crystallization*. Appl. Phys. Lett., vol. 99, no. 13, page 131910, 2011.

[Eshelby 1956] J.D. Eshelby. *The Continuum Theory of Lattice Defects*. volume 3 of *Solid State Physics*, pages 79 – 144. Academic Press, 1956.

[Fichthorn & Weinberg 1991] Kristen A. Fichthorn and W. H. Weinberg. *Theoretical foundations of dynamical Monte Carlo simulations*. The Journal of Chemical Physics, vol. 95, no. 2, pages 1090–1096, 1991.

[Frenkel & Smit 2001] Daan Frenkel and B. Smit. Understanding Molecular Simulation, From Algorithms to Applications. Academic Press, 2nd édition, November 2001.

[Gardiner 2009] Crispin Gardiner. Stochastic methods: A handbook for the natural and social sciences. Springer, 4th édition, 2009.

[Gärtner & Weber 2003] K. Gärtner and B. Weber. *Molecular dynamics simulations of solid-phase epitaxial growth in silicon*. Nucl. Instr. Meth. Phys. Res. Section B: Beam Interactions with Materials and Atoms, vol. 202, pages 255 – 260, 2003.

[Glasstone *et al.* 1941] S. Glasstone, K.J. Laidler and H. Eyring. The theory of rate processes: the kinetics of chemical reactions, viscosity, diffusion and electrochemical phenomena. International chemical series. McGraw-Hill Book Company, inc., 1941.

[Green 1990] Martin A. Green. *Intrinsic concentration, effective densities of states, and effective mass in silicon*. J. Appl. Phys., vol. 67, no. 6, pages 2944–2954, 1990.

[Haynes *et al.* 1995] T. E. Haynes, M. J. Antonell, C. Archie Lee and K. S. Jones. *Composition dependence of solid-phase epitaxy in silicon-germanium alloys: Experiment and theory*. Phys. Rev. B, vol. 51, pages 7762–7771, Mar 1995.

[Ho *et al.* 1984] K. T. Ho, I. Suni and M-A. Nicolet. *Substrate orientation dependence of enhanced epitaxial regrowth of silicon*. J. Appl. Phys., vol. 56, no. 4, pages 1207–1212, 1984.

[Hobler & Otto 2003] G. Hobler and G. Otto. *Status and open problems in modeling of as–implanted damage in silicon*. Materials Science in Semiconductor Processing, vol. 6, no. 1–3, pages 1–14, 2003.

[Jain *et al.* 2004] S. H. Jain, P. B. Griffin, J. D. Plummer, S. Mccoy, J. Gelpey, T. Selinger and D. F. Downey. *Metastable boron active concentrations in Si using flash assisted solid phase epitaxy*. J. Appl. Phys., vol. 96, no. 12, pages 7357–7360, 2004.

[Johnson & McCallum 2007] B. C. Johnson and J. C. McCallum. *Dopant-enhanced solid-phase epitaxy in buried amorphous silicon layers*. Phys. Rev. B, vol. 76, page 045216, Jul 2007.

[Johnson *et al.* 2009] B.C. Johnson, P. Caradonna and J.C. McCallum. *Dopant enhanced H diffusion in amorphous silicon and its effect on the kinetics of solid phase epitaxy*. Materials Science and Engineering: B, vol. 157, no. 1–3, pages 6–10, 2009.

[Johnson *et al.* 2012] B. C. Johnson, T. Ohshima and J. C. McCallum. *Dopant effects on solid phase epitaxy in silicon and germanium*. J. Appl. Phys., vol. 111, no. 3, page 034906, 2012.

[Jones *et al.* 1988] K.S. Jones, S. Prussin and E.R. Weber. *A systematic analysis of defects in ion-implanted silicon*. Applied Physics A, vol. 45, no. 1, pages 1–34, 1988.

[Justo *et al.* 1998] João F. Justo, Martin Z. Bazant, Efthimios Kaxiras, V. V. Bulatov and Sidney Yip. *Interatomic potential for silicon defects and disordered phases*. Phys. Rev. B, vol. 58, pages 2539–2550, Aug 1998.

[Kail *et al.* 2010] F. Kail, J. Farjas, P. Roura, C. Secouard, O. Nos, J. Bertomeu, F. Alzina and P. Roca i Cabarrocas. *Relaxation and derelaxation of pure and hydrogenated amorphous silicon during thermal annealing experiments*. Appl. Phys. Lett., vol. 97, no. 3, page 031918, 2010.

[Kail *et al.* 2011] F. Kail, J. Farjas, P. Roura, C. Secouard, O. Nos, J. Bertomeu and P. Roca i Cabarrocas. *The configurational energy gap between amorphous and crystalline silicon*. Phys. Status Solidi RRL, vol. 5, no. 10-11, pages 361–363, 2011.

[Kail *et al.* 2012] F Kail, J Molera, J Farjas, P Roura, C Secouard and P Roca i Cabarrocas. *Can the crystallization rate be independent from the crystallization enthalpy? The case of amorphous silicon*. J. Phys.: Condens. Matter, vol. 24, no. 9, page 095401, 2012.

[Kim & Lundstrom 2008] Raseong Kim and Mark Lundstrom. *Notes on Fermi-Dirac Integrals (3rd Edition)*, 2008.

[Kittel 2005] Charles Kittel. Introduction to Solid State Physics. John Wiley & Sons, Inc., New York, 8th édition, 2005.

[Kuhn 2011] K.J. Kuhn. *CMOS scaling for the 22nm node and beyond: Device physics and technology*. In VLSI Technology, Systems and Applications (VLSI-TSA), 2011 International Symposium on, pages 1–2, 2011.

[Kyutt *et al.* 2001] R.N Kyutt, Nikolai A Sobolev, Yu.A Nikolaev and V.I Vdovin. *Defect structure of erbium-doped $\langle 111 \rangle$ silicon layers formed by solid phase epitaxy*. Nuclear Instruments and Methods in Physics Research Section B: Beam Interactions with Materials and Atoms, vol. 173, no. 3, pages 319 – 325, 2001.

[Laaziri *et al.* 1999] Khalid Laaziri, S. Kycia, S. Roorda, M. Chicoine, J. L. Robertson, J. Wang and S. C. Moss. *High-energy x-ray diffraction study of pure amorphous silicon*. Phys. Rev. B, vol. 60, pages 13520–13533, Nov 1999.

[Laidler & King 1983] Keith J. Laidler and M. Christine King. *Development of transition-state theory*. The Journal of Physical Chemistry, vol. 87, no. 15, pages 2657–2664, 1983.

[Lampin & Krzeminski 2009] E. Lampin and C. Krzeminski. *Molecular dynamics simulations of the solid phase epitaxy of Si: Growth mechanism and orientation effects*. J. Appl. Phys., vol. 106, no. 6, page 063519, 2009.

[Landau & Kurt 2009] David P. Landau and Binder Kurt. A guide to monte-carlo simulations in statistical physics. Cambridge University Press, 2009.

[Landau *et al.* 1980] L.D. Landau, E.M. Lifshitz and L.P. Pitaevskii. Statistical physics. Numeéro Vol. 5. Butterworth-Heinemann, 1980.

[Lang *et al.* 1983] Joseph E. Lang, Frank L. Madarasz and Patrick M. Hemenger. *Temperature dependent density of states effective mass in nonparabolic p–type silicon*. J. Appl. Phys., vol. 54, no. 6, pages 3612–3612, 1983.

[Lim *et al.* 2010] Kwan-Yong Lim, Hyunjung Lee, Choongryul Ryu, Kang-Ill Seo, Uihui Kwon, Seokhoon Kim, Jongwan Choi, Kyungseok Oh, Hee-Kyung Jeon, Chulgi Song, Tae-Ouk Kwon, Jinyeong Cho, Seunghun Lee, Yangsoo Sohn, Hong Sik Yoon, Junghyun Park, Kwanheum Lee, Wookje Kim, Eunha Lee, Sang-Pil Sim, Chung Geun Koh, Sang Bom Kang, Siyoung Choi and Chilhee Chung. *Novel stress-memorization-technology (SMT) for high electron mobility enhancement of gate last high-k/metal gate devices*. In Electron Devices Meeting (IEDM), IEEE International, pages 10.1.1 – 10.1.4, dec. 2010.

[Lohmeier *et al.* 1994] M. Lohmeier, S. de Vries, J. S. Custer, E. Vlieg, M. S. Finney, F. Priolo and A. Battaglia. *Interface roughness during thermal and ion-induced regrowth of amorphous layers on Si(001)*. Appl. Phys. Lett., vol. 64, no. 14, pages 1803–1805, 1994.

[Lu *et al.* 1989] G. Q. Lu, E. Nygren, M. J. Aziz, D. Turnbull and C. W. White. *Interferometric measurement of the pressure-enhanced crystallization rate of amorphous Si*. Appl. Phys. Lett., vol. 54, no. 25, pages 2583–2585, 1989.

[Lu *et al.* 1991] Guo-Quan Lu, Eric Nygren and Michael J. Aziz. *Pressure-enhanced crystallization kinetics of amorphous Si and Ge: Implications for point-defect mechanisms*. J. Appl. Phys., vol. 70, no. 10, pages 5323–5345, 1991.

[Luo *et al.* 2003] Xuan Luo, S. B. Zhang and Su-Huai Wei. *Understanding Ultrahigh Doping: The Case of Boron in Silicon*. Phys. Rev. Lett., vol. 90, page 026103, Jan 2003.

[Marqués *et al.* 2003] Luis A. Marqués, Lourdes Pelaz, Mar´Aboy, Lourdes Enr´and Juan Barbolla. *Microscopic Description of the Irradiation-Induced Amorphization in Silicon*. Phys. Rev. Lett., vol. 91, page 135504, Sep 2003.

[Martin-Bragado & Moroz 2009] Ignacio Martin-Bragado and Victor Moroz. *Facet formation during solid phase epitaxy regrowth: A lattice kinetic Monte Carlo model*. Appl. Phys. Lett., vol. 95, no. 12, page 123123, 2009.

[Martin-Bragado & Sklenard 2012] Ignacio Martin-Bragado and Benoit Sklenard. *Understanding Si(111) solid phase epitaxial regrowth using Monte Carlo modeling: Bimodal growth, defect formation, and interface topology*. J. Appl. Phys., vol. 112, no. 2, page 024327, 2012.

[Martin-Bragado *et al.* 2005a] I. Martin-Bragado, P. Castrillo, M. Jaraiz, R. Pinacho, J. E. Rubio and J. Barbolla. *Physical atomistic kinetic Monte Carlo modeling of Fermi-level effects of species diffusing in silicon*. Phys. Rev. B, vol. 72, page 035202, Jul 2005.

[Martin-Bragado *et al.* 2005b] I. Martin-Bragado, P. Castrillo, M. Jaraiz, R. Pinacho, J. E. Rubio, J. Barbolla and V. Moroz. *Fermi-level effects in semiconductor processing: A modeling scheme for atomistic kinetic Monte Carlo simulators*. J. Appl. Phys., vol. 98, no. 5, page 053709, 2005.

[Martin-Bragado *et al.* 2013] I. Martin-Bragado, A. Rivera, G. Valles, J. L. Gomez-Selles and M. J. Caturla. *MMonCa: An Object Kinetic Monte Carlo simulator for damage irradiation evolution and defect diffusion*. Comput. Phys. Commun., vol. 184, no. 12, pages 2703 – 2710, 2013.

[Martin-Bragado 2011] Ignacio Martin-Bragado. *{111} local configurations: The main source of silicon defects during solid phase epitaxial regrowth modeled by lattice kinetic Monte Carlo*. Appl. Phys. Lett., vol. 98, no. 23, page 233109, 2011.

[Martin-Bragado 2012] Ignacio Martin-Bragado. *Importance of twin defect formation created by solid-phase epitaxial growth: An atomistic study*. Scripta Materialia, vol. 66, no. 3–4, pages 186 – 189, 2012.

[McCallum 1996] J. C. McCallum. *Kinetics of solid phase epitaxy in buried amorphous Si layers formed by MeV ion implantation*. Appl. Phys. Lett., vol. 69, no. 7, pages 925–927, 1996.

[Metropolis & Ulam 1949] Nicholas Metropolis and S. Ulam. *The Monte Carlo Method*. J. Am. Stat. Assoc., vol. 44, no. 247, pages 335–341, 1949.

[Metropolis *et al.* 1953] Nicholas Metropolis, Arianna W. Rosenbluth, Marshall N. Rosenbluth, Augusta H. Teller and Edward Teller. *Equation of State Calculations by Fast Computing Machines*. The Journal of Chemical Physics, vol. 21, no. 6, pages 1087–1092, 1953.

[Morarka *et al.* 2008] Saurabh Morarka, N. G. Rudawski and Mark E. Law. *Level set modeling of the orientation dependence of solid phase epitaxial regrowth*. Journal of Vacuum Science & Technology B, vol. 26, no. 1, pages 357–361, 2008.

[Morarka *et al.* 2009] S. Morarka, N. G. Rudawski, M. E. Law, K. S. Jones and R. G. Elliman. *Modeling two-dimensional solid-phase epitaxial regrowth using level set methods*. J. Appl. Phys., vol. 105, no. 5, pages –, 2009.

[Narayan & Holland 1982] J. Narayan and O. W. Holland. *Formation of metastable supersaturated solid solutions in ion implanted silicon during solid phase crystallization*. Appl. Phys. Lett., vol. 41, no. 3, pages 239–242, 1982.

[Narayan *et al.* 1983] J. Narayan, O. W. Holland and B. R. Appleton. *Solid-phase-epitaxial growth and formation of metastable alloys in ion implanted silicon*. Journal of Vacuum Science & Technology B: Microelectronics and Nanometer Structures, vol. 1, no. 4, pages 871–887, 1983.

[Narayan 1982] J. Narayan. *Interface structures during solid-phase-epitaxial growth in ion implanted semiconductors and a crystallization model*. J. Appl. Phys., vol. 53, no. 12, pages 8607–8614, 1982.

[Nishi *et al.* 1978] Hidetoshi Nishi, Teruo Sakurai and Tsuneo Furuya. *Electrical Activation of implanted Arsenic in Silicon during Low Temperature anneal*. J. Electrochem. Soc., vol. 125, page 461, 1978.

[Nobili *et al.* 1989] D. Nobili, R. Angelucci, A. Armigliato, E. Landi and S. Solmi. *Equilibrium Carrier Density and Solubility of Antimony in Silicon*. J. Electrochem. Soc., vol. 136, no. 4, pages 1142–1146, 1989.

[Nobili *et al.* 1994] D. Nobili, S. Solmi, A. Parisini, M. Derdour, A. Armigliato and L. Moro. *Precipitation, aggregation, and diffusion in heavily arsenic-doped silicon*. Phys. Rev. B, vol. 49, pages 2477–2483, Jan 1994.

[Northrup & Zhang 1993] John E. Northrup and S. B. Zhang. *Dopant and defect energetics: Si in GaAs*. Phys. Rev. B, vol. 47, pages 6791–6794, Mar 1993.

[Nygren *et al.* 1985] Eric Nygren, Michael J. Aziz, David Turnbull, John M. Poate, Dale C. Jacobson and Robert Hull. *Effect of pressure on the solid phase epitaxial regrowth rate of Si*. Appl. Phys. Lett., vol. 47, no. 3, pages 232–233, 1985.

[Olson & Roth 1988] G.L. Olson and J.A. Roth. *Kinetics of solid phase crystallization in amorphous silicon*. Materials Science Reports, vol. 3, no. 1, pages 1 – 77, 1988.

[Pham-Nguyen *et al.* 2009] Loan Pham-Nguyen, C. Fenouillet-Beranger, A. Vandooren, T. Skotnicki, G. Ghibaudo and S. Cristoloveanu. *In Situ Comparison of Si/High–κ and Si/SiO_2 Channel Properties in SOI MOSFETs*. Electron Device Letters, IEEE, vol. 30, no. 10, pages 1075–1077, Oct 2009.

[Posselt *et al.* 2001] M. Posselt, L. Bischoff and J. Teichert. *Influence of dose rate and temperature on ion-beam-induced defect evolution in Si investigated by channeling implantation at different doses*. Appl. Phys. Lett., vol. 79, no. 10, pages 1444–1446, 2001.

[Pyykkö & Atsumi 2009] Pekka Pyykkö and Michiko Atsumi. *Molecular Single-Bond Covalent Radii for Elements 1–118*. Chem. Eur. J., vol. 15, no. 1, pages 186–197, 2009.

[Rechtin *et al.* 1978] M. D. Rechtin, P. P. Pronko, G. Foti, L. Csepregi, E. F. Kennedy and J. W. Mayer. *An electron microscopy study of defect structures in recrystallized amorphous layers of self-ion-irradiated $\langle 111 \rangle$ silicon*. Philosophical Magazine A, vol. 37, no. 5, pages 605–620, 1978.

[Roorda *et al.* 1989] S. Roorda, S. Doorn, W. C. Sinke, P. M. L. O. Scholte and E. van Loenen. *Calorimetric evidence for structural relaxation in amorphous silicon*. Phys. Rev. Lett., vol. 62, pages 1880–1883, Apr 1989.

[Roorda *et al.* 1991] S. Roorda, W. C. Sinke, J. M. Poate, D. C. Jacobson, S. Dierker, B. S. Dennis, D. J. Eaglesham, F. Spaepen and P. Fuoss. *Structural relaxation and defect annihilation in pure amorphous silicon*. Phys. Rev. B, vol. 44, pages 3702–3725, Aug 1991.

[Roth *et al.* 1990] J. A. Roth, G. L. Olson, D. C. Jacobson and J. M. Poate. *Kinetics of solid phase epitaxy in thick amorphous Si layers formed by MeV ion implantation*. Appl. Phys. Lett., vol. 57, no. 13, pages 1340–1342, 1990.

[Roura *et al.* 2008] P. Roura, J. Farjas and P. Roca i Cabarrocas. *Quantification of the bond-angle dispersion by Raman spectroscopy and the strain energy of amorphous silicon*. J. Appl. Phys., vol. 104, no. 7, page 073521, 2008.

[Roura *et al.* 2011] P. Roura, D. Sanchez-Rodriguez and J. Farjas. *Measurement by differential scanning calorimetry of specific heat capacity variation due to crystallization: Application to amorphous silicon*. Thermochimica Acta, vol. 522, no. 1 - 2, pages 161 – 165, 2011.

[Roura *et al.* 2013] P. Roura, F. Taïr, J. Farjas and P. Roca i Cabarrocas. *Measurement of the specific heat and determination of the thermodynamic functions of relaxed amorphous silicon*. J. Appl. Phys., vol. 113, no. 17, page 173515, 2013.

[Rudawski & Jones 2009] N.G. Rudawski and K.S. Jones. *Atomistic considerations of stressed epitaxial growth from the solid phase*. Scr. Mater., vol. 61, no. 3, pages 327 – 330, 2009.

[Rudawski *et al.* 2006] N. G. Rudawski, K. N. Siebein and K. S. Jones. *Effect of uniaxial stress on solid phase epitaxy in patterned Si wafers*. Appl. Phys. Lett., vol. 89, no. 8, page 082107, 2006.

[Rudawski *et al.* 2008a] N. G. Rudawski, K. S. Jones and R. Gwilliam. *Kinetics and Morphological Instabilities of Stressed Solid-Solid Phase Transformations*. Phys. Rev. Lett., vol. 100, page 165501, Apr 2008.

[Rudawski *et al.* 2008b] N.G. Rudawski, K.S. Jones and R. Gwilliam. *Stressed solid-phase epitaxial growth of ion-implanted amorphous silicon*. Mater. Sci. Eng. R – Rep., vol. 61, no. 1–6, pages 40–58, 2008.

[Rudawski *et al.* 2009] N. G. Rudawski, K. S. Jones, S. Morarka, M. E. Law and R. G. Elliman. *Stressed multidirectional solid-phase epitaxial growth of Si*. J. Appl. Phys., vol. 105, no. 8, page 081101, 2009.

[Rudawski 2008] Nicholas G. Rudawski. *Stressed Solid Phase Epitaxial Growth of Silion*. PhD thesis, University of Florida, 2008.

[Saenger *et al.* 2007a] K. L. Saenger, J. P. de Souza, K. E. Fogel, J. A. Ott, C. Y. Sung, D. K. Sadana and H. Yin. *A study of trench-edge defect formation in (001) and (011) silicon recrystallized by solid phase epitaxy*. J. Appl. Phys., vol. 101, no. 2, page 024908, 2007.

[Saenger *et al.* 2007b] K. L. Saenger, K. E. Fogel, J. A. Ott, D. K. Sadana and H. Yin. *An examination of facet formation during solid phase epitaxy of line-shaped amorphized regions in (001) and (011) Si*. J. Appl. Phys., vol. 101, no. 10, page 104908, 2007.

[Sage *et al.* 2000] Jennifer F. Sage, William Barvosa-Carter and Michael J. Aziz. *Morphological instability of growth fronts due to stress-induced mobility variations*. Appl. Phys. Lett., vol. 77, no. 4, pages 516–518, 2000.

[Sage *et al.* 2006] Jennifer F. Sage, William Barvosa-Carter and Michael J. Aziz. *Strain-stabilized solid phase epitaxy of Si–Ge on Si*. J. Appl. Phys., vol. 99, no. 11, page 113529, 2006.

[Secco d'Aragona 1972] F. Secco d'Aragona. *Dislocation Etch for (100) Planes in Silicon*. J. Electrochem. Soc., vol. 119, no. 7, pages 948–951, 1972.

[Selberherr 1984] S. Selberherr. Analysis and simulation of semiconductor devices. Springer-Verlag, 1984.

[Shanavas *et al.* 2012] K. V. Shanavas, K. K. Pandey, Nandini Garg and Surinder M. Sharma. *Computer simulations of crystallization kinetics in amorphous silicon under pressure*. J. Appl. Phys., vol. 111, no. 6, page 063509, 2012.

[Shen *et al.* 2012] Tzer-Min Shen, Yen-Tien Tung, Ya-Yun Cheng, Da-Chin Chiou, Chia-Yi Chen, Ching-Chang Wu, Y.M. Sheu, Han-Ting Tsai, C.M. Huang, G. Hsieh, G. Tsai, S. Fung, J. Wu and C.H. Diaz. *Molecular Dynamic simulation study of stress memorization in Si dislocations*. In Electron Devices Meeting (IEDM), 2012 IEEE International, pages 30.1.1–30.1.4, 2012.

[Simoen *et al.* 2009] E. Simoen, A. Brugère, A. Satta, A. Firrincieli, B. Van Daele, B. Brijs, O. Richard, J. Geypen, M. Meuris and W. Vandervorst. *Impact of the chemical concentration on the solid-phase epitaxial regrowth of phosphorus implanted preamorphized germanium*. J. Appl. Phys., vol. 105, no. 9, page 093538, 2009.

[Sklenard *et al.* 2013a] Benoit Sklenard, Jean-Charles Barbe, Perrine Batude, Pierrette Rivallin, Clement Tavernier, Sorin Cristoloveanu and Ignacio Martin-Bragado. *An atomistic investigation of the impact of in-plane uniaxial stress during solid phase epitaxial regrowth*. Appl. Phys. Lett., vol. 102, no. 15, page 151907, 2013.

[Sklenard *et al.* 2013b] Benoit Sklenard, Perrine Batude, Quentin Rafhay, Ignacio Martin-Bragado, Cuiqin Xu, Bernard Previtali, Benjamin Colombeau, Fareen-Adeni Khaja, Sorin Cristoloveanu, Pierrette Rivallin, Clement Tavernier and Thierry Poiroux. *Influence of device architecture on junction leakage in low-temperature process FDSOI MOSFETs*. Solid-State Electronics, vol. 88, no. 0, pages 9 – 14, 2013.

[Sklenard *et al.* 2014] Benoit Sklenard, Jean-Charles Barbe, Perrine Batude, Pierrette Rivallin, Clement Tavernier, Sorin Cristoloveanu and Ignacio Martin-Bragado. *Atomistic investigation of the impact of stress during solid phase epitaxial regrowth*. Phys. Status Solidi (c), vol. 11, no. 1, pages 97–100, 2014.

[Solmi *et al.* 1990] S. Solmi, E. Landi and F. Baruffaldi. *High concentration boron diffusion in silicon: Simulation of the precipitation phenomena*. J. Appl. Phys., vol. 68, no. 7, pages 3250–3258, 1990.

[Solmi *et al.* 1996] S. Solmi, A. Parisini, R. Angelucci, A. Armigliato, D. Nobili and L. Moro. *Dopant and carrier concentration in Si in equilibrium with monoclinic SiP precipitates*. Phys. Rev. B, vol. 53, pages 7836–7841, Mar 1996.

[Solmi 2001] S Solmi. *Dopants in Silicon: Activation and deactivation kinetics*. Encyclopedia of Materials: Science and Technology, edited by K. H. J. Buschow, R. W. Cahn, M. C. Flemings, B. Ilschner, et al. (Elsevier Science Ltd., 2001), pages 2331–2340, 2001.

[Spaepen & Turnbull 1979] F. Spaepen and D. Turnbull. *Kinetics of motion of crystal-melt interfaces*. AIP Conference Proceedings, vol. 50, no. 1, pages 73–83, 1979.

[Spaepen 1974] Frans Spaepen. *On the configurational entropy of amorphous Si and Ge*. Philos. Mag., vol. 30, no. 2, pages 417–422, 1974.

[Spinella *et al.* 1998] Corrado Spinella, Salvatore Lombardo and Francesco Priolo. *Crystal grain nucleation in amorphous silicon*. J. Appl. Phys., vol. 84, no. 10, pages 5383–5414, 1998.

[Stillinger & Weber 1985] Frank H. Stillinger and Thomas A. Weber. *Computer simulation of local order in condensed phases of silicon*. Phys. Rev. B, vol. 31, pages 5262–5271, Apr 1985.

[Suzuki *et al.* 2007] K. Suzuki, Y. Kataoka, S. Nagayama, C.W. Magee, T.H. Buyuklimanli and T. Nagayama. *Analytical Model for Redistribution Profile of Ion-Implanted Impurities During Solid-Phase Epitaxy*. Electron Devices, IEEE Transactions on, vol. 54, no. 2, pages 262–271, 2007.

[Tang *et al.* 1997] Meijie Tang, L. Colombo, Jing Zhu and T. Diaz de la Rubia. *Intrinsic point defects in crystalline silicon: Tight-binding molecular dynamics studiesof self-diffusion, interstitial-vacancy recombination, and formation volumes*. Phys. Rev. B, vol. 55, pages 14279–14289, Jun 1997.

[Tersoff 1988] J. Tersoff. *Empirical interatomic potential for silicon with improved elastic properties*. Phys. Rev. B, vol. 38, pages 9902–9905, Nov 1988.

[Treacy & Borisenko 2012] M. M. J. Treacy and K. B. Borisenko. *The Local Structure of Amorphous Silicon*. Science, vol. 335, no. 6071, pages 950–953, 2012.

[Van de Walle *et al.* 1993] Chris G. Van de Walle, D. B. Laks, G. F. Neumark and S. T. Pantelides. *First-principles calculations of solubilities and doping limits: Li, Na, and N in ZnSe*. Phys. Rev. B, vol. 47, pages 9425–9434, Apr 1993.

[Verlet 1967] Loup Verlet. *Computer "Experiments" on Classical Fluids. I. Thermodynamical Properties of Lennard-Jones Molecules*. Phys. Rev., vol. 159, pages 98–103, Jul 1967.

[Verlet 1968] Loup Verlet. *Computer "Experiments" on Classical Fluids. II. Equilibrium Correlation Functions*. Phys. Rev., vol. 165, pages 201–214, Jan 1968.

[Vineyard 1957] George H. Vineyard. *Frequency factors and isotope effects in solid state rate processes*. Journal of Physics and Chemistry of Solids, vol. 3, no. 1 – 2, pages 121 – 127, 1957.

[Voter *et al.* 2002] Arthur F. Voter, Francesco Montalenti and Timothy C. Germann. *Extending the TIme Scale in Atomistic Simulation of Materials*. Annu. Rev. Mater. Res., vol. 32, page 321, 2002.

[Weber *et al.* 2011] C.E. Weber, S.M. Cea, H. Deshpande, O. Golonzka and M.Y. Liu. *Modeling of NMOS performance gains from edge dislocation stress*. In Electron Devices Meeting (IEDM), 2011 IEEE International, pages 34.4.1–34.4.4, 2011.

[Williams & Elliman 1981] J.S. Williams and R.G. Elliman. *Limits to solid solubility in ion implanted silicon*. Nuclear Instruments and Methods, vol. 182-183, Part 1, pages 389 – 395, 1981.

[Williams & Elliman 1982] J. S. Williams and R. G. Elliman. *Substitutional solid solubility limits during solid phase epitaxy of ion implanted (100) silicon*. Appl. Phys. Lett., vol. 40, no. 3, pages 266–268, 1982.

[Williams & Elliman 1983] J. S. Williams and R. G. Elliman. *Role of Electronic Processes in Epitaxial Recrystallization of Amorphous Semiconductors*. Phys. Rev. Lett., vol. 51, pages 1069–1072, Sep 1983.

[Williams *et al.* 1985] J. S. Williams, R. G. Elliman, W. L. Brown and T. E. Seidel. *Dominant Influence of Beam-Induced Interface Rearrangement on Solid-Phase Epitaxial Crystallization of Amorphous Silicon*. Phys. Rev. Lett., vol. 55, pages 1482–1485, Sep 1985.

[Witvrouw & Spaepen 1993] Ann Witvrouw and Frans Spaepen. *Viscosity and elastic constants of amorphous Si and Ge*. J. Appl. Phys., vol. 74, no. 12, pages 7154–7161, 1993.

[Wooten *et al.* 1985] F. Wooten, K. Winer and D. Weaire. *Computer Generation of Structural Models of Amorphous Si and Ge*. Phys. Rev. Lett., vol. 54, pages 1392–1395, Apr 1985.

[Xu *et al.* 2012] C. Xu, P. Batude, B. Sklenard, M. Vinet, M. Mouis, B. Previtali, F. Y. Liu, J. Guerrero, K. Yckache, P. Rivallin, V. Mazzocchi, S. Cristoloveanu, O. Faynot and T. Poiroux. *FDSOI: A solution to suppress boron deactivation in low temperature processed devices*. In Junction Technology (IWJT), 2012 12th International Workshop on, pages 69–72, May 2012.

[Young & Elcock 1966] W M Young and E W Elcock. *Monte Carlo studies of vacancy migration in binary ordered alloys: I*. Proceedings of the Physical Society, vol. 89, no. 3, page 735, 1966.

[Zachariasen 1932] W. H. Zachariasen. *The atomic arrangement in glass*. J. Am. Chem. Soc., vol. 54, no. 10, pages 3841–3851, 1932.

[Zechner *et al.* 2004] Christoph Zechner, Dmitri Matveev and Axel Erlebach. *Phase-field model for the dopant redistribution during solid phase epitaxial regrowth of amorphized silicon*. Materials Science and Engineering: B, vol. 114 – 115, pages 162 – 165, 2004.

[Zhang & Northrup 1991] S. B. Zhang and John E. Northrup. *Chemical potential dependence of defect formation energies in GaAs: Application to Ga self-diffusion*. Phys. Rev. Lett., vol. 67, pages 2339–2342, Oct 1991.

[Zographos & Martin-Bragado 2008] Nikolas Zographos and Ignacio Martin-Bragado. *A Comprehensive Atomistic Kinetic Monte Carlo Model for Amorphization/Recrystallization and its Effects on Dopants*. MRS Proceedings, vol. 1070, 1 2008.

List of communications

Journals:

- **B. Sklenard**, J.–C. Barbe, P. Batude, P. Rivallin, C. Tavernier, S. Cristoloveanu, and I. Martin–Bragado, "Atomistic investigation of the impact of stress during solid phase epitaxial regrowth," Phys. Status Solidi C, 11 (2014) pp. 97–100.

- **B. Sklenard**, J.–C. Barbe, P. Batude, P. Rivallin, C. Tavernier, S. Cristoloveanu, and I. Martin–Bragado, "An atomistic investigation of the impact of in-plane uniaxial stress during solid phase epitaxial regrowth," Appl. Phys. Lett., 102 (2013), p. 151907.

- **B. Sklenard**, P. Batude, Q. Rafhay, I. Martin-Bragado, C. Xu, B. Previtali, B. Colombeau, F.–A. Khaja, S. Cristoloveanu, P. Rivallin, C. Tavernier, and T. Poiroux, "Influence of device architecture on junction leakage in low-temperature process FDSOI MOSFETs," Solid-State Electron., 88 (2013), pp. 9–14.

- I. Martin–Bragado and **B. Sklenard**, "Understanding Si(111) solid phase epitaxial regrowth using monte carlo modeling: Bi–modal growth, defect formation, and interface topology," J. Appl. Phys., 112 (2012), p. 024327.

Conferences:

- B. Voisin, B. Roche, E. Dupont–Ferrier, **B. Sklenard**, M. Cobian, X. Jehl, O. Cueto, R. Wacquez, M. Vinet, Y.–M. Niquet, S. D. Franceschi, and M. Sanquer, "The Coupled Atom Transistor: a first realization with shallow donors implanted in a FDSOI silicon nanowire," in 43rd European Solid-State Device Conference (2013).

- B. Voisin, B. Roche, E. Dupont–Ferrier, **B. Sklenard**, M. Cobian, X. Jehl, O. Cueto, R. Wacquez, M. Vinet, Y.–M. Niquet, S. D. Franceschi, and M. Sanquer, "The coupled atom transistor: a first realization with shallow donors implanted in a trigate silicon nanowire," in Silicon Nanoelectronics Workshop (2013).

- **B. Sklenard**, I. Martin–Bragado, J.–C. Barbe, P. Batude, P. Rivallin, C. Tavernier, and S. Cristoloveanu, "Atomistic investigation of the impact of stress during solid phase epitaxial regrowth," in European Materials Research Society Spring meeting, Strasbourg (2013).

- P. Batude, **B. Sklenard**, C. Xu, B. Previtali, B. D. Salvo, and M. Vinet, "Low temperature FDSOI devices, a key enabling technology for 3D sequential integration," in International Symposium on VLSI Technology, Systems, and Applications (2013), *Invited paper*, pp. 1–4.

- C. Xu, P. Batude, **B. Sklenard**, M. Vinet, M. Mouis, B. Previtali, F. Y. Liu, J. Guerrero, K. Yckache, P. Rivallin, V. Mazzocchi, S. Cristoloveanu, O. Faynot, and T. Poiroux, "FDSOI: A solution to suppress boron deactivation in low temperature processed devices," in 12th International Workshop on Junction Technology, pp. 69–72.

- C. Xu, P. Batude, M. Vinet, M. Mouis, M. Casse, **B. Sklenard**, B. Colombeau, Q. Rafhay, C. Tabone, J. Berthoz, B. Previtali, J. Mazurier, L. Brunet, L. Brevard, F. A. Khaja, J. Hartmann, F. Allain, A. Toffoli, R. Kies, C. Le Royer, S. Morvan, A. Pouydebasque, X. Garros, A. Pakfar, C. Tavernier, O. Faynot, and T. Poiroux, "Improvements in low temperature ($\leqslant$ 625 °C) FDSOI devices down to 30 nm gate length," in International Symposium on VLSI Technology, Systems, and Applications (2012), pp. 1–2.

- **B. Sklenard**, C. Xu, P. Batude, B. Previtali, C. Tabone, Q. Rafhay, B. Colombeau, F.–A. Khaja, I. Martin–Bragado, J. Berthoz, F. Allain, A. Toffoli, R. Kies, M. A. Jaud, P. Rivallin, S. Cristoloveanu, C. Tavernier, O. Faynot, and T. Poiroux, "FDSOI devices: A solution to achieve low junction leakage with low temperature processes ($\leqslant$ 650 °C)," in International Conference on Ultimate Integration on Silicon (2012), pp. 169—172.

- P. Batude, M. Vinet, B. Previtali, C. Tabone, C. Xu, J. Mazurier, O. Weber, F. Andrieu, L. Tosti, L. Brevard, **B. Sklenard**, P. Coudrain, S. Bobba, H. Ben Jamaa, P. Gaillardon, A. Pouydebasque, O. Thomas, C. Le Royer, J. Hartmann, L. Sanchez, L. Baud, V. Carron, L. Clavelier, G. De Micheli, S. Deleonibus, O. Faynot, and T. Poiroux, "Advances, challenges and opportunities in 3D CMOS sequential integration," in IEEE International Electron Devices Meeting (2011), *Invited paper*, pp. 7.3.1– 7.3.4.

Patents:

- **B. Sklenard** and P. Batude, "Circuit intégré 3D," French patent 2986370, August 2, 2013

- **B. Sklenard** and P. Batude, "3D integrated circuit," US patent App. 13/751,489, filed January 28, 2013

- P. Batude, **B. Sklenard** and F. Mazen, "Recristallisation de blocs de source et de drain par le haut," French patent App. 1357929, filed August 9, 2013

- P. Batude, **B. Sklenard**, J.–M. Hartmann and M. Vinet, "Procédé amélioré de réalisation de zones dopées sous les espaceurs d'un transistor," French patent App. 1357931, filed August 9, 2013

Physical modeling of junction processing in FDSOI devices for 20 nm node and below

Abstract

Complementary metal oxide semiconductor (CMOS) device scaling involves many technological challenges in terms of junction formation. Solid phase epitaxial regrowth (SPER) at temperatures below 600 °C is an attractive technique since it enables to form highly–activated and abrupt junctions that are required for advanced technology nodes such as 20 nm and beyond. In this manuscript, we present a comprehensive atomistic model relying on the lattice Kinetic Monte Carlo (LKMC) method to simulate SPER kinetics in silicon. The model is based on the phenomenological description of the microscopic recrystallization mechanisms proposed by Drosd and Washburn in [J. Appl. Phys. **53**, 397 (1982)] by distinguishing among {100}, {110} and {111} events depending on the local regrowth plane and has been implemented in the MMonCa simulator [Appl. Phys. Lett. **98**, 233109 (2011)]. This is the same basis than the atomistic model of Martín–Bragado and Moroz proposed in [Appl. Phys. Lett. **95**, 123123 (2009)] and available in the Synopsys SProcess KMC commercial tool. Nevertheless, in our work the formation of twin configurations during {111} events has been incorporated giving rise to significant changes in the implementation. The model has been calibrated on single–directional SPER experiments and allows predicting the regrowth anisotropy and temperature dependence. In particular, it has been used to explain the formation of defective regions in FDSOI devices annealed with a low processing temperature. In this work, the LKMC model has also been extended in order to include the influence of non–hystrostatic stress and dopant–enhanced regrowth that are technologically relevant. Non–hydrostatic stress effects have been incorporated using the concept of activation strain tensor introduced by Aziz, Sabin and Lu in [Phys. Rev. B **44**, 9812 (1991)] and only four independent parameters are required. The presence of ionized dopants has been shown to cause an enhancement of the regrowth velocity which has been attributed to a Fermi level effect. A three–dimensional Thomas–Fermi–Poisson solver has been implemented and coupled with the LKMC model allowing to take into account the band bending at amorphous/crystalline interface. The phenomenological generalized Fermi level shifting (GFLS) correction proposed by Williams and Elliman in [Phys. Rev. Lett. **51**, 1069 (1983)] has been used to modify the microscopic recrystallization rates. Simulations of the regrowth velocity as a function of temperature for different dopant concentrations have shown a reasonable agreement with experimental data. In summary, in this manuscript a unified SPER model relying on the LKMC approach is presented. It takes into account various technologically relevant parameters influencing the regrowth kinetics such as temperature, crystalline orientation, stress and dopants. The model is *per se* three-dimensional and can therefore be used to explore multi–directional regrowth phenomena that take place in real electronic devices.

Keywords: Solid Phase Epitaxial Regrowth, Fully Depleted SOI, Kinetic Monte Carlo